Optical Forces on Metastable Helium

A Dissertation Presented

by

Christopher Scott Corder

to

The Graduate School

in Partial Fulfillment of the Requirements

for the Degree of

Doctor of Philosophy

in

Physics

Stony Brook University

December 2014

Stony Brook University

The Graduate School

Christopher Scott Corder

We, the dissertation committee for the above candidate for the
Doctor of Philosophy degree, hereby recommend
acceptance of this dissertation.

Harold Metcalf – Dissertation Advisor
Distinguished Teaching Professor, Department of Physics and Astronomy

Dominik Schneble – Chairperson of Defense
Associate Professor, Department of Physics and Astronomy

Jacobus Verbaarschot
Graduate Program Director and Professor, Department of Physics and Astronomy

Petr Anisimov
Physicist, Visiting Scientist, RIKEN
& Postdoctoral Researcher, Los Alamos National Lab

This dissertation is accepted by the Graduate School.

Charles Taber
Dean of the Graduate School

Abstract of the Dissertation

Optical Forces on Metastable Helium

by

Christopher Scott Corder

Doctor of Philosophy

in

Physics

Stony Brook University

2014

Optical forces using lasers allow precise control over the motion of atoms. The bichromatic optical force (BF) is unique in its large magnitude and velocity range, arising from the absorption and stimulated emission processes. These properties were used to transversely collimate a beam of metastable helium (He^*) using the $2^3S - 2^3P$ transition. The collimation created a very bright beam of He^*, allowing experiments of neutral atom lithography. The He^* beam was used to pattern material surfaces using a resist-based lithography technique, where the pattern was determined by either mechanical or optical masks. The optical masks produced features with a separation of half the wavelength of the light used. Patterning was successfully demonstrated with both IR and UV optical masks. The etched pattern resolution was ~ 100 nm and limited by the material surface.

Further experiments were performed studying the ability of the bichromatic force to cool. The finite velocity range of the BF allows estimation of a characteristic cooling time which is independent of the excited state lifetime, only depending on the atomic mass and optical transition energy. Past experiments, including

the helium collimation used for neutral atom lithography, have demonstrated that the BF can collimate and longitudinally slow atomic beams, but required long interaction times that included many spontaneous emission (SE) events. The effect of SE can be mitigated, and is predicted to not be necessary for BF cooling. Since the BF cooling time is not related to the excited state lifetime, a transition can be chosen such that the cooling time is shorter than the SE cycle time, allowing direct laser cooling on atoms and molecules that do not have cycling transitions. Experiments using the helium $2^3\mathrm{S} - 3^3\mathrm{P}$ transition were chosen because the BF cooling time (285 ns) is on the order of the average SE cycle time (260 ns). Numerical simulations of the experimental system were run predicting compression of the atomic velocity distribution. Our experimental results demonstrate the stimulated nature of the force through many atomic recoils from the light in less than one SE cycle time. A large range of the atomic velocity distribution is accelerated and accumulates at the velocity limit of the force. This accumulation results in an increase in the velocity space density, demonstrating cooling.

For my brilliant wife
Stephanie

Contents

List of Figures

List of Tables

Acknowledgements

This work owes much to the people in my life. In particular, my parents who have consistently supported me in all my endeavors. Their examples have been the inspiration for my work ethic, which was necessary for this accomplishment. My success is also strongly indebted to my wife Stephanie. Her intelligence and assistance has made me a smarter better scientist.

I want to thank my advisor Hal who allowed me to join his research group and choose these projects. I've learned a great many things and am happy to have such a terrific role model for my future career. I want to thank Jason Reeves and Claire Allred for being excellent mentors to me when I first arrived in the lab. My lab skills are greatly owed to them. I also want to thank all the members of the Metcalf group over my many years here, I've enjoyed our daily lunches and discussions. Particular thanks to Brian Arnold who worked with me during the UV bichromatic force experiments. Thanks to my committee and Martin Cohen for helping edit this dissertation. And thanks to the Stony Brook physics department and the AMO groups here in the basement.

Chapter 1

Introduction

Optical forces in the field of atomic physics have become well-established techniques in the decades since the discovery of laser cooling [1]. The use of lasers to manipulate the motion and cool atomic samples has become a standard technique in most atomic physics laboratories. This control has been exploited by many experiments to utilize atoms for precision measurements, such as gravimeters in the form of atom interferometers [2]. Optical cooling techniques allow the trapping of atoms, which when done in high finesse optical cavities are able to probe quantum electrodynamical effects of the interaction between the atom and light. These implementations are leading research in the field of quantum information [3]. Particularly exciting has been the creation of ultracold samples of dilute gas reaching Bose-Einstein condensation and other more exotic phases of matter [4–6]. These experiments allow a unique experimentally-based method for exploring theoretical condensed matter systems [7, 8].

Besides the experiments born out of these control and cooling techniques, there have been exciting experiments in the mechanical effects of the atom-light interaction. Recent years have seen the technique of laser cooling extended to mechanical objects of macroscopic size, able to be cooled to their quantum ground state [9]. Another recent push has been established in the direct laser cooling of molecular gases analogous to the atoms described above [10]. These cold molecules would allow exciting probes of fundamental physics from condensed matter [8] to extensions of the standard model [11]. Recent work has also explored the cooling of more exotic atomic elements that were previously ignored because of their seeming complexity, but now are wanted to exploit this very complexity. Each of these areas of cooling has required developing new and different techniques and ideas on methods for manipulating the optical interaction to give the desired result. This has led to the discovery of

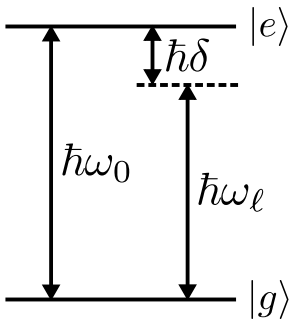

Figure 1.1: The energy structure of a two level system showing the separation between the ground, $|g\rangle$, and excited, $|e\rangle$, states. The laser energy $\hbar\omega_\ell$ may be detuned from resonance, where the sign of the detuning is defined as $\delta = \omega_\ell - \omega_0$.

methods including sideband, Sisyphus, dark state, and molecule Doppler cooling [10, 12–15].

The field of optical forces arising from multifrequency fields is relatively unexplored. The impact of additional optical fields provides new opportunities for molding the interaction to give a desired result, which of course comes at the expense of increasing complexity. This thesis begins to explore this field by looking at the opportunities that arise from the simplest case, adding a second optical field.

1.1 Atom-Optical Interactions

The interaction of isolated atoms with optical fields can lead to many effects, but the discussion here will be restricted to a particular set: optical dipole interactions. The dipole interaction is the first term in the series of a multipole expansion of an atom in an applied electric field. It is often the strongest optical effect on an atom. The electric field is assumed to have no structure on the length scale of the atom, and the atom responds as a pure dipole in a uniform field.

1.1.1 The Dipole Interaction

The two-level atom will serve as the basic system for the work in this thesis. The electron energy level structure is shown in Fig. 1.1, and the bare atomic Hamiltonian can be written as

$$\mathcal{H}_0 = \hbar\omega_g|g\rangle\langle g| + \hbar\omega_e|e\rangle\langle e| \tag{1.1}$$

An induced dipole moment $\vec{d}$ allows coupling between the two levels through an interaction with an applied electric field $\vec{E}(t)$. The interaction Hamiltonian is then

$$\mathcal{H}_I = \vec{d} \cdot \vec{E}(t) = \hbar\Omega(t)|g\rangle\langle e| + \hbar\Omega^*(t)|e\rangle\langle g| \tag{1.2}$$

written in terms of the Rabi frequency defined as $\Omega(t) = -\frac{\vec{d}\cdot\vec{E}(t)}{\hbar}$. The definite parity of the electronic spatial wavefunctions $\psi_i(r)$ and the odd parity of the dipole operator $\vec{r}$ guarantee no single state dipole moment as $\int \psi_i^*(r) r \psi_i(r) dr = 0$. However, two distinct electronic states can have a non-zero dipole moment $\vec{d} = -e\langle e|\vec{r}|g\rangle$, where the $-e$ outside the bra/ket is the charge of the electron. The value of $\vec{d}$ for a particular atom can be evaluated by integrating over its spatial wavefunctions for $|g\rangle$ and $|e\rangle$.

We can begin by simply noting the dynamics of the original Hamiltonian $\mathcal{H}_0$ by setting $\Omega(t) = 0$. Then the Schrödinger equation for an arbitrary state $|\psi\rangle = c_g(t)|g\rangle + c_e(t)|e\rangle$ is

$$i\hbar\frac{\mathrm{d}}{\mathrm{dt}}|\psi\rangle = \mathcal{H}_0|\psi\rangle \tag{1.3}$$

and simplifies to a set of differential equations.

$$\dot{c}_g(t) = -i\omega_g c_g(t) \tag{1.4a}$$

$$\dot{c}_e(t) = -i\omega_e c_e(t) \tag{1.4b}$$

The solutions are static state populations that accumulate phase proportional to their energy. This leads to a prudent choice for a complete set of basis states for the full Hamiltonian $\mathcal{H} = \mathcal{H}_0 + \mathcal{H}_I$.

$$|\psi\rangle = c_g(t)e^{-i\omega_g t}|g\rangle + c_e(t)e^{-i\omega_e t}|e\rangle \tag{1.5}$$

Plugging $|\psi\rangle$ into the combined Hamiltonian and some algebra leaves a set of differential equations:

$$\dot{c}_g(t) = -i\Omega(t)e^{-i\omega_0 t}c_e(t) \tag{1.6a}$$

$$\dot{c}_e(t) = -i\Omega^*(t)e^{i\omega_0 t}c_g(t) \tag{1.6b}$$

where $\omega_0 = \omega_e - \omega_g$. It is important to remember that $\Omega(t)$ will contain any time dependence of the applied electric field.

A laser field can be written in terms of its optical frequency ω_ℓ as $\vec{E}(t) = \mathcal{E}\,\hat{\epsilon}\cos(\omega_\ell t)$ where $\hat{\epsilon}$ is the polarization vector and $\mathcal{E}$ is a function that can depend on space and timescales much slower than ω_ℓ^{-1}. Plugging this expression into $\Omega(t)$ separates the optical frequency

oscillation from the slower Rabi frequency time dependence

$$\Omega(t) = -\left(\frac{d\mathcal{E}}{\hbar}|\vec{d}| \cdot \hat{\epsilon}\right)\cos(\omega_\ell t) = \Omega_0 \cos(\omega_\ell t) \tag{1.7}$$

This leads to a set of differential equations which, in general, cannot be solved analytically.

$$\dot{c}_g(t) = -i\frac{\Omega_0}{2}(e^{-i\omega_\ell t} + e^{i\omega_\ell t})e^{-i\omega_0 t}c_e(t) \tag{1.8a}$$

$$\dot{c}_e(t) = -i\frac{\Omega_0^*}{2}(e^{-i\omega_\ell t} + e^{i\omega_\ell t})e^{i\omega_0 t}c_g(t) \tag{1.8b}$$

By examining these equations we can see that changes in state populations vary on two distinct time scales; fast $e^{\pm i(\omega_\ell+\omega_0)t}$ and slow $e^{\pm i(\omega_\ell-\omega_0)t}$. The rotating wave approximation [16] drops the fast anti-resonant timescale oscillations, $\sim 10^{15}$ Hz for optical transitions. The anti-resonant term is considered to oscillate too quickly compared with relevant experimental timescales and is assumed to average to zero. Only the more slowly varying resonant timescale of $\omega_0 - \omega_\ell$ is considered, which for typical experiments is $1 - 100$ MHz.

1.1.2 Rabi Oscillations

After applying the rotating wave approximation Eq.'s 1.8 reduce to a deceptively simple looking set of differential equations where the frequency detuning is defined as $\delta = \omega_\ell - \omega_0$. It is important to remember that Ω_0 can still contain a non-trivial dependence on time and space.

$$\dot{c}_g(t) = -\frac{i}{2}\Omega_0\, c_e(t)e^{i\delta t} \tag{1.9a}$$

$$\dot{c}_e(t) = -\frac{i}{2}\Omega_0\, c_g(t)e^{-i\delta t} \tag{1.9b}$$

It will be instructive to first solve the state amplitudes $c_{g,e}(t)$ for the simple case of a constant laser field. This is most easily done by taking Eq. 1.9 to second order to decouple the set of differential equations.

$$\ddot{c}_g(t) - i\delta\dot{c}_g(t) + \frac{|\Omega_0|^2}{4}c_g(t) = 0 \tag{1.10a}$$

$$\ddot{c}_e(t) + i\delta\dot{c}_e(t) + \frac{|\Omega_0|^2}{4}c_e(t) = 0 \tag{1.10b}$$

The resulting solutions, when squared to get the observable state populations, show that an atom initially populating the ground state driven by on-resonance laser light oscillates between the two states at the Rabi frequency. This is the process of absorption and stim-

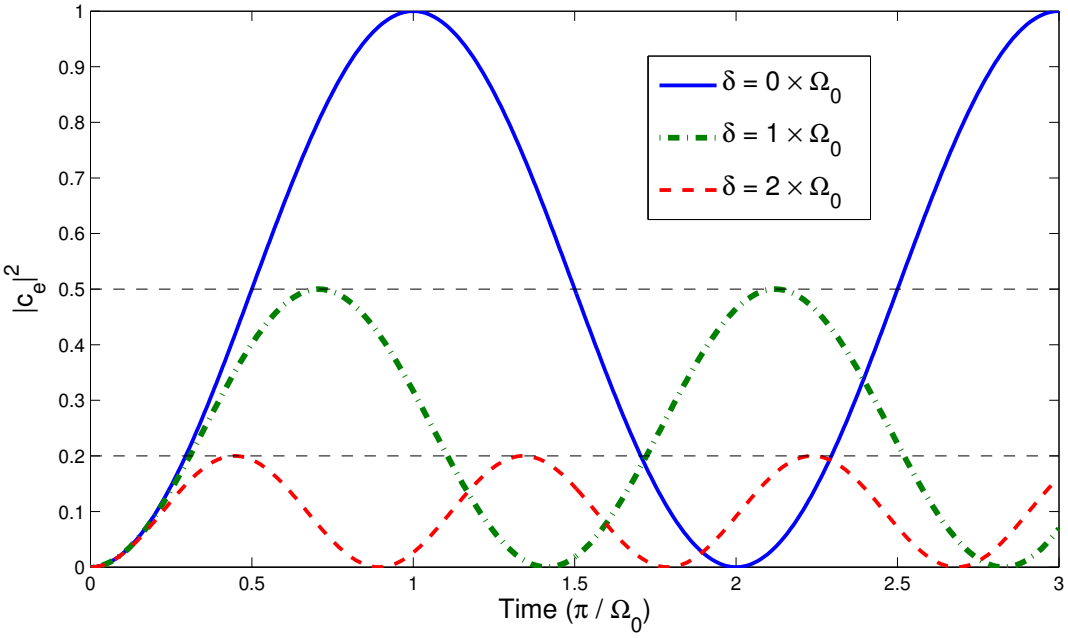

Figure 1.2: The excited state population is plotted vs time for a CW driving field at three values of laser detuning. For zero detuning, complete population transfer occurs at a time of $\Omega_0 t = \pi$. The non-zero detunings reduce the amplitude of transferred population and increase the rate of oscillation.

ulated emission. If the laser frequency is detuned from resonance the population in the excited state never reaches 100% and the oscillations occur at the generalized Rabi frequency $\Omega_0' = \sqrt{|\Omega_0|^2 + \delta^2}$. The solutions are plotted for several values of δ in Fig. 1.2.

$$|c_g(t)|^2 = 1 - \left(\frac{\Omega_0}{\Omega_0'}\right)^2 \sin^2 \frac{\Omega_0' t}{2} \tag{1.11a}$$

$$|c_e(t)|^2 = \left(\frac{\Omega_0}{\Omega_0'}\right)^2 \sin^2 \frac{\Omega_0' t}{2} \tag{1.11b}$$

1.1.3 The Light Shift

We can see from their oscillatory behavior that the atomic bare states in Fig. 1.2 are no longer the eigenstates of the system. To find the eigenstates of the combined Hamiltonian

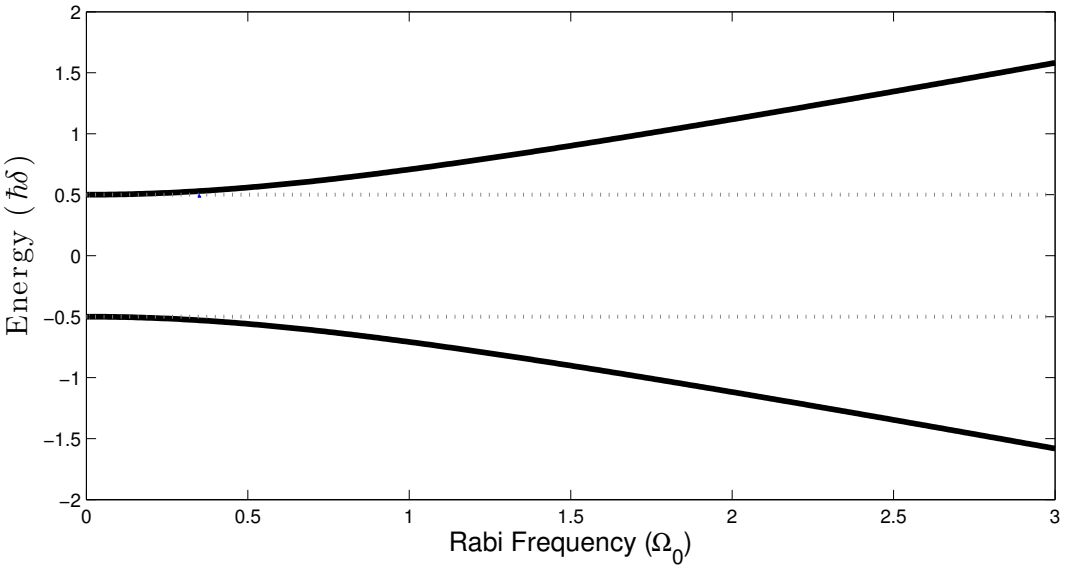

Figure 1.3: The eigenstates are initially separated by $\hbar\delta$, and repel one another with increasing laser intensity ($I \propto \Omega_0^2$). This separation grows as the generalized Rabi frequency Ω_0'.

(Eq's 1.1+1.2) we perform a coordinate transformation to a frame rotating at a rate δ.

$$c_g'(t) = c_g(t)e^{-i\delta t/2} \tag{1.12a}$$

$$c_e'(t) = c_e(t)e^{i\delta t/2} \tag{1.12b}$$

Following this transformation, the linear set of differential equations (Eq's 1.9) can be written in matrix form as

$$\begin{pmatrix} \dot{c}_g'(t) \\ \dot{c}_e'(t) \end{pmatrix} = -\frac{i}{2}\begin{pmatrix} \delta & \Omega_0 \\ \Omega_0^* & -\delta \end{pmatrix}\begin{pmatrix} c_g'(t) \\ c_e'(t) \end{pmatrix} \tag{1.13}$$

Diagonalizing the matrix gives the eigenenergies and eigenfunctions as

$$E_\pm = \pm\frac{\hbar}{2}\sqrt{|\Omega_0|^2 + \delta^2} = \pm\frac{\hbar\Omega_0'}{2} \tag{1.14a}$$

$$|-\rangle = \sqrt{1/2(1+\delta/\Omega_0')}|\tilde{g}\rangle + \sqrt{1-1/2(1+\delta/\Omega_0')}|\tilde{e}\rangle \tag{1.14b}$$

$$|+\rangle = \sqrt{1/2(1-\delta/\Omega_0')}|\tilde{g}\rangle + \sqrt{1-1/2(1-\delta/\Omega_0')}|\tilde{e}\rangle \tag{1.14c}$$

The tildes are included to remind us that these are the atomic states including the time dependence of the rotating frame, but those phases have no effect on the population evolution. The eigenenergies of the system are given by the generalized Rabi frequency as shown in Fig. 1.3. At zero intensity ($\Omega_0 = 0$) the two states are separated by the detuning of the laser and are exactly the bare atomic ground and excited states. As the intensity increases, the two eigenstates separate and become a mixture of the original ground and excited states.

1.1.4 The Dressed Atom

The previous sections considered solutions to $\mathcal{H} = \mathcal{H}_0 + \mathcal{H}_I$, where atomic states obtained from $\mathcal{H}_0$ are influenced through an interaction with an external electric field. The energy of these states is shifted due to varying amounts of interaction energy through $\mathcal{H}_I$. It can be useful to study the system of dressed states that are formed by including the electric field Hamiltonian ($\mathcal{H}_f$) in the system so that $\mathcal{H} = \mathcal{H}_0 + \mathcal{H}_I + \mathcal{H}_f$. The energy structure of the atomic system ($\mathcal{H}_0$) has two levels separated by $\hbar\omega_0$. This can be combined with the energy contained in the optical field $E_n = (n + \frac{1}{2})\hbar\omega_\ell$, where n is the integer number of photons. Since only classical light fields will be considered, the $\frac{1}{2}\hbar\omega_\ell$ zero point energy will be omitted from this point onward. The combined state will be denoted by $|i, N\rangle$ with $i = g$ or e. The spectrum formed by these dressed states is shown in Fig. 1.4. The states $|g, N\rangle$ and $|e, N\rangle$ are still separated by the atomic energy, however the combined effect of losing one quantum of photon energy and gaining one quantum of atomic energy puts the $|e, N-1\rangle$ state very near $|g, N\rangle$, as seen in Fig. 1.4. These two states are referred to as being in a single manifold, and correspond to the atom removing one photon from the laser field (absorption) and in the process transferring from its ground to excited state. The system is now parameterized into two energy scales. The first comprises states within a manifold differing by a single photon and separated in energy by $\hbar\delta$. The second is between different manifolds separated by the much larger $\hbar\omega_\ell$. The interaction Hamiltonian $\mathcal{H}_I$ for this system has no coupling terms between the different manifolds. Spontaneous emission (SE) is usually the only coupling between these levels and can lead to effects such as the Mollow triplet [17], but will be ignored here to study coherent effects.

Since each manifold has an identical structure the dressed state Hamiltonian can be reduced to

$$\mathcal{H} = \hbar \begin{pmatrix} 0 & \Omega_0/2 \\ \Omega_0^*/2 & \delta \end{pmatrix} \tag{1.15}$$

and diagonalized to find the new eigenstates of the combined system. These eigenstates (nec-

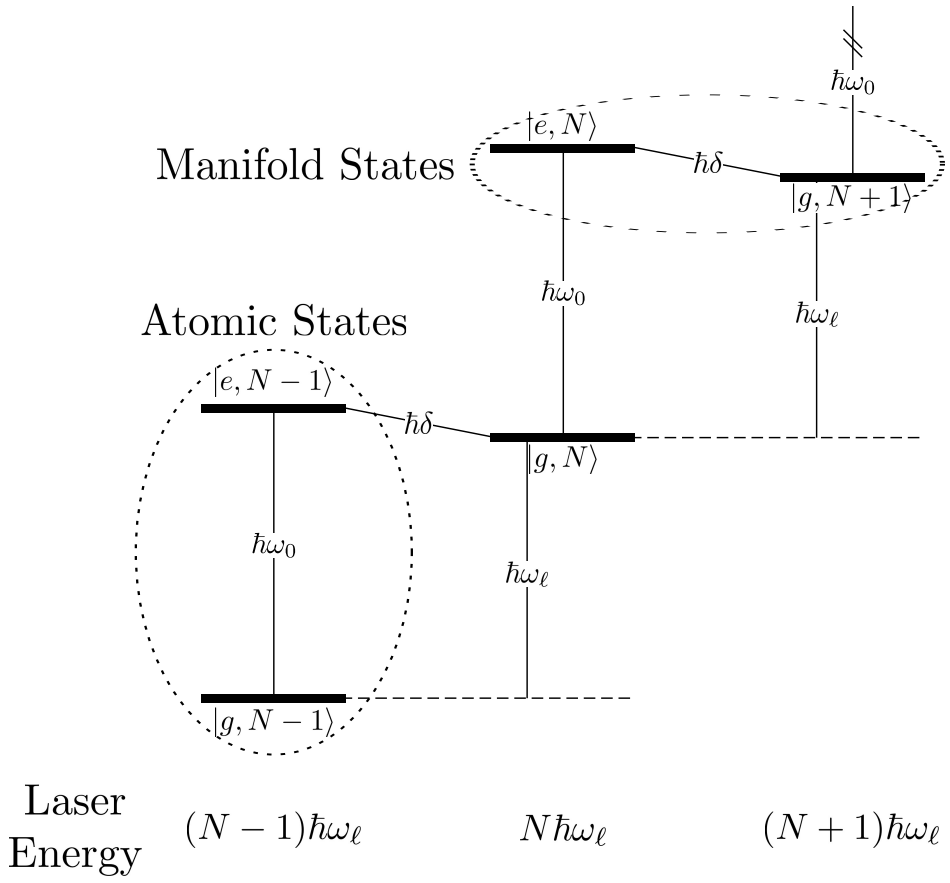

Figure 1.4: Level spectrum of the dressed states formed by including the laser energy with the atomic states. The separation between ground and excited states associated with a single photon change in the laser field is very much smaller than the original atomic state separation $\delta \ll \omega_0$ (not drawn to scale). The dressed state picture can be reduced to a single manifold to study coherent effects since neighboring manifolds are not coupled by the laser.

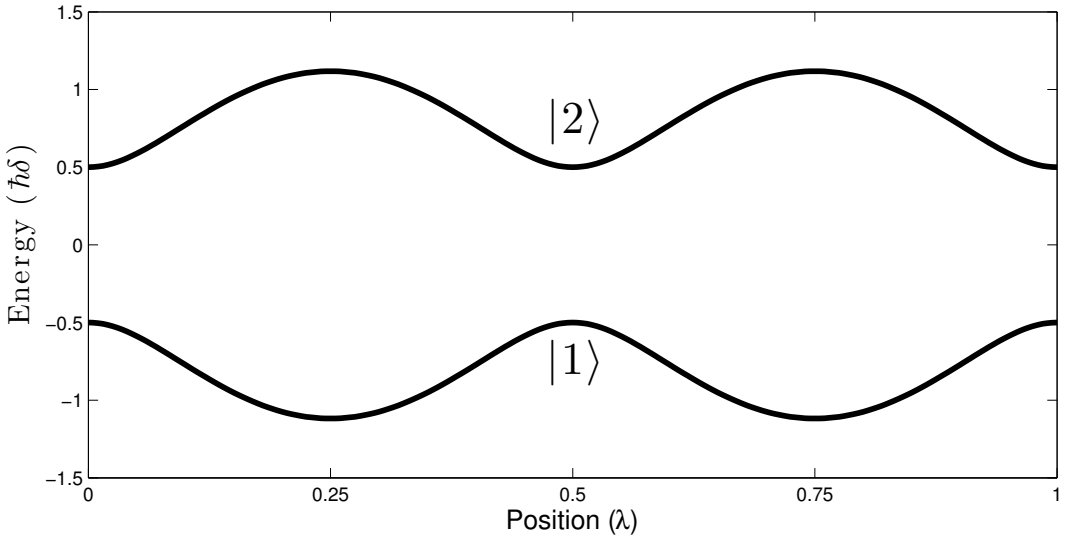

Figure 1.5: The eigenenergies of the dressed states $|1\rangle$ and $|2\rangle$ for a standing wave light field with $\Omega_0 = 2\delta$.

essarily time independent) consist of superpositions of the uncoupled states. The eigenenergies of the system are

$$E_n = \hbar/2 \left(\delta \pm \sqrt{\delta^2 + \Omega_0^2} \right) + \hbar n \omega_\ell \tag{1.16}$$

where n determines the manifold and the first term shows the structure within a manifold. The energy gap between coupled states grows as the Rabi frequency is increased. This is the same effect described as the light shift in Sec. 1.1.3. The eigenstate solutions [18], written in terms of a mixing angle $\tan 2\theta = -\Omega_0/\delta$ for $0 \leq \theta < \pi$,

$$|1\rangle = \sin\theta |g, n\rangle + \cos\theta |e, n-1\rangle \tag{1.17a}$$

$$|2\rangle = \cos\theta |g, n\rangle - \sin\theta |e, n-1\rangle \tag{1.17b}$$

show that with increasing Rabi frequency there is increased mixing of the bare atomic ground and excited state. This maps back to the Rabi oscillations of Sec. 1.1.2. If the eigenenergies are plotted as a function of position for a standing wave optical field, shown in Fig. 1.5, the energy oscillates on the half wavelength scale. This will be important for the dipole force discussed later in Sec. 2.2.

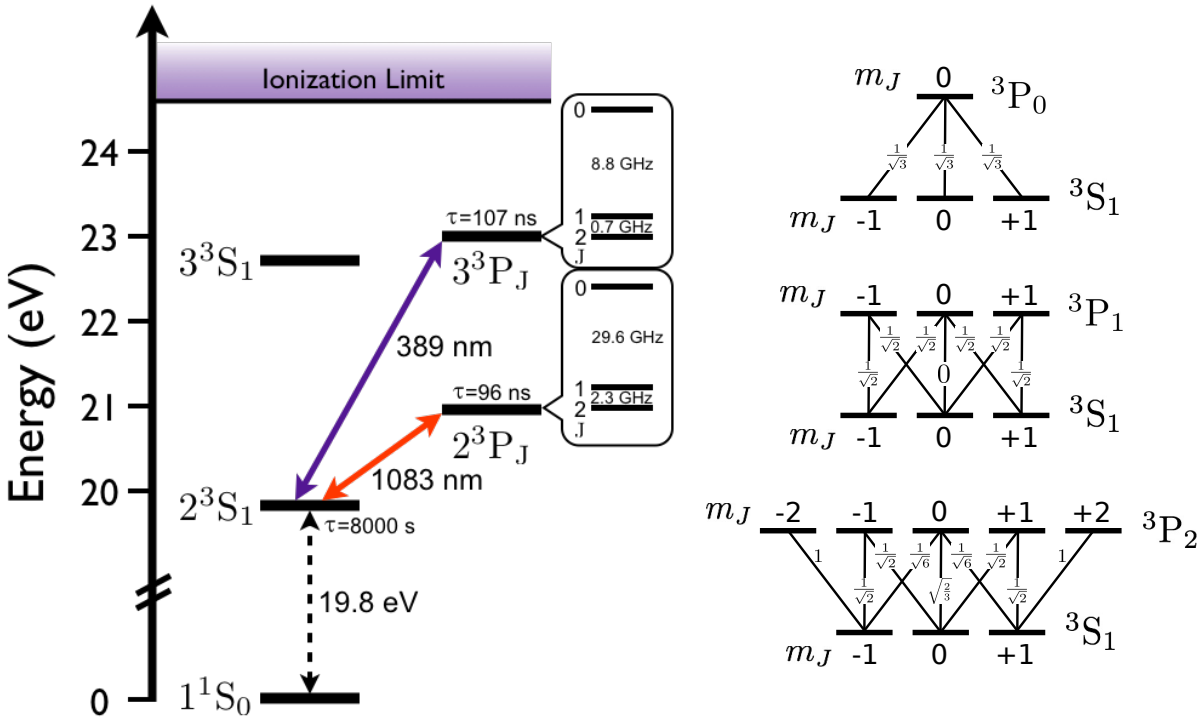

Figure 1.6: The relevant energy levels for He* are shown on the left. The degenerate magnetic structure of each $S_1 \rightarrow P_J$ transition is shown on the right with the relative coupling strength ($\propto \Omega$) between m_J levels determined by the Clebsch-Gordon coefficients.

1.2 He* as a Two Level Atom

The atomic system used for all the experiments of this thesis is the metastable $n = 2$, $l = 0$ triplet state of Helium, denoted as He*. The beauty of the Helium atom is its simplicity. With an atomic mass of four it contains no nuclear spin. There are only two electrons, which at the lowest energy fill the 1^1S_0 state. The next closest energy level, 2S, is ~ 20 eV away, an energy far too large to be of any use for optical experiments. Luckily, the two electron system provides parallel sets of electronic states arising from the singlet/triplet systems formed from the relative alignment of the two electron spins, where the spin wavefunction is symmetric/antisymmetric on electron exchange [19]. The triplet set of states closely mimic the singlet system except beginning at $n = 2$, since having two electrons in the same $n = 1$ level with a triplet wavefunction would violate the Pauli principle. The triplet system is uncoupled from the singlet system because the required spin flip forbids electric dipole transitions. This means that for the triplet states of Helium, the 2^3S_1 state is the lowest

Transition	Energy (eV)	$\omega_0/2\pi$ (THz)	λ (nm)	$\gamma/2\pi$ (MHz)	τ (ns)	$\omega_r/2\pi$ (kHz)	I_s (mW/mm^2)	v_r (m/s)	γ/k (m/s)
$2^3S \rightarrow 2^3P$	1.14	276.7	1083.3	1.63	97.9	42.5	1.7×10^{-3}	0.092	1.76
$2^3S \rightarrow 3^3P$	3.19	770.7	389.0	1.51	105.5	329.4	3.3×10^{-2}	0.256	0.58

Table 1.1: The relevant parameters for the optical transitions in He* taken or calculated from values listed on the NIST Atomic Spectra Database [21].

energy state. In fact, it is the longest lived metastable state contained in the noble gas atoms (τ = 2.2 hours) [20], being doubly forbidden to optical decay by spin and orbital angular momentum quantum numbers.

If we now consider the system beginning with the metastable "ground" state (Fig. 1.6), the nearest triplet energy levels are the set of $2^3P_{J=2,1,0}$. These states are coupled to the 2^3S_1 state through an electric dipole moment allowing an optical transition at the wavelength 1083 nm, an experimentally-convenient value given its proximity to commonly used telecommunication wavelengths. The next nearest optical transition is to the $3^3P_{J=2,1,0}$ state. The change in principal quantum number for the $2^3S \rightarrow 3^3P$ transition means it is larger in energy than the previous one, and puts the wavelength in the UV near 389 nm. While these transitions differ considerably in energy and coupling strength, they share a very common structure. Each excited P state is split into three through the fine structure splitting. They are labeled with the total angular momentum quantum number $\vec{J} = \vec{L} + \vec{S}$ with values 2, 1, or 0. The fine structure splitting is large enough that when coupled by a laser each excited state can be considered isolated. Since there is no nuclear spin, m_J sublevels in the absence of any magnetic field are energy degenerate for a given J. However, they are important to take into account as the polarization of the optical field will determine whether the transition is between states of $\Delta m_J = 0$ or ± 1. This can lead to dark state formation [1] for transitions to the levels with $J \neq 2$.

Typically the J = 2 excited state will be used. It provides a clear cycling transition if optically pumped to the $m_J = \pm 1$ ground state and excited using the proper ($\sigma^{\pm}$) polarization. A second useful feature for an unpolarized atomic sample is that with π polarized light there are no dark states and all three transitions have roughly the same strength (see Fig. 1.6). Some important parameters for the two transitions are given in Table 1.1.

Chapter 2

Optical Forces on Atoms

The interaction between atoms and optical beams induces dynamics between the different electronic states through absorption and emission of the field quanta. The transfer from an atomic state of lower energy to one of higher energy is possible through the absorption of the energy difference from the applied field. In addition to its energy, the electromagnetic radiation of the field also carries momentum. An absorbing/emitting atom must undergo a momentum change so that the total momentum of the atom and field is conserved. This momentum transfer in the absorption and emission processes gives rise to optical forces.

2.1 The Radiative Optical Force

When a single traveling-wave laser beam is applied to a two level atom, the atom can absorb energy from the field and transfer to the excited electronic state. This absorption extracts energy ($E = \hbar\omega_\ell$) from the field, and therefore also a momentum given by $\vec{p} = \hbar\vec{k}$ where $k = \frac{\omega_\ell}{c} = \frac{2\pi}{\lambda}$. This momentum transfer, shown in Fig 2.1(a), causes an atom initially at rest to move at the recoil velocity ($\mathrm{v}_r = \frac{\hbar k}{M}$), where M is the mass of the atom. Assuming the associated kinetic energy, written in terms of the recoil frequency ($\Delta\mathrm{KE} = \hbar\omega_r = \frac{(\hbar k)^2}{2M}$), is small compared to the linewidth of the excited atomic state (γ), the applied field will continue to interact resonantly with the atom. The state will transfer to the ground state and emit the energy and momentum back into the field through stimulated emission shown in Fig 2.1(b). Because the field now increases in momentum, the atom returns to rest. From these two processes alone we cannot obtain a useful force on the atom since on average there is no net momentum transfer.

Fortunately, spontaneous emission (SE) gives us a way to break this cycle and create the

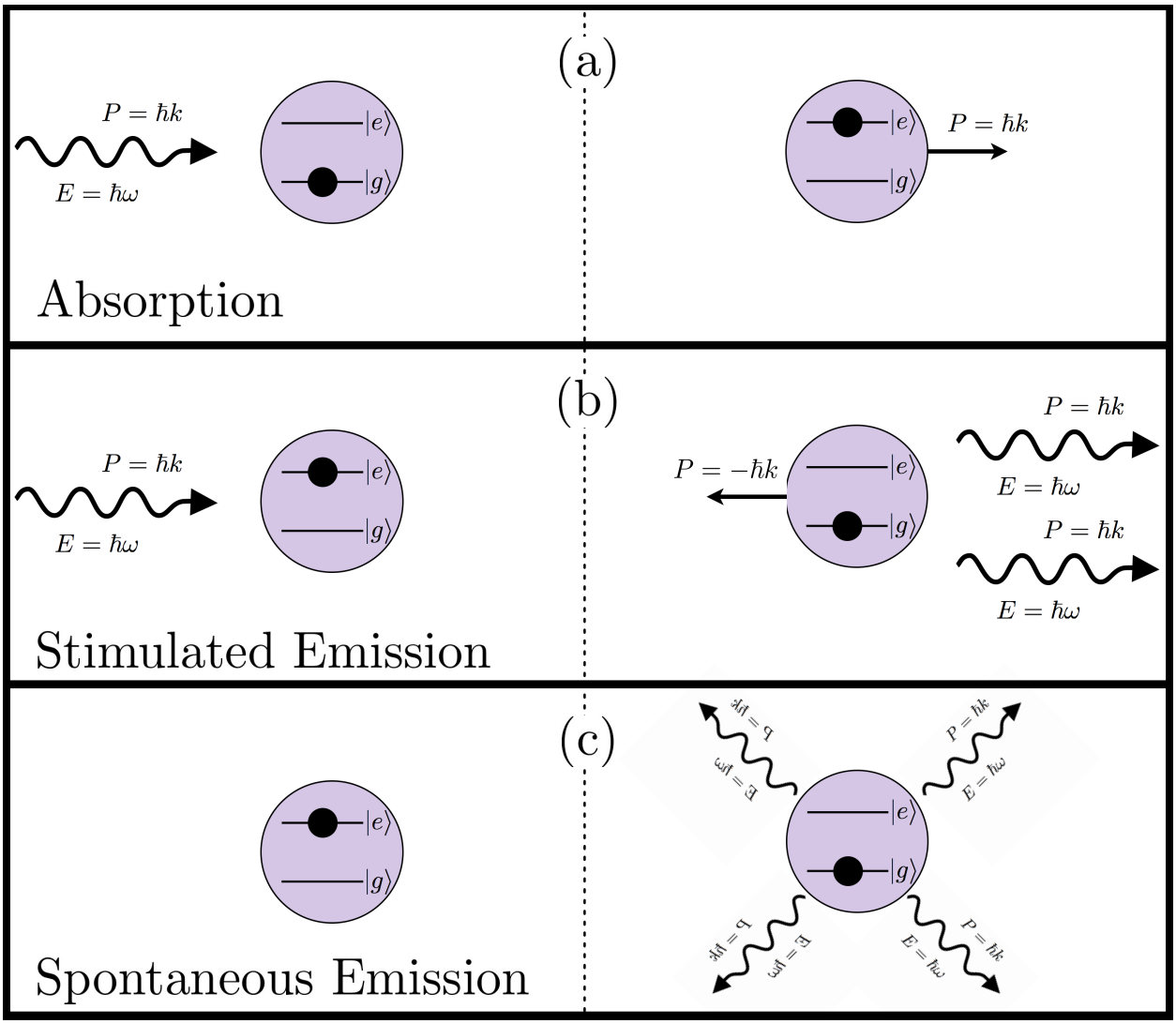

Figure 2.1: The optical field can interact with the atom's motion through the three processes diagrammed here where the field is shown as the oscillating arrows. a) When an atom absorbs energy from the field to transfer between states it must also absorb the momentum carried by the field. b) If the field induces emission and energy is returned to the field the atom must carry momentum in the opposite direction to conserve total momentum. c) In the absence of an applied field an atom in an excited state will undergo SE to the ground state emitting in a random angular distribution (indicated by multiple emissions above). Over the course of many emissions the net momentum gained from this process averages to zero.

radiative force. While the atom is in the excited state, it has a probability of spontaneously decaying back to the ground state. This emission process is not associated with the applied field and emits in a random angular distribution with symmetry about the atom, shown in Fig. 2.1(c). While a single SE will impart momentum to the atom in a random direction (opposite to the emitted field direction), over the course of many SE's the net momentum transfer will average to zero. Each SE is preceded by absorption from the applied field, and this momentum transfer will accumulate. The magnitude of the radiative force is determined by the momentum transferred by the applied field ($\hbar k$) and the rate of the SE process. The rate of SE is determined by the excited state lifetime ($\tau = 1/\gamma$) and the time average value of excited state population $\overline{|c_e(t)|}^2$. Solving the two level system for the steady state populations gives an expression for the radiative force [1]

$$\vec{F} = \hbar\vec{k}\left(\overline{|c_e(t)|}^2\gamma\right) = \frac{\hbar\vec{k}\gamma}{2}\left(\frac{s_0}{1+s_0+(2\delta/\gamma)^2}\right) \tag{2.1}$$

where s_0 is the saturation parameter defined in terms of the laser intensity (I) and saturation intensity ($I_s = \frac{\pi hc}{3\lambda^3\tau}$) as

$$s_0 = \frac{I}{I_s} = 2\left(\frac{\Omega_0}{\gamma}\right)^2 \tag{2.2}$$

The force is at a maximum when $\delta = 0$ and $s_0 \gg 1$. Under these conditions the excited state population is maximized with an average value of 1/2, saturating the force at $F_{rad} = \hbar k\gamma/2$.

2.1.1 Optical Molasses

The magnitude of F_{rad} is determined by the intensity and frequency of the optical field. As the atom accelerates from the force and gains velocity, this velocity will in turn influence the force through a Doppler shift of the laser frequency in the atomic frame. The detuning in the denominator of Eq. 2.1 changes $\delta \to \delta + k\mathrm{v}$, where $k\mathrm{v}$ is the Doppler shift induced by atomic velocity v. Fig. 2.2(a) plots the radiative force as a function of this Doppler detuning and shows there is a finite velocity range for the radiative force ($\pm\gamma/k$). All atoms within this region are accelerated to a velocity where the magnitude of the force approaches zero. This velocity dependence is exploited for the laser cooling process known as optical molasses.

In an optical molasses the laser frequency is purposefully set to be initially red detuned ($\delta < 0$) to the atomic resonance resulting in a force profile shown in Fig. 2.2(b), where the atom requires a velocity traveling opposite to the laser direction to shift its frequency into resonance. A second red detuned beam sent in the opposite direction has a similar

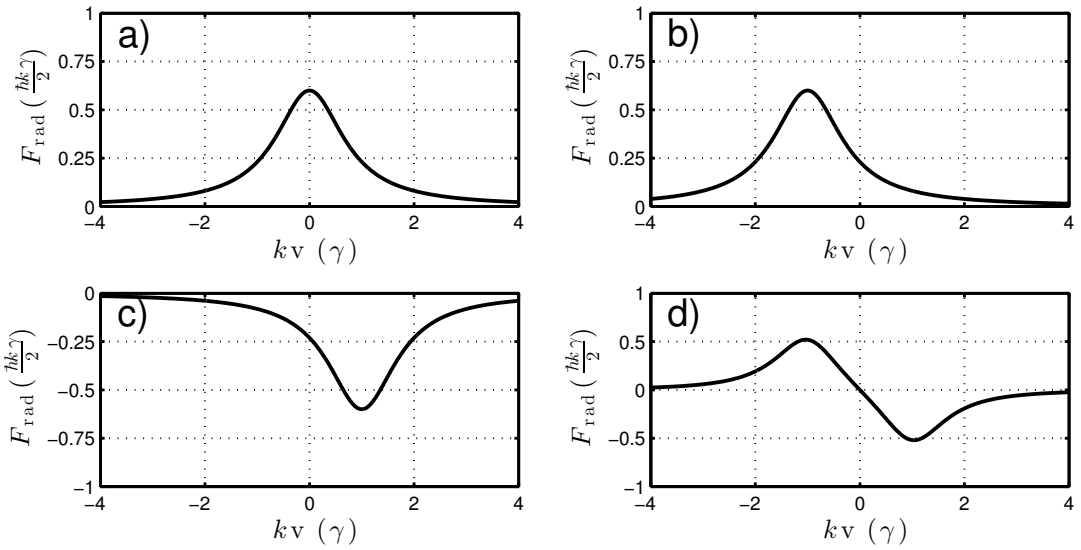

Figure 2.2: The radiative force is plotted vs the Doppler detuning caused by the motion of the atom for $s_0 = 1$ and the laser (a) on resonance $\delta = 0$ and (b) red detuned $\delta = -\gamma$. (c) The direction of the force is reversed for a red detuned laser traveling from the opposite direction. (d) The combined forces from (b) and (c) create an optical molasses that is zero only at $\mathrm{v} = 0$.

force profile, Fig. 2.2(c), but with the force in the opposite direction and shifted to the opposite side of $\mathrm{v} = 0$. When these two laser beams are overlapped, the force profiles sum and result in Fig 2.2(d). The name optical molasses fits because atoms experience a force that always opposes their velocity. Within the velocity capture range ($\pm\gamma/k$), only atoms at $\mathrm{v} = 0$ experience no acceleration. Cooling occurs because an atomic velocity distribution initially spread over $\Delta\mathrm{v} \approx 2\gamma/k$ reduces to a small range around $\mathrm{v} = 0$. The one-dimensional temperature can be expressed in terms of this velocity spread, where $\Delta\mathrm{v}$ is the rms velocity [1].

$$\mathrm{T} = \frac{M(\Delta\mathrm{v})^2}{k_B} \tag{2.3}$$

The optical molasses reduces the velocity spread $\Delta\mathrm{v}$ resulting in a reduction in temperature.

2.2 The Dipole Optical Force

A second type of optical force on atoms occurs because of the induced light shift discussed in Sec. 1.1.3. It was shown that the interaction energy of the eigenstates of the atom are modified by the field. If we consider a standing wave applied to an atom, the Rabi frequency

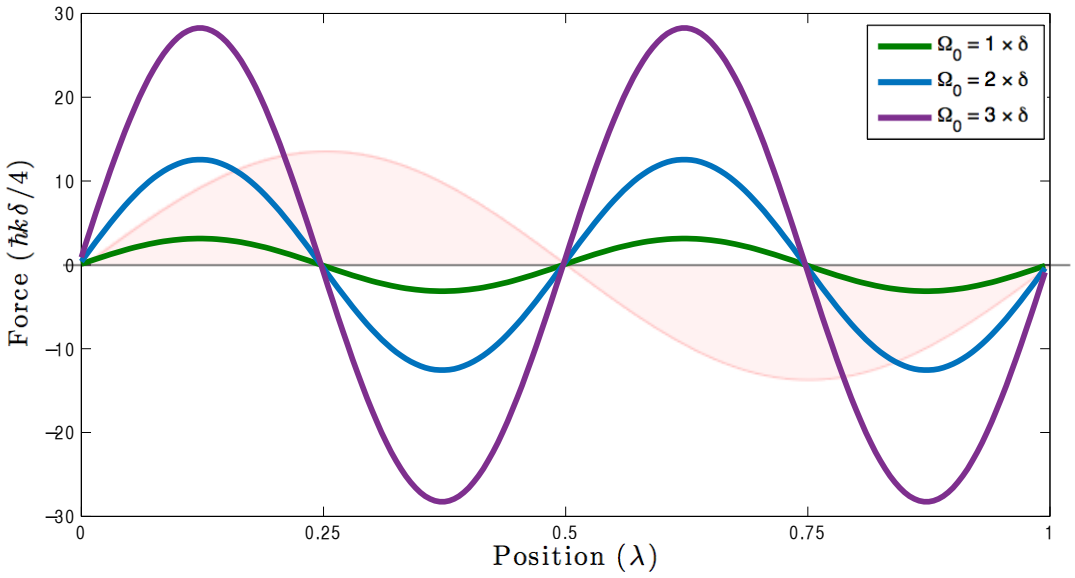

Figure 2.3: The optical dipole force of a standing wave with $\delta < 0$. The electric field is represented in faint red, and the force is plotted for three values of Rabi frequency. The force vanishes at the peaks and nodes of the standing wave, but only the peaks have a stable equilibrium. With $\delta > 0$ the force profile inverts and the nodes become the stable equilibrium points.

displays a spatial dependence.

$$\Omega_0(z) = \Omega_{max} \cos(kz) \tag{2.4}$$

This causes the energy eigenstates of the atom to become spatially varying as shown in Fig. 1.5. This spatial dependence of the potential energy landscape creates the dipole force which we can quantify through the Ehrenfest theorem [1]

$$\vec{F}_{dip} = -\nabla \mathcal{H} = -\nabla \sqrt{\Omega_0^2(z) + \delta^2} \tag{2.5}$$

It is interesting to note that this force does not saturate like the radiative force. This is possible because the dipole force is mediated entirely by stimulated processes of the applied field, and not by SE. The atom can accumulate momentum by absorbing from one direction and emitting into the opposite direction, Fig 2.1(a) followed by Fig 2.1(b). However for single frequency light the force is conservative, only allowing oscillations in the magnitude of the kinetic energy, with no average force acting on the atom.

The radiative force discussed in the previous section will still occur, so the dipole force

becomes most relevant at large detunings that are outside the range of the radiative force. If we assume $\delta \gg \Omega_0$, then the dipole force can be approximated as

$$\vec{F}_{dip} \approx -\frac{\hbar}{4\delta}\nabla\Omega_0^2(z) = -\frac{\hbar\gamma^2}{8\delta I_s}\nabla I(z) \tag{2.6}$$

The magnitude of this force is directly proportional to the laser intensity and has a profile given by the gradient of the spatial variation, shown in Fig. 2.3 for a standing wave pattern.

2.3 The Bichromatic Force

The previous sections explored the forces that arise from simple single frequency optical fields. In general, the atomic response to an applied field can be very complicated if that field has more structure than simple standing or traveling waves. Further, the range of parameters of the applied field can include both strong dipole and radiative effects that interact together.

We will focus on the particular case of a bichromatic standing wave field. The bichromatic field will be composed of two standing waves with detunings equally-spaced from atomic resonance by an amount $\delta \gg \gamma$ (see Fig. 2.4). The two frequencies will be referred to as red and blue in reference to their detuning from resonance (not the actual colors of the fields). When the Rabi frequency and phases of these fields meet certain conditions they produce the bichromatic force. The bichromatic force is unique in its very large magnitude and velocity range and is not restricted by the radiative time limitations associated with SE. In this section three views of the bichromatic force will be presented; the π pulse model, the Bloch equations, and the dressed atom model.

2.3.1 The π Pulse Model

A qualitative description of the bichromatic force can be provided using the 'π pulse' model [22]. In this description we treat the four fields (two frequencies from two directions) by combining fields that share propagation directions. After this we have two traveling waves that are counterpropagating. Let us consider one of these traveling waves. The beam contains two frequencies that are co-propagating. The two frequencies can be rewritten in terms of a single amplitude-modulated carrier (beat pattern)

$$E_r \cos(k_r z - \omega_r t) + E_b \cos(k_b z - \omega_b t) = E_{TW} \cos(\Delta k z/2 - \delta t)\cos(kz - \omega_0 t) \tag{2.7}$$

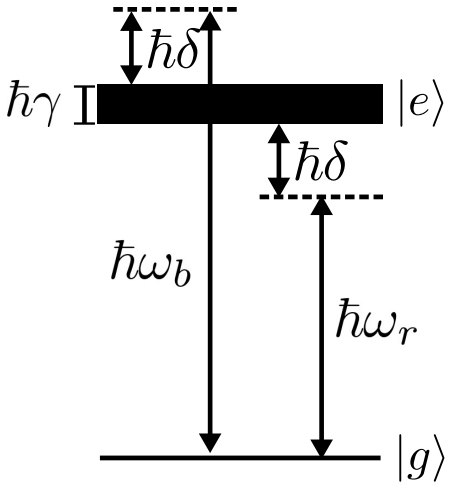

Figure 2.4: The bichromatic optical force uses two frequencies ($\omega_{r,b}$) equally detuned above and below atomic resonance. The magnitude of the detuning is chosen to be much larger than the linewidth of the excited atomic state ($\delta >> \gamma$).

where $\Delta k = 2\delta/c$ and $E_r = E_b = \frac{1}{2}E_{TW}$. Since these two frequencies are spaced equally from resonance, the fast modulation carrier is exactly at the atomic resonance frequency ω_0. The slow amplitude modulation then varies with the magnitude of the detuning. The π pulse model derives its name as the amplitude of the slow oscillation is chosen so that one beat acts as a single π pulse. This occurs when the area of the pulse integrated over the beat envelope is equal to π [16]

$$\int_{-\pi/2\delta}^{\pi/2\delta} \Omega_{TW}(t)\,\mathrm{d}t = \pi \tag{2.8}$$

and corresponds to each frequency having $\Omega_{r,b} = \frac{\pi}{4}\delta$. We can then easily picture the response of the atoms to this single traveling wave. As the beat travels across the atom, the atom transfers for example from the initial ground state to its excited state. We know this is accompanied by a transfer of $\hbar k$ momentum. The next beat will transfer the atom back to the ground state and remove $\hbar k$ momentum. Each beat acts as an individual π pulse able to excite/deexcite and give/take momentum to the atom.

We now turn our attention to the traveling wave that is counterpropagating relative to the first. We time the arrival of the π pulse beat from the opposite direction to coincide with the end of the first π pulse that excites the atom. Then the opposite direction deexcites and removes $\hbar k$ momentum, but now from the opposite direction. This results in a total of $2\hbar k$ momentum transferred to the atom over the course of two π pulses (one from each

direction). This allows an estimation of the magnitude of the bichromatic force

$$\vec{F}_B = \frac{\Delta p}{\Delta t} = \frac{2\hbar k}{\pi/\delta} = \frac{2\hbar k\delta}{\pi} \tag{2.9}$$

Further, the system has returned to its initial state in terms of the internal atomic state and optical fields. Only the momentum has been modified. This allows the entire process to repeat itself as the following π pulse beats arrive, where the only changing parameter (in this simplified model) is the momentum of the atom. This process continues until the cumulative momentum change causes a large enough Doppler shift so that the atoms no longer regard the beats as π pulses.

A simple implementation of the counterpropagating π pulse beats is to use a mirror to retroreflect the bichromatic traveling wave (Eq. 2.7) after interacting with the atoms. Then the relative pulse timing is determined by a phase accumulation of Δkz, where z is the distance between the atoms and the mirror. For a distance of $\Delta kz = \pi/2 \pmod{\pi}$ the π pulses arrive from each direction equally separated in time. The direction of the force is determined by the direction of the first π pulse to interact with the atom, and this will give equal probability of a force in either direction as the atoms continuously enter the field. To give the force a preferred direction, the timing can be modified by changing the phase so that $\Delta kz \neq \pi/2 \pmod{\pi}$, so that it is more probable for one of the directions to occur first. This timing offset will increase as $\Delta kz \to 0 \pmod{\pi}$, and comes at the expense of increasing overlap between the peak intensity regions of the π pulse beats. A good compromise borne out of computational and experimental results is $\Delta kz = \pi/4 \pmod{\pi}$. With this offset it is more likely (3:1), that the desired π pulse will occur first. While the π pulse model provides a simplified picture of the bichromatic force, it ignores many important effects; decoherence from SE, imperfection of the π pulses, and the overlap of the π pulses beats coming from opposite directions.

2.3.2 The Bichromatic Optical Bloch Equations

A more quantitative, but less intuitive, description can be achieved by looking at the atomic dynamics with the optical Bloch equations (OBE). The Bloch description has its roots in the spin response in NMR [23, 24], but can be used to describe any quantum two level system. Additionally, we can include some effects of SE. While not relevant for our short interaction time cooling, it can influence the characteristics of the bichromatic force

on longer timescales. We start with the density matrix for a two level system represented as

$$\boldsymbol{\rho} = \begin{pmatrix} |c_g|^2 & c_g c_e^* \\ c_e c_g^* & |c_e|^2 \end{pmatrix} = \begin{pmatrix} \rho_{gg} & \rho_{ge} \\ \rho_{eg} & \rho_{ee} \end{pmatrix} \tag{2.10}$$

and its time evolution is given by

$$i\hbar\dot{\boldsymbol{\rho}} = [\boldsymbol{\mathcal{H}}, \boldsymbol{\rho}] \tag{2.11}$$

The dipole interaction Hamiltonian in matrix form is

$$\boldsymbol{\mathcal{H}} = \hbar \begin{pmatrix} 0 & \Omega \\ \Omega^* & \omega_0 \end{pmatrix} \tag{2.12}$$

We will first transfer to a rotating frame given by the rotation matrix

$$\boldsymbol{R} = \begin{pmatrix} e^{-\frac{i}{2}(\omega_0 t)} & 0 \\ 0 & e^{\frac{i}{2}(\omega_0 t)} \end{pmatrix} \tag{2.13}$$

so that the Hamiltonian in the rotating frame, following the rotating wave approximation, becomes

$$\tilde{\boldsymbol{\mathcal{H}}} = \boldsymbol{R}\boldsymbol{\mathcal{H}}\boldsymbol{R}^{-1} = \hbar \begin{pmatrix} 0 & \Omega_0 \\ \Omega_0^* & \omega_0 \end{pmatrix} \tag{2.14}$$

and the density matrix becomes

$$\tilde{\boldsymbol{\rho}} = \boldsymbol{R}\boldsymbol{\rho}\boldsymbol{R}^{-1} = \begin{pmatrix} \rho_{gg} & \rho_{ge}e^{-i\omega_0 t} \\ \rho_{eg}e^{i\omega_0 t} & \rho_{ee} \end{pmatrix} = \begin{pmatrix} \tilde{\rho}_{gg} & \tilde{\rho}_{ge} \\ \tilde{\rho}_{eg} & \tilde{\rho}_{ee} \end{pmatrix} \tag{2.15}$$

After these substitutions and including the SE term, Eq. 2.11 becomes

$$\begin{gathered} i\hbar\boldsymbol{R}\dot{\boldsymbol{\rho}}\boldsymbol{R}^{-1} = [\tilde{\boldsymbol{\mathcal{H}}}, \tilde{\boldsymbol{\rho}}] - \left(\frac{d\tilde{\boldsymbol{\rho}}}{dt}\right)_{SE} = \\ i\hbar\left(\dot{\tilde{\boldsymbol{\rho}}} - \begin{pmatrix} 0 & -i\omega_0\tilde{\rho}_{ge} \\ i\omega_0\tilde{\rho}_{eg} & 0 \end{pmatrix}\right) = \tilde{\boldsymbol{\mathcal{H}}}\tilde{\boldsymbol{\rho}} - \tilde{\boldsymbol{\rho}}\tilde{\boldsymbol{\mathcal{H}}} - \begin{pmatrix} -\gamma & \gamma/2 \\ \gamma/2 & \gamma \end{pmatrix} \end{gathered} \tag{2.16}$$

where the term $\left(\frac{d\tilde{\rho}}{dt}\right)_{SE}$ is the decoherence caused by SE [18]. Working through the algebra leads to the follow set of differential equations.

$$\dot{\tilde{\rho}}_{gg} = -i[\Omega_0\tilde{\rho}_{eg} - \Omega_0^*\tilde{\rho}_{ge}] + \gamma\tilde{\rho}_{ee} \tag{2.17a}$$

$$\dot{\tilde{\rho}}_{ge} = -i\Omega_0[\tilde{\rho}_{ee} - \tilde{\rho}_{gg}] + \gamma\tilde{\rho}_{ge}/2 \tag{2.17b}$$

$$\dot{\tilde{\rho}}_{eg} = i\Omega_0^*[\tilde{\rho}_{ee} - \tilde{\rho}_{gg}] + \gamma\tilde{\rho}_{eg}/2 \tag{2.17c}$$

$$\dot{\tilde{\rho}}_{ee} = i[\Omega_0\tilde{\rho}_{eg} - \Omega_0^*\tilde{\rho}_{ge}] - \gamma\tilde{\rho}_{ee} \tag{2.17d}$$

The Bloch representation reduces these equations to a spin vector on the Bloch sphere. The components of the Bloch vector are defined in terms of the density matrix as

$$\mathrm{u}_1 = \tilde{\rho}_{ge} + \tilde{\rho}_{eg} \tag{2.18a}$$

$$\mathrm{u}_2 = i(\tilde{\rho}_{eg} - \tilde{\rho}_{ge}) \tag{2.18b}$$

$$\mathrm{u}_3 = \tilde{\rho}_{ee} - \tilde{\rho}_{gg} \tag{2.18c}$$

and their evolution can be written as

$$\dot{\mathrm{u}}_1 = -\frac{\gamma}{2}\,\mathrm{u}_1 + 2\mathrm{Im}[\Omega_0]\,\mathrm{u}_3 \tag{2.19a}$$

$$\dot{\mathrm{u}}_2 = -\frac{\gamma}{2}\,\mathrm{u}_2 - 2\mathrm{Re}[\Omega_0]\,\mathrm{u}_3 \tag{2.19b}$$

$$\dot{\mathrm{u}}_3 = -2\mathrm{Im}[\Omega_0]\,\mathrm{u}_1 + 2\mathrm{Re}[\Omega_0]\,\mathrm{u}_2 - \gamma(\mathrm{u}_3 + 1) \tag{2.19c}$$

To determine Ω_0 the field can be written as the sum of the two bichromatic traveling waves in Eq. 2.7 as

$$\begin{aligned} E(z,t) &= E_{TW}\cos(\omega_0 t - kz)\cos(\delta t - \Delta kz/2) - E_{TW}\cos(\omega_0 t + kz)\cos(\delta t + \Delta kz/2) \\ &= e^{i\omega_0 t}E_{TW}(e^{-ikz}\cos(\delta t - \Delta kz/2) - e^{ikz}\cos(\delta t + \Delta kz/2)) + c.c \end{aligned} \tag{2.20}$$

where c.c is the complex conjugate of the first term. Then the real and imaginary parts of the Rabi frequency are

$$\mathrm{Re}[\Omega_0] = 2\Omega_{TW}\cos(kz)\sin(\delta t)\sin(\Delta kz/2) \tag{2.21a}$$

$$\mathrm{Im}[\Omega_0] = -2\Omega_{TW}\sin(kz)\cos(\delta t)\cos(\Delta kz/2) \tag{2.21b}$$

The OBE's can be solved to find the dynamics of the internal state populations and their coherences. To determine the force that results, we make use of the Ehrenfest theorem

$$\begin{aligned} F =& -\boldsymbol{\nabla}\boldsymbol{\mathcal{H}} = \mathrm{Tr}(-\tilde{\boldsymbol{\rho}}\boldsymbol{\nabla}\tilde{\boldsymbol{\mathcal{H}}}) = -\hbar(\mathrm{u}_1\,\nabla\mathrm{Re}[\Omega_0] + \mathrm{u}_2\,\nabla\mathrm{Im}[\Omega_0]) \\ =& 2\hbar k\Omega_{TW}[\mathrm{u}_1\,\sin(kz)\sin(\delta t)\sin(\Delta kz/2) + \mathrm{u}_2\,\cos(kz)\cos(\delta t)\cos(\Delta kz/2)] \end{aligned} \tag{2.22}$$

The optical Bloch equations are able to include the effects of SE and atomic velocity, but no longer result in analytic solutions. These equations will be used in the next chapter to numerically simulate the dynamics.

2.3.3 The Doubly Dressed Atom

The dressed atom approach of Sec. 1.1.4 allows another intuitive model of the bichromatic force, which was originally described in Ref. [25] and expanded in Ref. [26]. Here the bichromatic field will be represented slightly differently. Instead of combining the field in groups traveling in the same direction (Eq. 2.7), we will consider each frequency individually. The combination of each red/blue traveling wave from opposite directions is equivalent to a red/blue standing wave.

$$E_r\cos(k_rz - \omega_rt) + E_r\cos(-k_rz - \omega_rt) = 2E_r\cos(kz - \Delta kz/2)\cos(\omega_rt) \tag{2.23a}$$

$$E_b\cos(k_bz - \omega_bt) + E_b\cos(-k_bz - \omega_bt) = 2E_b\cos(kz + \Delta kz/2)\cos(\omega_bt) \tag{2.23b}$$

The single frequency dressed atom was introduced in Sec. 1.1.4. To describe the bichromatic force the dressed atom must be expanded to include the two laser fields at energies $\hbar\omega_{r,b}$. A particular difference of the doubly dressed atom is that each manifold contains an infinite set of levels, all equally spaced at $\hbar\delta$, see Fig. 2.5. Each state is connected to the adjacent states through either the red or the blue detuned field. These states are the basis states for our dressed state Hamiltonian, and the coupling between adjacent states is given by the

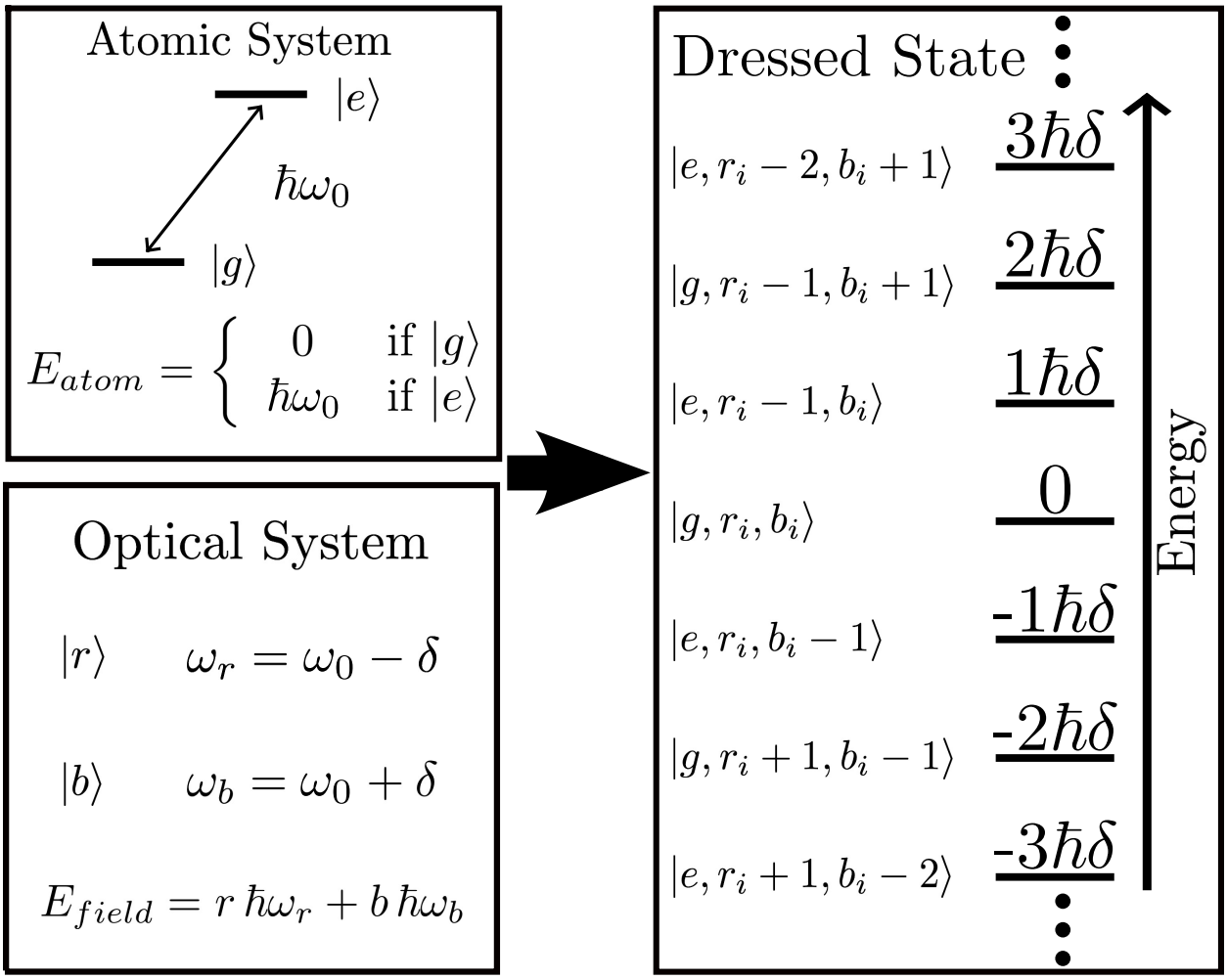

Figure 2.5: The bichromatic dressed states are constructed by combining the atomic states with the energy states of the optical fields. The result is an infinite set of dressed states each separated by $\hbar\delta$ and coupled to its neighboring states through one of the two optical frequencies.

Rabi frequency of the field.

$$\mathcal{H} = \begin{pmatrix}
\ddots & & & & & & & & & & \\
\Omega_r(z) & +4\delta & \Omega_b(z) & 0 & 0 & 0 & 0 & 0 & 0 & 0 & 0 \\
0 & \Omega_b(z) & +3\delta & \Omega_r(z) & 0 & 0 & 0 & 0 & 0 & 0 & 0 \\
0 & 0 & \Omega_r(z) & +2\delta & \Omega_b(z) & 0 & 0 & 0 & 0 & 0 & 0 \\
0 & 0 & 0 & \Omega_b(z) & +1\delta & \Omega_r(z) & 0 & 0 & 0 & 0 & 0 \\
0 & 0 & 0 & 0 & \Omega_r(z) & 0 & \Omega(z)_r & 0 & 0 & 0 & 0 \\
0 & 0 & 0 & 0 & 0 & \Omega_b(z) & -1\delta & \Omega_r(z) & 0 & 0 & 0 \\
0 & 0 & 0 & 0 & 0 & 0 & \Omega_r(z) & -2\delta & \Omega_b(z) & 0 & 0 \\
0 & 0 & 0 & 0 & 0 & 0 & 0 & \Omega_b(z) & -3\delta & \Omega_r(z) & 0 \\
0 & 0 & 0 & 0 & 0 & 0 & 0 & 0 & \Omega_r(z) & -4\delta & \Omega_b(z) \\
 & & & & & & & & & & \ddots
\end{pmatrix} \tag{2.24}$$

Since the fields are independent standing waves at the two frequencies we can write these couplings as a spatially dependent function.

$$\Omega_{r,b}(z) = \frac{|d|\, E_{r,b}}{\hbar} \cos\left(kz \pm \Delta k z/2\right) \tag{2.25}$$

The off-diagonal coupling terms in Eq. 2.24 modify the eigenenergies of the system through light shifts. Diagonalization of the Hamiltonian matrix gives the spatially dependent eigenstates. When $\Omega_r(z) = \Omega_b(z)$ the light shift between all the states are equal from above and below, resulting in no overall change. This corresponds to timing in the π pulse model that would have perfectly overlapped left and right traveling π pulses. We can adjust the phase between the standing waves to match the π pulse model with appropriate beat timings.

In reality, the standing waves have all possible phases on the length scale of $\frac{c\pi}{\delta} \sim$ meters, and since the experiment is on the scale of μm-cm we can consider a single particular phase set by the Δkz terms in Eq. 2.25. If the standing waves are given a phase so that $\Delta kz \neq 0 \,(\mathrm{mod}\, \pi)$ then as the Rabi frequency increases, the eigenstates experience light shifts that depend on the relative intensity of each standing wave at a particular location. For the phase that corresponds to the π pulse picture that resulted in the bichromatic force described in Sec. 2.3.1 ($\Delta kz = \pi/4$), as the Rabi frequency is increased the dressed states experience light shifts, avoided crossings, and eventually exact crossings (see Fig 2.6). The avoided crossings occur when the light shift of one field causes two states to approach, and their

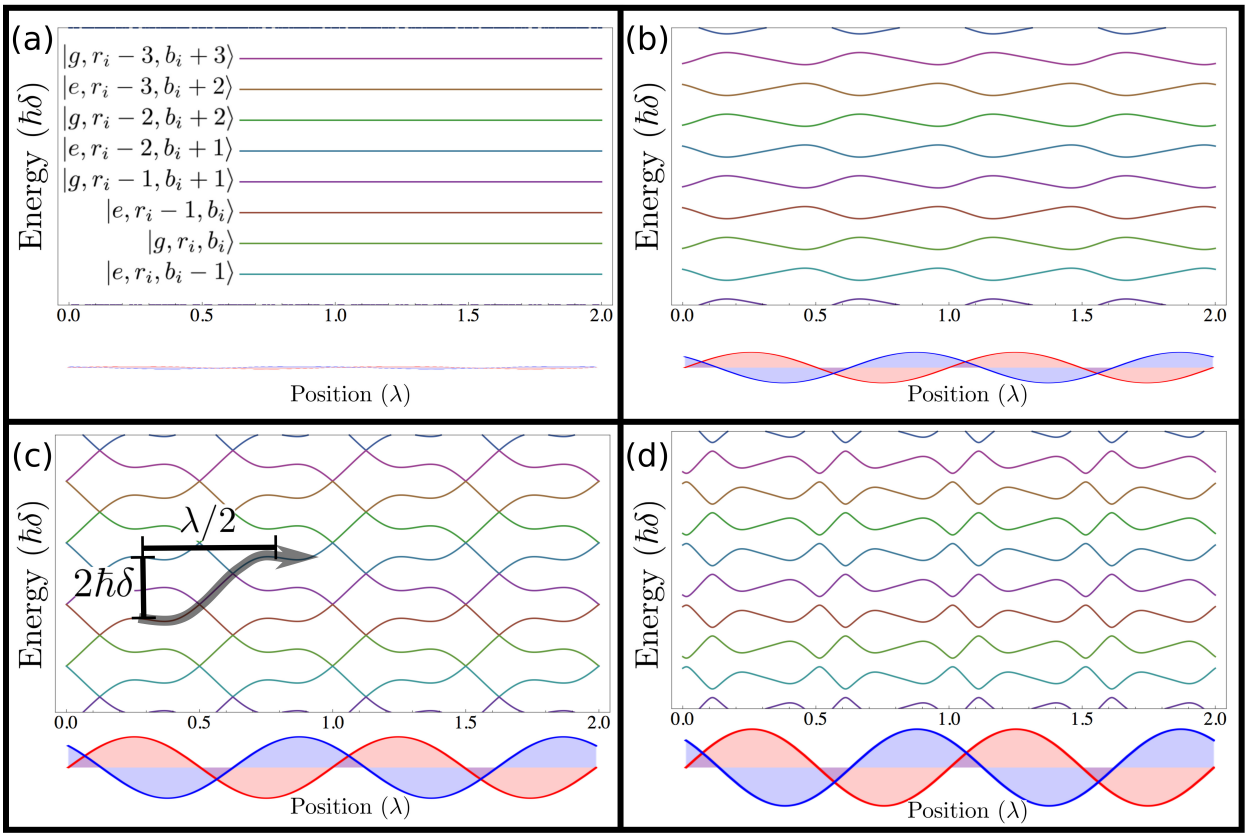

Figure 2.6: The eigenenergies of the bichromatic standing wave with $\Delta kz = \frac{\pi}{4}$ for standing wave intensity (a) $\Omega_{r,b} = 0$, (b) $\Omega_{r,b} = \frac{1}{2}\sqrt{\frac{3}{2}}\delta$, (c) $\Omega_{r,b} = \sqrt{\frac{3}{2}}\delta$, and (d) $\Omega_{r,b} = \frac{5}{4}\sqrt{\frac{3}{2}}\delta$. The standing wave pattern is shown below each energy diagram. At zero intensity, the dressed states are separated in energy by $\hbar\delta$ and then experience light shifts as the intensity increases. At $\Omega_{r,b} = \sqrt{\frac{3}{2}}\delta$ the energy levels have exact crossings that facilitate the bichromatic force, changing by an energy of $2\hbar\delta$ every $\lambda/2$ in distance.

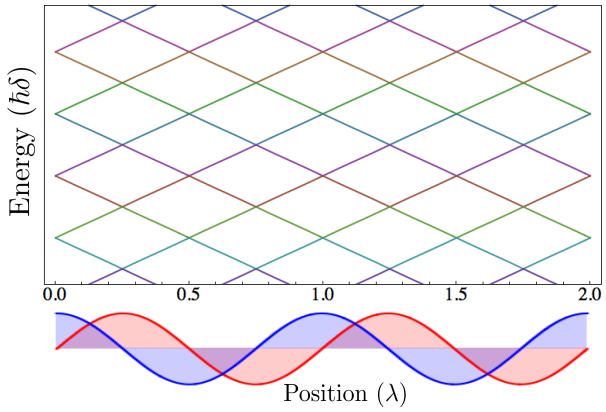

Figure 2.7: The eigenenergies for $\Delta kz = \pi$ have equal probability over the span of $\lambda/2$ to accelerate to the left or right when the atoms enter the optical field, and the force acts as an atomic beamsplitter.

crossing is forbidden because they are coupled by the other field. The exact crossings are allowed because they occur at positions where one of the standing waves has a node and therefore the coupling between alternating states is zero.

The solutions in Fig 2.6 to the dressed atom in a bichromatic field leads to spatially varying energy eigenstates initially similar to the eigenstates found for a single frequency standing wave in Sec. 1.1.3. The oscillating potential energy will cause an atom to accelerate and slow down as it travels along the standing wave. The kinetic energy will change contrary to the dressed state energy (so total energy is conserved), and because the potential is periodic, when it is averaged over a few wavelengths there is no net effect. At $\Omega_r = \Omega_b = \sqrt{\frac{3}{2}}\delta$ the exact crossings first occur and a very interesting structure emerges. Now an atom traveling along the bichromatic standing wave will follow the eigenenergy through each exact crossing so that over the course of each half wavelength the energy of the atom+field has increased by $2\hbar\delta$. Since the energy of the atom+field is increasing the kinetic energy must be decreasing. This monotonically increasing path will continue to slow the atom through a force with magnitude given by

$$F = -\frac{\Delta E}{\Delta z} = -\frac{2\hbar k\delta}{\lambda/2} = -\frac{2\hbar k\delta}{\pi} \tag{2.26}$$

which matches the result found in Sec 2.3.1 with the π pulse model.

The direction of the force is determined by the energy state that the atom is traveling along. If we start with zero bichromatic intensity (the atom starting outside the standing

wave), the atom is in the pure atomic ground state. When the atom enters the light field it will start on a level that corresponds to the initial energy of atom and light fields. In a given energy range of $\hbar\delta$ there is an asymmetry in the probability of landing on a downward vs upward slope as seen in Fig 2.6(c). For the case of $\Delta kz = \pi/4$ the ratio is 1:3, and this can change with different standing wave phase values. For a phase value of $\Delta kz = \pi/2$ the splitting is equal 1:1 as shown in Fig 2.7.

The velocity range of the bichromatic force is limited by Landau-Zener (LZ) transitions that occur between levels at avoided crossings. As the atom's velocity is increased, the amount of time spent traveling through each avoided crossing decreases. The ability of the atom to resolve the energy splitting is inversely proportional to this time ($\Delta E \Delta t \sim \hbar$). The probability for these non-adiabatic crossings to occur is [26]

$$P_{LZ} = e^{-\alpha \frac{\delta/k}{\mathrm{v}}} = e^{-\alpha \frac{\mathrm{v}_B}{\mathrm{v}}} \tag{2.27}$$

where α is a numerical factor of order 1 that depends on the choice of phase. We expect the force to break down at the velocity limit $\Delta \mathrm{v}_B$, where $\delta/4k < \Delta \mathrm{v}_B < \delta/2k$, since the atom will jump from state to state and is unable to continue along a path of increasing/decreasing energy.

Chapter 3

Numerical Simulations

The optical forces described in the previous sections allow experimental control over the motion of individual atoms. This control will be demonstrated in later chapters for two experiments. The first is neutral atom lithography with a bright He^* beam. In neutral atom lithography an optical beam is used to coherently control the position of individual atoms to pattern a substrate in a lithographic process. The second experiment uses the bichromatic force to compress the velocity distribution of He^* atoms on very short time scales ($\approx \tau = 1/\gamma$). Both of these processes required numerical simulations of experimental conditions to assist in understanding the experimental outcomes.

3.1 Lithographic Optical Mask Simulations

Numerical simulations of atomic trajectories were created to investigate the effects of various experimental parameters on the neutral atom lithography process. This Fortran code (Appendix A) is a Monte Carlo simulation of atomic trajectories through an optical mask. The simulation begins with a statistical collection of atoms with properties that reflect the He^* beam produced experimentally. The free atomic motion is modified by the potential created by the standing wave optical mask through the dipole force (Eq. 2.5). The spatial gradient of the dipole potential results in forces on the atoms, and the trajectories to the final atomic position on the lithographic sample surface are recorded. After the motion of the entire statistical collection of atoms is integrated, a histogram of the final positions on the sample surface is made to look at the effectiveness of the optical mask in forming a pattern. Relevant to our experiment are effects related to the velocity distributions of our He^* beam and the strength of the optical mask potential.

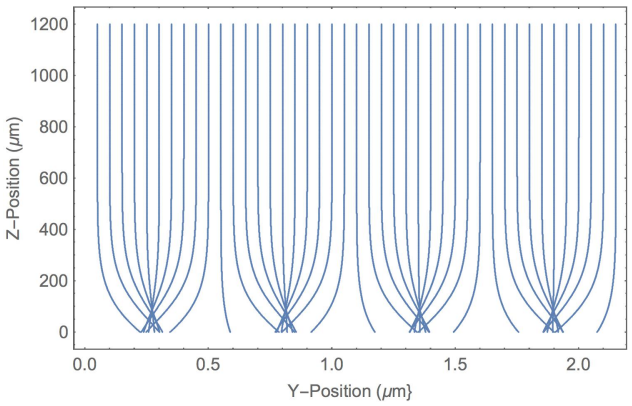

Figure 3.1: The trajectories of He* atoms (shown as blue lines) traveling downward through a standing wave optical mask (not shown) with $\lambda = 1.08\,\mu$m forming a pattern along the horizontal axis at $Z = 0$. At the correct optical intensity, determined by P_f, the optical mask acts as an array of lenses for the atoms, spaced every half wavelength, focusing onto the sample surface.

The ability to pattern the He* beam derives from the dipole interaction. If a standing wave is formed, then the beam acts as a continuous set of micro lenses spaced at $\lambda/2$. These lenses will focus atoms as they travel through the laser field as shown in Fig. 3.1, where atoms are traveling down from high z values to the sample surface at $z = 0$ μm. Previous studies determined that for a Gaussian laser beam, the optimal power for an optical mask to produce the smallest features occurs with a dipole force that focuses an incoming atomic beam onto the center of the laser beam [27]. This occurs at a power independent of beam size and given by

$$P_f = 5.37\,\frac{\pi(\mathrm{E}_{KE})I_s\delta}{\hbar\gamma^2 k^2} \tag{3.1}$$

where E_{KE} is the kinetic energy of the atom [27]. This is used as the starting point for the experimental simulation, and relevant He* beam parameters are included to study their effects on the focusing process.

The geometry of the experimental simulation is shown in Fig 3.2. A gold sample is in the x-y plane and the optical mask standing wave is formed along the y-axis over the gold with its beam center at the sample surface. The optical mask is characterized by three parameters; wavelength (λ), Gaussian waist (w_0), and optical power. The power is defined relative to P_f from Eq. 3.1. The He* beam travels along z toward the sample surface with each atom beginning a distance of $3w_0$ from the sample surface. The classical equations of motion are given by free evolution from initial He* positions and velocities under the influence of the

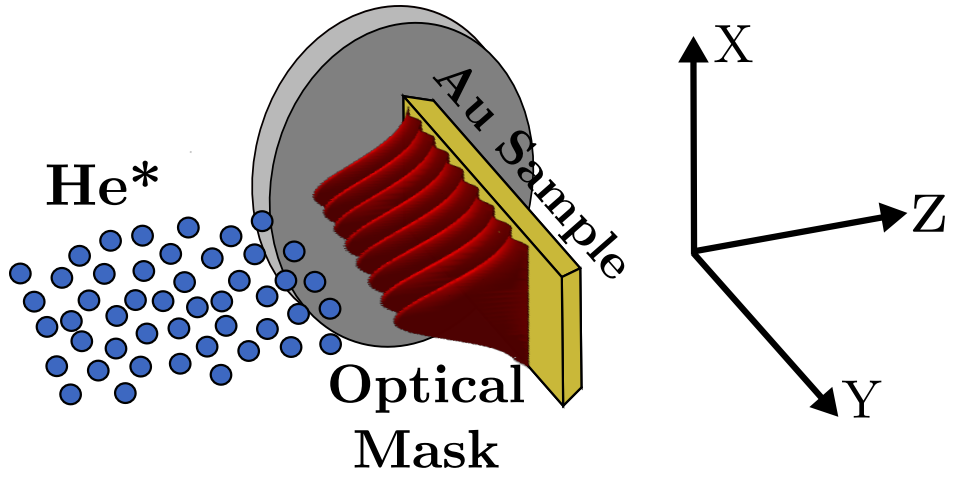

Figure 3.2: The geometry used for the lithography simulation. The He*, represented in blue, travel toward the gold lithography sample inside the vacuum chamber. A laser beam travels parallel to the sample surface and is retro-reflected from a high quality mirror placed perpendicular to the sample. The resulting standing wave forms the optical mask (shown in red) used to pattern the He* beam.

dipole force of the optical mask and integrated to the sample surface. The initial conditions of the He* atoms are randomly populated from probability distributions chosen to reflect the experimental conditions. The initial positions in the x-y plane are chosen from random over a 4μm $\times$ 4μm region. The He* beam has a distribution of velocities in the longitudinal propagation direction given by a Maxwellian profile centered at 1125 m/s with width $\sim$ 400 m/s. A particularly worrisome experimental reality is the transverse velocity spread of the atomic beam, which produces a divergence entering the optical mask 'lens', smearing the location of the focus. The initial velocities in the x and y directions are determined by Gaussian distributions with variable widths $\Delta \mathrm{v}_t$.

The final positions of each He* atom on the sample surface are plotted in Fig. 3.3 for a set of laser powers and transverse velocity distributions. Above each scatter plot is a histogram that integrates over the x axis and bins the y axis into 10 nm bins. It is immediately obvious that the transverse velocity distribution has a detrimental effect on the focusing ability. It is true that an optical mask power of P_f gives the narrowest features as reported in [27], but only for $\Delta \mathrm{v}_t = 0$. It was determined that the power should be slightly increased to improve the He* localization at the sample surface to compensate transverse velocity spread. These results also indicate that the experimental transverse velocity spread should be reduced as much as possible, and led to the implementation of an extra optical molasses stage in our

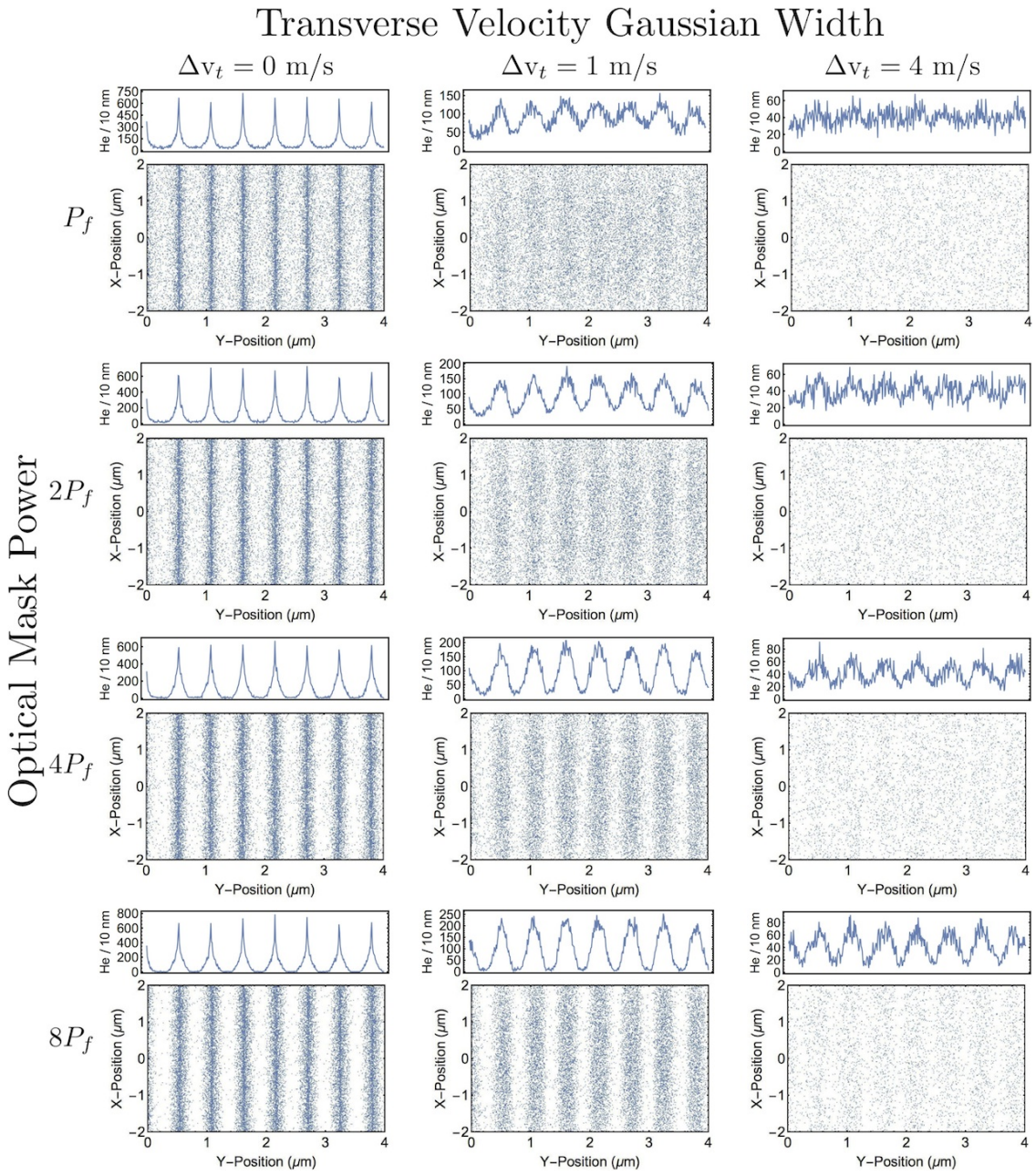

Figure 3.3: Monte-Carlo simulation of atom patterning with an IR optical mask. Atoms initially randomly distributed over a $4\mu\text{m} \times 4\mu\text{m}$ area are patterned after they travel through the IR optical mask. The location where each atom hits the sample surface is shown with a blue dot. Above each scatter plot the distribution of atoms is shown summed over the vertical dimensions and horizontally binned into 10 nm bins. Any transverse velocity spread in the He* has a detrimental effect on the pattern formation that can be compensated with increased optical power at the expense of feature size.

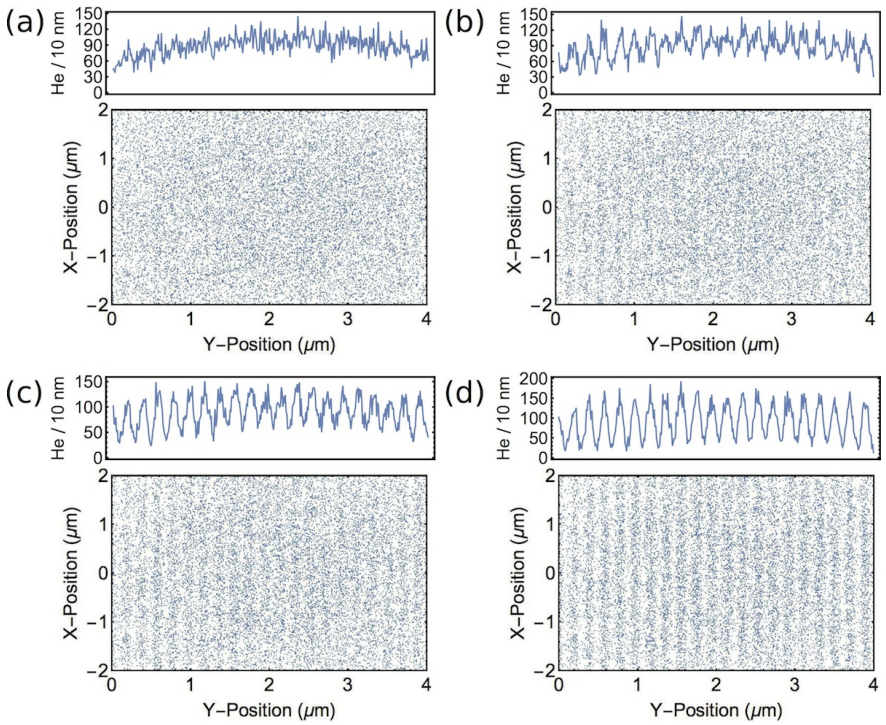

Figure 3.4: Monte-Carlo simulation of atom patterning with an UV optical mask. The UV optical mask ($\lambda = 389$ nm) is more sensitive to the He* transverse velocity spread ($\Delta v_t = 1$ m/s) because of the smaller feature spacing. The plots above show the final atomic distribution for (a) P_f, (b) $4P_f$, (c) $8P_f$, and (d) $16P_f$. The results show that a higher optical power is required for the UV than the IR to compensate for the transverse velocities.

He* collimation to reduce the experimental transverse velocity spread to $\Delta v_t \sim 1$ m/s.

Following the successful experimental patterning using the IR ($\lambda = 1083$) nm optical mask, the experiment was modified to use the UV transition ($\lambda = 389$ nm) to create a pattern with a smaller pitch (194 nm). The reduced distance between each optical mask 'lens' could be more sensitive to the transverse velocity distribution, so the simulation was run for $\lambda = 389$ nm and $\Delta v_t = 1$ m/s. The results are shown in Fig. 3.4 and indicate an increased sensitivity to the transverse spread that should also be compensated by higher optical power.

3.2 The Bichromatic Optical Bloch Equations

The π pulse model and dressed atom model provide intuitive pictures of the bichromatic force. They are also able to provide estimates of the force magnitude and velocity limits, but

to look at the detailed dependence of the bichromatic force on the variation of parameters the optical Bloch equations (OBE) must be solved. There are no analytic solutions to the OBE derived in Sec. 2.3.2 for the bichromatic optical fields, so the equations must be solved numerically which is possible with modest computing power.

3.2.1 Numerical Solutions of the OBE's for the Bichromatic Force

The original bichromatic force Fortran code was developed in Heidelberg by the authors of [25] and subsequently modified in Ref. [28]. It has been used to create force maps as a function of velocity (v), Rabi frequency (Ω_0), and phase (Δkz). It required only minor modifications to solve for the He* UV transition. The simulation uses a constant velocity approximation, keeping the velocity fixed and using $z = \mathrm{v}t$. The Bloch equations are integrated until they reach steady state. Once they reach steady state Eq. 2.22 is used to calculate the magnitude of the force each time step. An effective force is found by averaging these values over time. All the results shown in this section are in good agreement with previous calculations [22,28–30].

The calculated force vs velocity depends on the bichromatic Rabi frequency as shown in Fig. 3.5. We know from the other bichromatic force models that the force magnitude and velocity range scale with δ, so the plots are scaled where the Rabi frequency is given by Ω_0/δ, the velocity v/v_B with $\mathrm{v}_B = \delta/k$, and F/F_B with $F_B = \hbar k\delta/\pi$. The force extends through a velocity range of $\pm\mathrm{v}_B/4$ to $\pm\mathrm{v}_B/2$ depending on the choice of Ω_0. The lineouts of the force at particular values of Ω_0 show that the magnitude is strongest near the $\Omega_0 = \sqrt{\frac{3}{2}}\delta$, the value predicted by the dressed atom picture. Here the force is strongest, but the velocity range is narrow at $\pm\mathrm{v}_B/4$. The force extends over the widest velocity range at $\Omega_0 \sim 1.15\,\delta$ at the cost of reduced magnitude. The force is more sensitive to Ω_0 in this region since it attempts to bridge the small region of overlap between the features around $\mathrm{v} = 0$ and $\mathrm{v} = \pm\mathrm{v}_B/2$.

We know from the π pulse model in Sec. 2.3.1 that the relative phase between the fields can be related to the π pulse timing, so that we should expect that this determines the directionality of the force. Fig. 3.6 shows the force reversal when the phase changes by $\pi/2$. The sharp fall off of the force with changes in phase is in part due to the dependence of the optimal Rabi frequency with phase. It was shown in Ref. [26] that the value of Ω_0 required for the dressed states to have exact crossings changes with phase.

If we look at the force vs velocity for $\Omega_0 = 1.24\delta$ and $\Delta kz = \pi/4$ (Fig. 3.5), the profile has a top hat type shape. All atoms within the velocity range of the force will be accelerated to positive velocities until the force vanishes. This will cause an accumulation of atoms near $\mathrm{v}_B/4$.

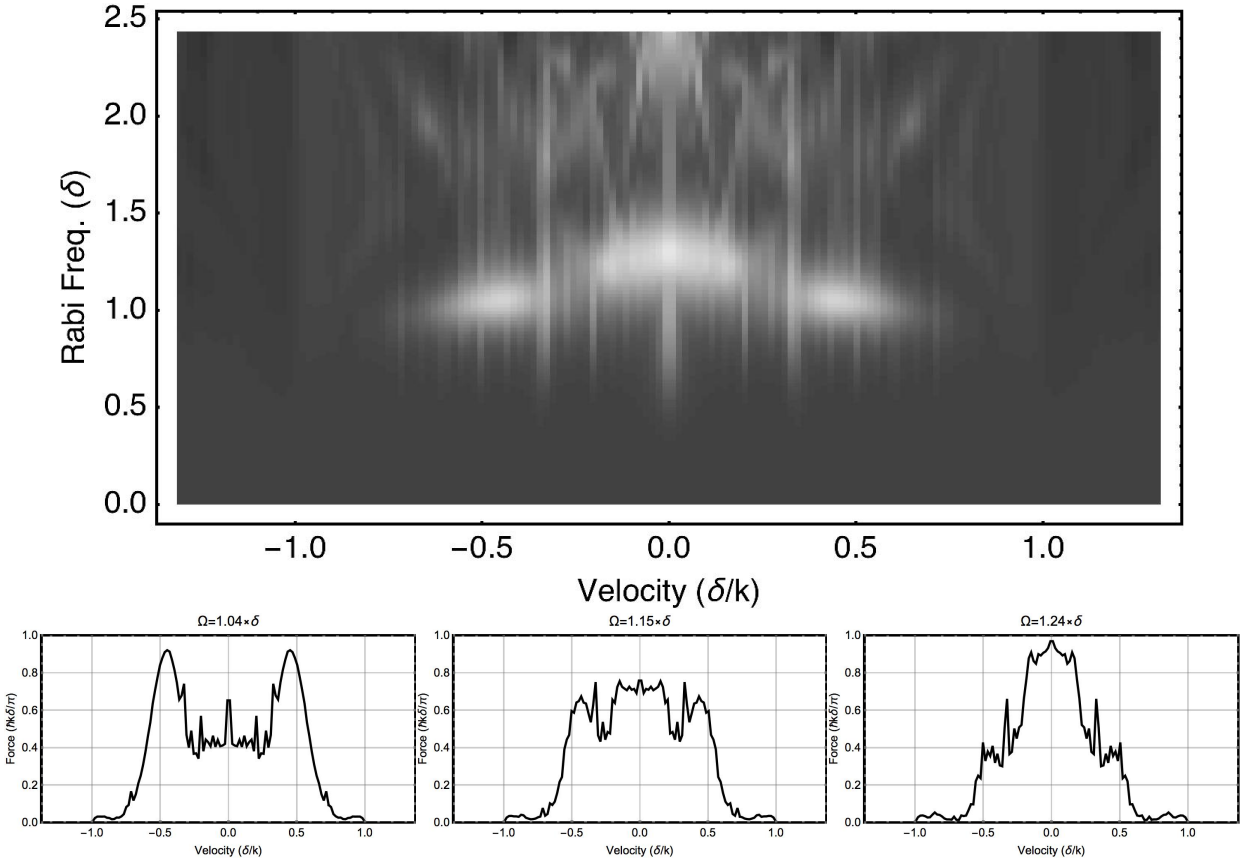

Figure 3.5: Top: Magnitude of the bichromatic force as a function of velocity and Rabi frequency for $\delta = 15.1\gamma$ and $\Delta\phi = \pi/4$. The white regions correspond to larger magnitude and black signifies no force. Bottom: Three lineouts taken from the plot above of the force vs velocity at particular values of Rabi frequency ($\Omega_0 = 1.04\,\delta$, $\Omega_0 = 1.15\,\delta$, $\Omega_0 = 1.24\,\delta$).

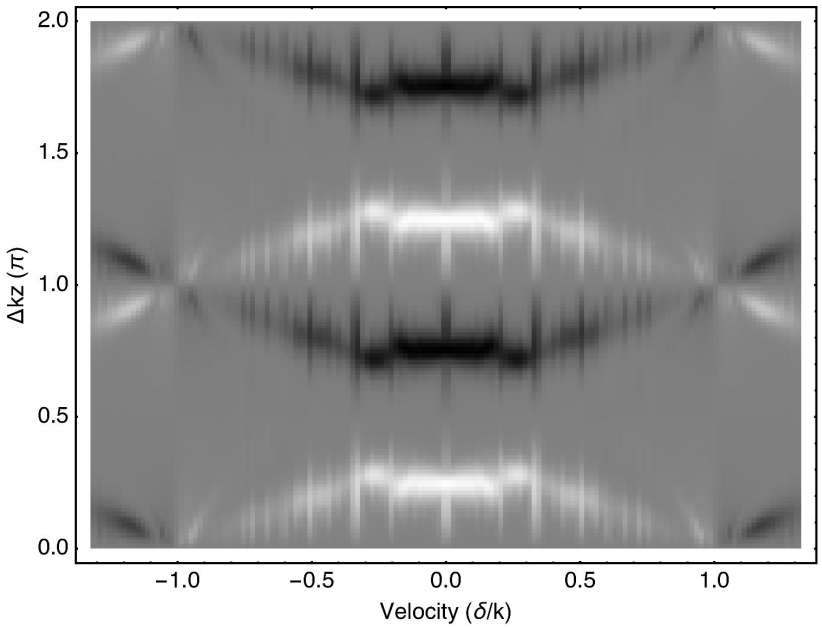

Figure 3.6: The magnitude of the bichromatic force is shown as a function of velocity and standing wave phase. The white regions indicate a strong force in the positive z direction, while the black regions indicate a strong force in the negative z direction.

3.2.2 Simulating Atomic Dynamics in a Bichromatic Field

The previous version of the bichromatic force numerical simulation calculates the atomic response and averages the force in time after the Bloch equations reach steady state. This will not reflect the experiment of a short interaction time bichromatic force used to look for cooling without SE. The steady state was previously important because the transient response is strongly dependent on initial conditions, which for previous experiments were not important because of the long interaction times. The code was modified to more carefully take account of these parameters, and is attached in Appendix B.

The atomic motion through the standing wave, which is important in the dressed state picture, means the constant velocity approximation is no longer valid. The acceleration felt by the atom depends on the value of the Bloch vector components and the atom's position in the bichromatic field. This acceleration will influence the atom's trajectory through the field, and the evolution of the Bloch vector changes depending on the path taken. In this way the history of the atom in the field is important to accurately determine its response.

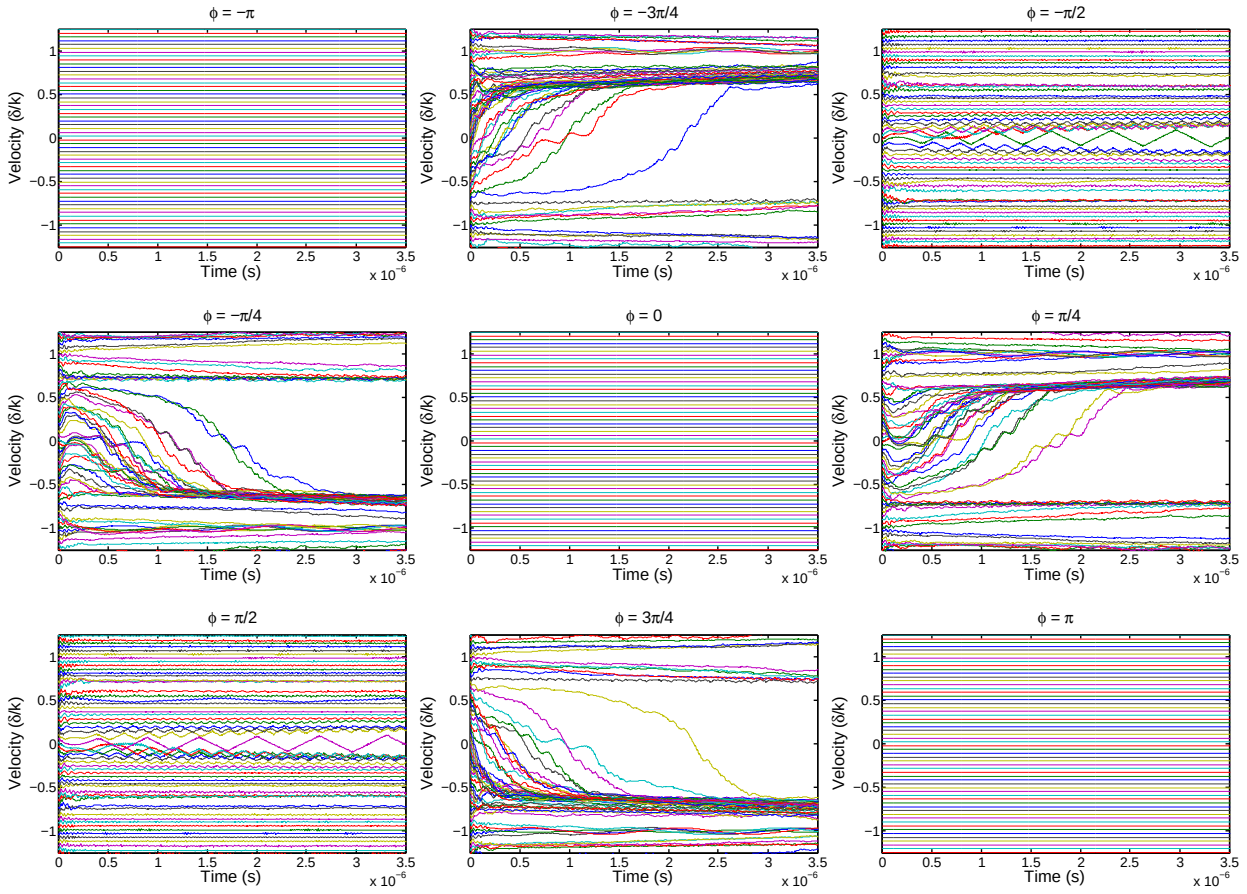

Figure 3.7: Each plot shows atomic velocity trajectories in time after entering the bichromatic field. The trajectories are shown for equally-spaced initial velocities between $\pm 1.25 \mathrm{v}_B$. The response is shown or different values of $\phi = \Delta k z$ with $\Omega_0 = \sqrt{\frac{3}{2}}\,\delta$ kept constant. For $\phi = \frac{\pi}{4} \pmod{\pi}$ the bichromatic force compresses the central velocity distribution showing cooling.

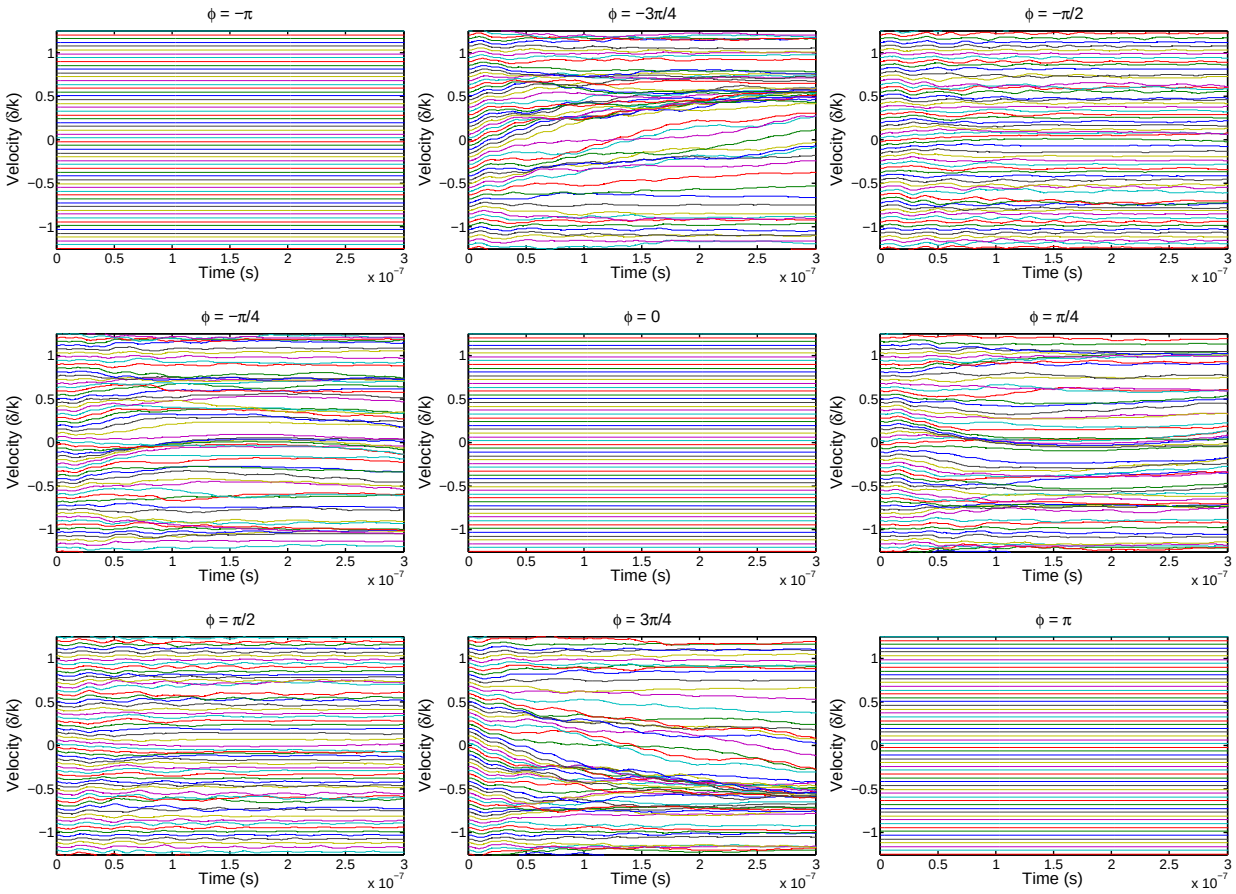

Figure 3.8: Each plot shows the atomic velocity trajectories for the initial transient time in the bichromatic field with the same parameters as Fig. 3.7. The accumulation of atoms is less pronounced on this time scale, but still exists.

The complete set of differential equations for the OBE (Eq.'s 2.19) and atomic motion are

$$\dot{u}_1 = -\gamma/2\, u_1 - 4\Omega_0 \sin(\phi/4) \sin(kz) \sin(\delta t)\, u_3 \tag{3.2a}$$

$$\dot{u}_2 = -\gamma/2\, u_2 - 4\Omega_0 \cos(\phi/4) \cos(kz) \cos(\delta t)\, u_3 \tag{3.2b}$$

$$\dot{u}_3 = 4\Omega_0[\sin(\phi/4) \sin(kz) \sin(\delta t)\, u_1 + \cos(\phi/4) \cos(kz) \cos(\delta t)\, u_2] - (\gamma - 1)\, u_3 \tag{3.2c}$$

$$\dot{z} = v \tag{3.2d}$$

$$\dot{v} = \frac{F_B}{M} = -\frac{2\hbar k \Omega_0}{M}[\cos(\phi/4) \sin(kz) \cos(\delta t)\, u_1 + \sin(\phi/4) \cos(kz) \sin(\delta t)\, u_2] \tag{3.2e}$$

Integrating the atomic dynamics in the bichromatic field gives trajectories for each of the five time dependent variables in Eq. 3.2. The velocity trajectories are the most informative as they will show changes induced by the bichromatic force, and we can also look for accumulations of atoms at a particular velocity, showing cooling.

The atoms begin initially in their ground state before entering the field so that $u_1(0) = u_2(0) = 0$ and $u_3(0) = -1$. Fig. 3.7 shows a set of velocity trajectories for equally-spaced starting velocity values as a function of interaction time and different phase values for $\Omega_0 = \sqrt{\frac{3}{2}}\delta$. We saw in the previous section (Fig. 3.6) that the phase determines the direction of the force and repeats every change of π. The same behavior is demonstrated here. The bichromatic force accelerates all atoms in its velocity limits, and this acceleration causes the trajectories to either slope upward or downward depending on the direction of the force. The acceleration stops when the atoms reach a region of velocity where the force goes to zero, and the atomic trajectories accumulate at a velocity that corresponds to the edge of the force profile. At phases of $\Delta kz = \pm\pi/2$ the bichromatic beam acts as an atomic beamsplitter. This can be understood from the π pulse model as having equally-spaced beats in time. In this case, there is no method to institute a preferential direction since the first π pulse seen will be determined by the timing of the atom entering the light field.

The trajectories shown in Fig. 3.7 have long interaction times, and the dynamics can be largely described by what was known from the steady state force calculations. However the dynamics on short time scales, shown in Fig. 3.8, are less intuitive. We can see that the accumulations are less pronounced, but still exist. More interesting is that while we should expect identical trajectories for atoms at phases separated by π, the results show the trajectories are different. This led to the understanding that in this transient regime all initial conditions are relevant, including starting position and time.

The starting position is relevant over the wavelength scale as shown in Fig. 3.9. Each of these initial positions causes the trajectories to take different paths on the short time scales,

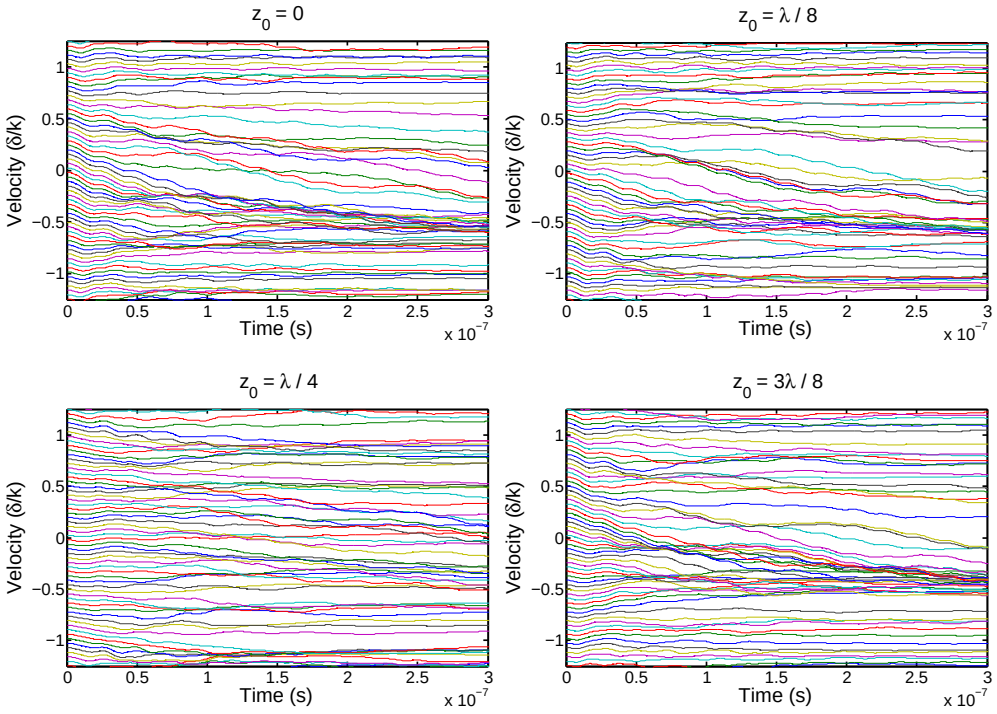

Figure 3.9: The velocity trajectories for $\Omega_0 = \sqrt{\frac{3}{2}}\,\delta$ and $\Delta kz = 3\pi/4$ change for different values of starting position (z_0). On long time scales (not shown) the trajectories for different starting positions converge to the result shown in Fig. 3.7. The trajectories are identical for a relative change of $\Delta z_0 = \lambda/2$.

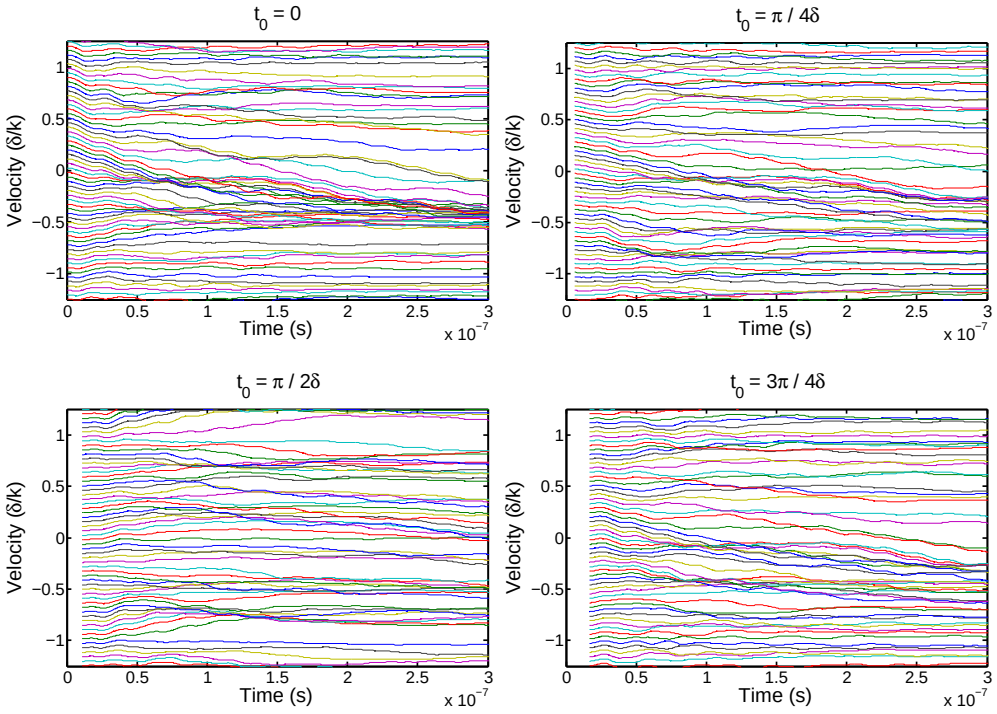

Figure 3.10: The velocity trajectories for $\Omega_0 = \sqrt{\frac{3}{2}}\,\delta$ and $\Delta kz = 3\pi/4$ change for different values of starting time (t_0). On long time scales (not shown) the trajectories for different starting times converge to the result shown in Fig. 3.7. The trajectories are identical for a relative change of $\Delta t_0 = \pi/\delta$.

but converge on longer time scales and repeat every $\lambda/2$. We can understand this response from the dressed atom model of Sec. 1.1.4 noting the dressed state structure over a distance of $\lambda/2$. In Fig. 2.6 over a region of $\lambda/2$ the path of the dressed state has a slope in one direction over 3/4 of the region, while for 1/4 of the region it is sloped in the other direction. This is reflected in Fig. 3.9 where three of the four initial positions immediately cause the trajectories to accelerate to negative velocities.

The starting time has a similar effect on the trajectories shown in Fig. 3.10, repeating every π/δ. This is best understood from the π pulse model. Changing the initial time corresponds to changing which π pulse beat direction is seen first. Because they are timed to be asymmetric to favor a particular direction, we expect that 3/4 of the time the correct π pulse is seen first, while 1/4 of the time the wrong π pulse is first. From these results we were able to determine that the differences in the trajectories for phases separated by π in Fig. 3.8 are actually caused by a shift in the starting time based on how the phase is defined in the simulation program.

The initial position and time are not controlled experimentally since the He^* beam width spans many wavelengths and He^* atoms are continuously entering the optical interaction region. The simulation can be run for all combinations of v_0, t_0, and z_0, but the number of atomic trajectories that need to be calculated can easily become computationally unreasonable when trying to account for all these parameters. This is because all permutations of initial conditions are required to properly account for all experimental possibilities. A few numerical simulations were run where atomic trajectories were calculated for each initial velocity multiple times with different starting positions (15 equally spaced over λ) and starting times (15 equally spaced over $2\pi/\delta$) and all combinations of the two. With so many trajectories it became necessary to bin and histogram the finally velocity distribution after the interaction, shown in Fig. 3.11. At this point there are so many initial parameters that very little understanding of the detailed dynamics can be gained, but the numerical simulations still indicate that cooling should occur on timescales of a few hundred nanoseconds.

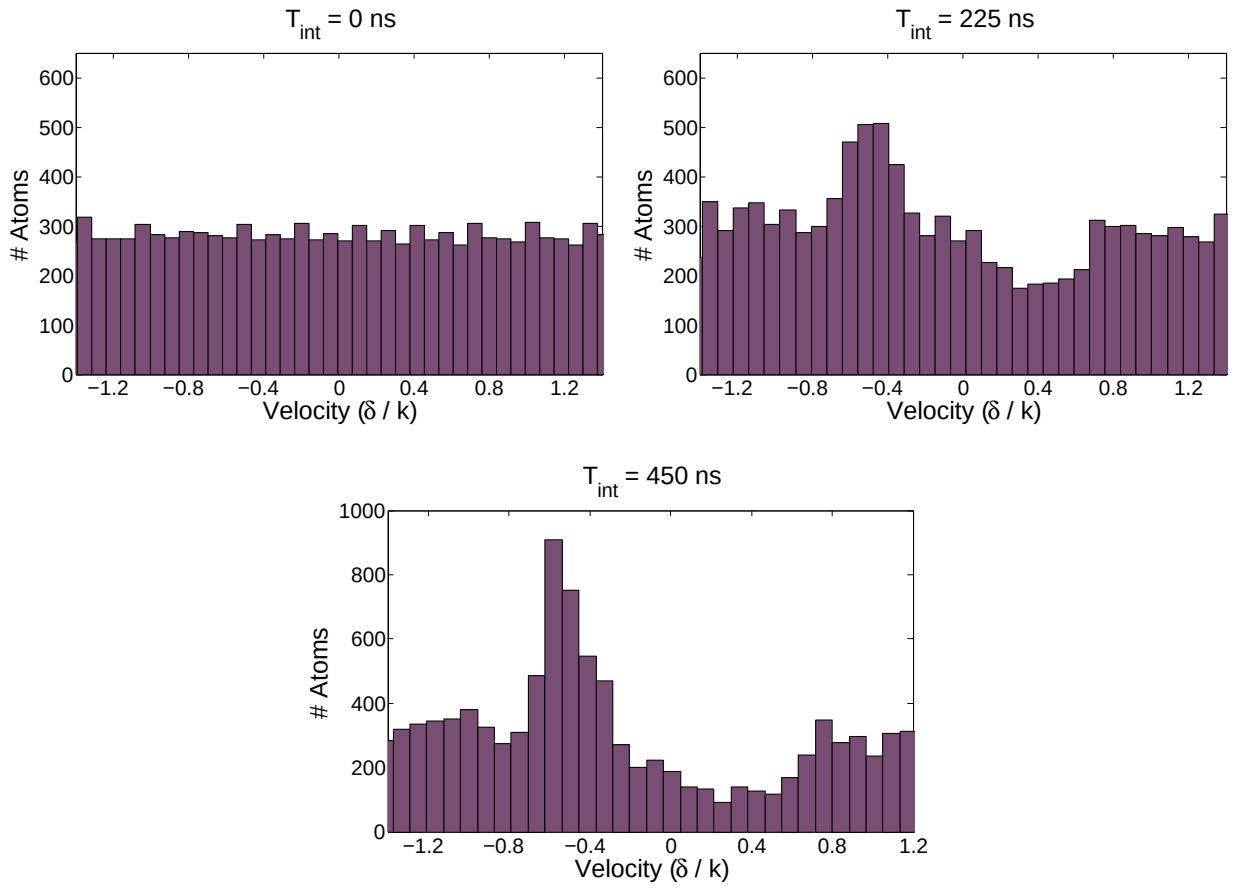

Figure 3.11: The trajectory for each initial velocity was calculated for all permutations of 15 initial positions ($z_0 = 0 \leftrightarrow \lambda$) and 15 initial times ($t_0 = 0 \leftrightarrow \pi/\delta$). The final set of velocities after an interaction time $\mathrm{T_{int}}$ are histogrammed into bins $0.0375\mathrm{v}_B$ wide.

Chapter 4

Experimental Apparatus

4.1 Vacuum System

The vacuum chamber used for these experiments is largely inherited and is also well described in [31–33]. The chamber has three main segments shown in Fig. 4.1; the He* source, interaction region, and lithography chamber. It is predominately constructed with Conflat® vacuum flanges, but there are some o-ring seals. The He* source region is nearly isolated from the rest of the vacuum chamber except for a small exit hole. The entire system is kept under vacuum with two Pfeiffer TPH-330 turbomolecular pumps (turbos) attached to the source and interaction region. The exhaust of each turbo is pumped by a dedicated mechanical pump. The turbo pump on the source region is pumped with a Pfeiffer Duo Seal 110 direct drive pump, while the interaction region turbo is pumped with a Welch 1376. These pumps are able to keep the entire vacuum system in the 10^{-7} Torr pressure range. This pressure is limited by a combination of leaking from o-ring seals in the He* source and doors to the lithography chamber, and outgassing from certain parts not designed for high vacuum.

The interaction region contains four windows directly following the He* source exit allowing two dimensional optical access transverse to the He* beam direction. These windows are antireflection (AR) coated for the IR and UV wavelengths. Downstream, just past the windows are a set of parallel metal plates kept at 1000 volts relative to ground to use electric fields to sweep any charged particles out of the He* beam and into the metal walls of the vacuum chamber. About 25 cm downstream from the exit of the He* source are another two vacuum windows allowing access for additional laser beams, or a line of sight to image the front microchannel plate with phosphor screen detector (MCP/PS) that can be lowered from

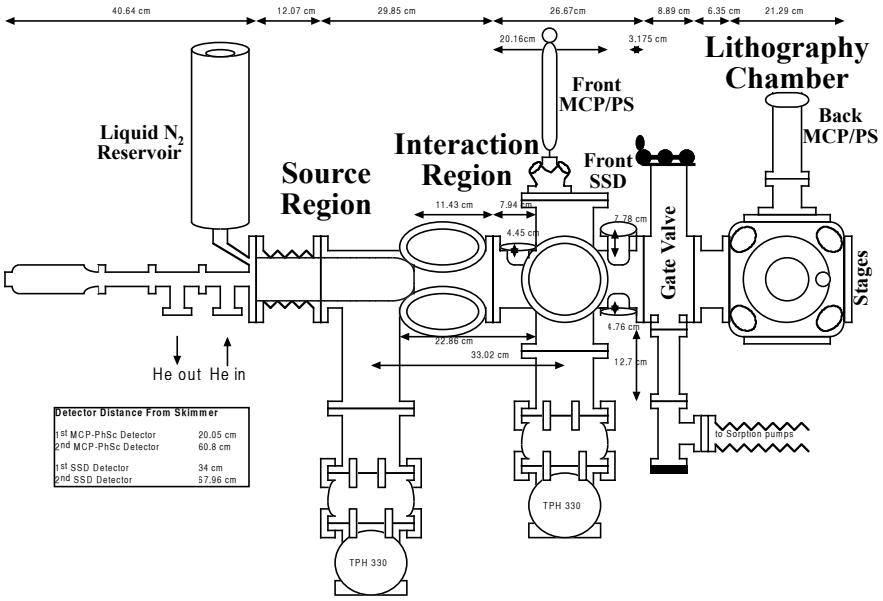

Figure 4.1: The He* beam apparatus is a stainless steel chamber pumped by two turbomolecular pumps. The vacuum system has three main segments; the He* source, the interaction region, and the lithography chamber. Adapted from Fig. 3.1 in [31].

above into the He* beam path. After this second set of windows and before the lithography chamber there are two mechanical feedthroughs that can be used to position the front stainless steel detector (SSD) into the He* beam path. The interaction chamber is then connected to the lithography chamber with a gate valve.

The lithography chamber also has two windows for optical access. Initially both windows were on hinged doors with o-ring seals, allowing easy access when the lithography region is brought up to atmospheric pressure. One of these windows eventually had to be replaced with a standard uncoated Conflat® window because the AR coating for the IR wavelength on the hinged doors caused very large attenuation of the UV laser beam. Inside the lithography chamber attached to the back flange directly facing the He* source are a set of electronically controlled stages. These stages can be computer controlled through LabVIEW or with a program written in Visual Basic designed for doing He* lithography [28]. The stages are used to position or scan either the rear SSD or a lithography sample, and have a mount designed to attach either. There are two mechanical feedthroughs near the gate valve that are used to attach mechanical beam blocks, or a metallic mesh used to pattern the He* beam for lithography experiments. There is also an residual gas analyzer that is used for vacuum troubleshooting.

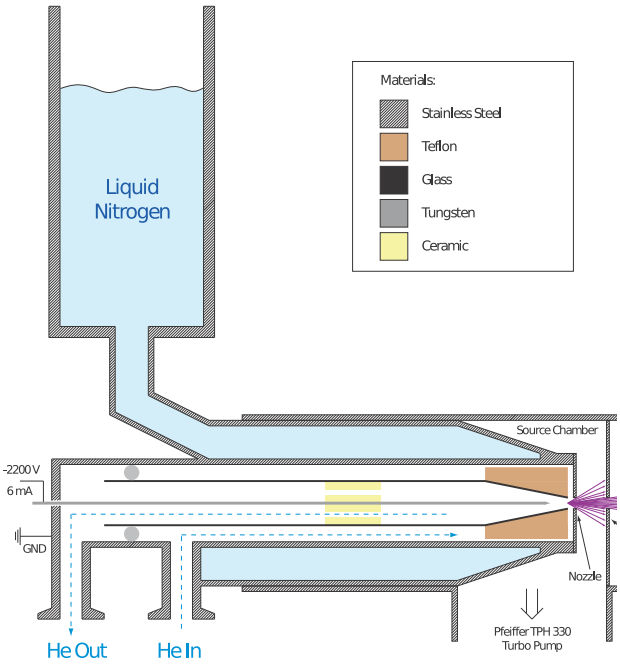

Figure 4.2: Helium flows into the source and is cooled through collisions with the liquid nitrogen cooled metal walls and is pumped back out through the glass tube. The tungsten needle produces a discharge plasma at the nozzle, and the process of electron recombination with helium ions produces the He* beam. Taken from Fig. 3.2 in [28]

The gate valve connection to the interaction region can be closed, isolating the lithography chamber from the turbos and the rest of the vacuum system. Then the lithography chamber can be vented with dry nitrogen to bring it up to atmospheric pressure. This is necessary to allow access for insertion of lithography samples into the vacuum system without compromising the entire chamber with atmospheric pressure. The lithography chamber can then be pumped by two sorption pumps to a pressure of a few mTorr, with an optional cold trap able to be attached to the top of the lithography chamber to speed up the pumping rate. At this pressure, the gate valve can be opened and the turbo pumps can finish the process of returning the pressure to 10^{-7} Torr. This process allowed 2-4 lithography samples to be patterned by the He* beam in a single day, depending on the necessary exposure time.

4.1.1 He* Source

The He* are produced in a differentially-pumped liquid nitrogen cooled DC discharge source [34, 35]. The source region is separated from the rest of the vacuum system by a

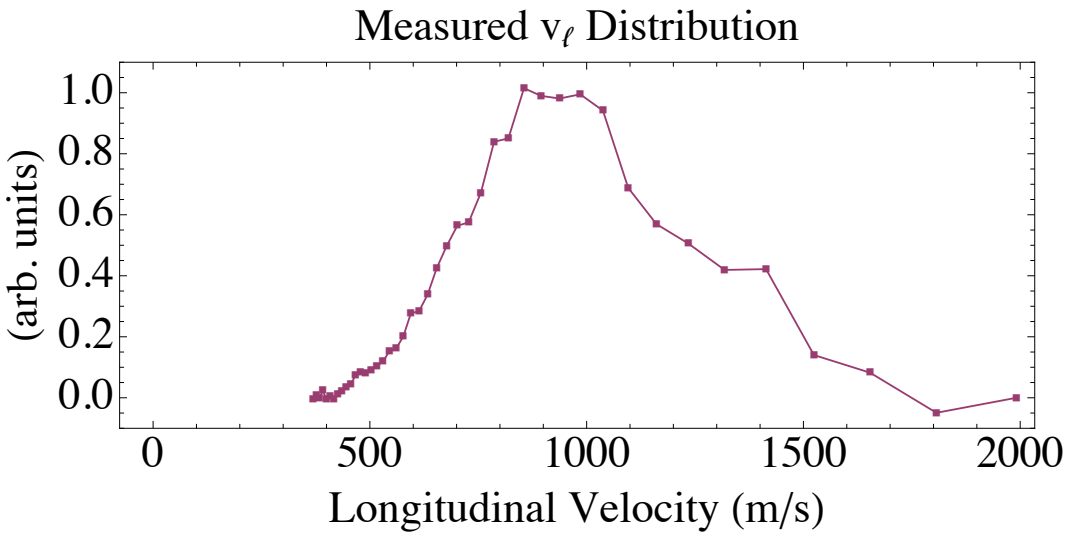

Figure 4.3: The longitudinal velocity distribution of the He* exiting the source measured with time of flight detection.

metal skimmer plate with a 0.5 mm diameter hole. The source has a glass tube tapered at the end as shown in Fig. 4.2. Helium flows into the vacuum chamber in the region between the outside of this glass tube and the liquid nitrogen cooled metallic jacket. The liquid nitrogen cools the helium gas as it collides with the walls. The helium is pumped out through the interior of the glass tube with a dedicated Welch 1376 mechanical pump. With the helium flow, the pressure in the source region typically rises one or two orders of magnitude. In the center of the glass tube is a tungsten needle whose sharpened tip is near the tapered region of the glass tube. A high voltage is applied to the needle through a load resistor (170 kΩ) and a discharge forms from electric arcing to the metallic nozzle immediately in front of the needle. In this region the helium atoms are ionized and a plasma forms. Exiting this region some helium ions recapture an electron from the plasma, and when the electron cascades down the energy levels of helium, there is a chance it will end in the metastable 2^3S state. A flux on the order $\sim 10^{14}$ He*/sr·s is produced. These atoms, along with singlet ground and excited state helium, ions, electrons, and UV light all exit the source through the 0.5 mm hole of the skimmer plate into the interaction region. The liquid nitrogen is used to reduce the average velocity of the He* beam. With the liquid nitrogen, the slightly supersonic He* beam in our system has an average velocity $\sim 10^3$ m/s. The longitudinal velocity distribution (Fig. 4.3) is measured by mechanically chopping an on-resonance laser beam and using time of flight to compare the arrival times of the pushed He* atoms to the laser pulse monitored with a photodiode.

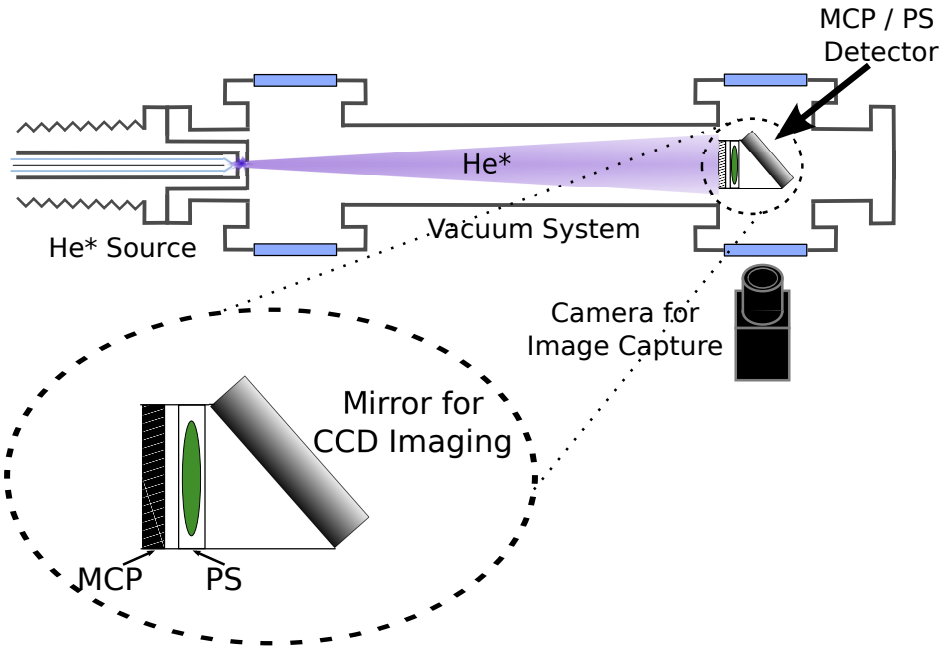

Figure 4.4: Each He* in the beam causes an electron to eject into the MCP. The MCP amplifies these electrons, and they are accelerated with a bias voltage to the PS. The PS produces light that provides an image of the He* beam profile that is reflected from a mirror and captured by a CCD camera outside the vacuum chamber.

4.1.2 He* Detectors

There are two types of detectors used for the He* beam. The first is a real time imaging detector made from a microchannel plate and a phosphor screen shown in Fig. 4.4. A microchannel plate (MCP) is composed of 10 μm channels at a 12 degree bias angle designed to amplify electrons in a process similar to a photomultiplier tube. The He* have a large internal energy (20 eV) and when colliding with the entrance of a channel on the MCP they eject electrons from the surface. Since each channel is small many can be placed equally spaced together so that the amplified electrons reflect the spatial distribution of the incoming He* beam. After the electrons leave the MCP a large bias voltage (1-2 kV) is used to accelerate them to the phosphor screen (PS), a glass plate coated with a phosphorescent material, which will emit light proportional to the number of electrons that collide. This produces an image that reflects the pattern that initially caused the electron injection on the front of the MCP. The PS is then imaged from outside the vacuum system using a CCD camera. This gives real time He* beam imaging in the transverse direction, however it can be difficult to measure the absolute intensity of the He* beam with this technique

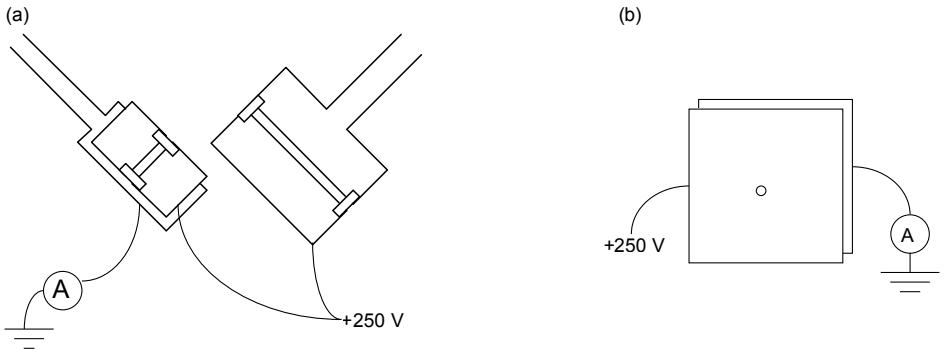

Figure 4.5: (a) The front SSD is mounted in two parts on different mechanical feedthroughs. When the two slits are overlapped the He* beam can be probed at a particular position by measuring the current from ground to the stainless steel plate attached behind the slit on the left. (b) The back SSD is two fixed metal plates with a 460 μm opening in the front. This detector is attached to the computer controlled stages measuring the current generated on the rear plate by He* that make it through the opening. Taken from Fig. 3.4(a) and Fig. 3.5(a) of [31].

because the PS would need to be continuously calibrated to compensate for the dimming that occurs as the screen ages. There are two MCP/PS detectors attached to the vacuum system identified as the 'front' and 'back' signifying their distance from the He* source. The two MCP detectors are nearly identical in design with the only significant difference being their location in the vacuum chamber. The front detector can image a larger divergence angle of the He* beam ($\sim$ 50 mrad) with less resolution, where the back detector has a range of ($\sim$ 20 mrad) with better resolution.

A stainless steel detector (SSD), the second type of detector, is very reliable for measuring the absolute flux in the He* beam, but is difficult to use for imaging. The SSD uses the same physical process as the MCP, a signal resulting from electron ejection, but instead of amplifying and imaging, the He* just collide with a flat metal surface, and then a moderate bias voltage ($\sim$ 250 V) is used to accelerate the electrons ejected from the cathode connected to ground. By measuring the small current (pA - nA) that flows to keep the cathode grounded, it is possible to measure the number of electrons being ejected each second. Correcting for the electron ejection efficiency (70% [36]) the He* flux is quantifiable. This can be used to slowly image the He* beam if an aperture is placed in front of the plate and then the apertured detector is scanned across the He* beam. There are also two SSD detectors within the vacuum system identified as front and back. The front SSD is attached to two mechanical feedthroughs near the gate valve. One feedthrough positions a single metal plate

held at 250 V with a 205 μm slit as shown in Fig. 4.5, and the other feedthrough positions two parallel plates. The front acts as a second slit (orthogonal to the first) with width 500 μm and biasing plate also held at 250 V. The last plate is a solid stainless steel plate that is connected to ground through a picoammeter to measure the current generated by the apertured He* beam ejecting electrons. The back SSD is directly mounted to the electronic stages in the lithography chamber used to scan the position of the detector. This detector is built from two parallel plates permanently attached together. The front plate has a 460 μm diameter hole at the center and is kept at 250 V, while the back plate is a solid piece of stainless steel grounded through the picoammeter. This detector is used to locate and measure the collimated He* beam intensity at the position of the lithography sample.

4.2 Infrared Laser System

The lowest energy excitation of He* is the $2^3\mathrm{S} \rightarrow 2^3\mathrm{P}$ transition at an optical wavelength near 1083 nm. This IR light is made with two external cavity distributed Bragg reflector diode lasers. Each laser produces a few 10's of mW at $\lambda = 1083$ nm and this light is sent through optical isolators and beam shaping lenses before each beam is coupled into a single mode optical fiber. These fibers can then be used to transport the light to any optical setup required. In practice one laser is dedicated to the bichromatic collimation for the He* beam, and the second laser is either used for other experiments or as an optical mask for lithography.

Each diode's frequency is actively stabilized using feedback on a piezo-mounted mirror that controls the external cavity length. The electronic feedback signal is derived from a saturated absorption spectroscopy measurement of an rf discharge cell of helium. In practice this method of locking resulted in a laser linewidth, measured by heterodyne spectroscopy, less than 250 kHz, which is below the natural width of the transition $\gamma = 2\pi \times 1.6$ MHz.

4.2.1 IR Bichromatic Light Production

The bichromatic force collimation required two beams of two frequencies each, for a total of four unique frequencies ($\omega_\ell = \omega_0 \pm \delta \pm k\mathrm{v}$), where each offset of kv is chosen to cause the force to collimate to v = 0 [37]. This is accomplished with a double-passed acousto-optic modulator (AOM) as shown in Fig. 4.6. The rf drive power and incoming laser angle of the AOM are chosen to give a 50% diffraction efficiency on each pass. The first pass produces two beams with frequencies ω_ℓ and $\omega_\ell + \delta$. The beams are retroreflected and sent back through

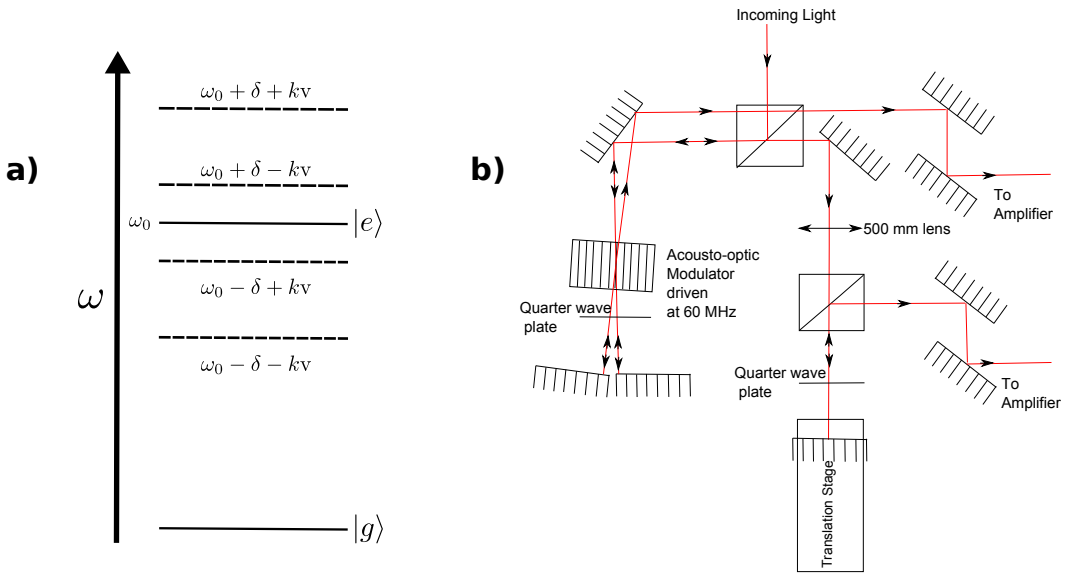

Figure 4.6: (a) Four frequencies are required for bichromatic collimation. (b) They are produced by double passing an AOM. The translation stage is required to set the correct phase between the two beams for the bichromatic force. Part (b) taken from Fig. 3.4 in [32].

the AOM to add an additional frequency to each beam leaving one beam with (ω_ℓ, $\omega_\ell + 2\delta$) and the other with ($\omega_\ell + \delta$, $\omega_\ell - \delta$).

The bichromatic beams are measured with a Fabry-Pérot interferometer (FP) to accurately balance the power equally between the two frequencies in each beam. After coupling the bichromatic beams into two optical fibers, the power in each beam is typically ~ 1 mW. The required intensity for the bichromatic force $I \approx 4000 I_s$ means that the optical power required is $\sim$ 1 W, so amplification is necessary. This is accomplished using a Keopsys KPS-BT2-YFA-NLS-1083-40-COL two stage 4 W Yb fiber amplifier. The first stage is a pre-amplification stage meant to saturate the input to the high power amplifier. The second amplification stage can be controlled by the level of pump power sent into the Yb doped fiber. The 1 W of required bichromatic power is typically achieved at 2-3 A of current into a single pump diode.

Following the amplification stage, a small amount of light is taken from the bichromatic beam containing $\omega_\ell \pm \delta$ and used for optical molasses cooling and the saturation absorption spectroscopy (SAS) frequency lock. The correct frequency offset for $k\mathrm{v} = \delta/2$ is accomplished by using a 90 MHz AOM to frequency shift this beam and lock to the SAS atomic resonance so that $\omega_\ell = \omega_0 - \delta/2$. This leaves the two bichromatic beams with frequencies given by $\omega_0 \pm \delta + k\mathrm{v}$ and $\omega_0 \pm \delta - k\mathrm{v}$ diagrammed in Fig. 4.6(a), where $\delta = 2\pi \times 60$ MHz and

$k\mathrm{v} = 2\pi \times 30$ MHz.

The optical molasses light is produced using additional AOMs to shift the $\omega_0 \pm \delta - k\mathrm{v}$ light closer to resonance. A high intensity molasses beam is shifted so that the frequency closest to resonance became $\omega_0 - 2\pi \times 8$ MHz. The second molasses stage is shifted with an AOM to $\omega_0 - 2\pi \times 1.6$ MHz. Since the light used to produce the molasses beams originated from one of the bichromatic beams, they both contained a second frequency. However this frequency is shifted further from resonance, and for the intensities used, had a negligible effect on the atoms.

4.2.2 IR Optical Mask Production

The IR optical mask is produced with the second 1083 nm diode laser. This laser is frequency locked using the SAS so that $\omega_\ell = \omega_0$. The laser light is fiber coupled and transported to near the lithography chamber of the vacuum system. The optical mask requires a detuning far from resonance to suppress radiative effects, so an AOM is used to frequency shift the light by 490 MHz above atomic resonance. The beam is then amplified using a single stage Optocom 30 dBm 1 W Yb fiber amplifier to variably set the optical mask power.

4.3 Ultraviolet Laser System

The next closest optically accessible He^* transition is the $2^3\mathrm{S} \rightarrow 3^3\mathrm{P}$ with a wavelength near 389 nm. High power at this wavelength is not as easily obtained as it is at the IR wavelength. Until recently diode lasers at this wavelength were nonexistent, and even now the diodes that do exist are very limited in power output, typically ~ 10 mW, far too low for our experiments. Our UV light is instead produced from a CW narrow linewidth Ti:Sapphire laser (Ti:Sapph) whose output is frequency doubled in a resonant cavity. The Ti:Sapph is at a wavelength of 778 nm and the frequency doubled light is at $\lambda = 389$ nm. The Ti:Sapph is pumped by a nominally 10 W, 532 nm wavelength laser, which was originally a Coherent Verdi V-10, but was replaced with a Lighthouse Photonics Sprout. The Verdi is a single longitudinal mode laser, but was no longer able to produce the full 10 W output due to aging in its internal diode pump lasers. The Sprout is a multi-longitudinal mode design, but this does not have any measurable effect on our Ti:Sapph laser output.

The Ti:Sapph output is sent to a second cavity in a commercial frequency doubling setup (Coherent MBD-200). This cavity contains a nonlinear LBO crystal which is able

to frequency double the Ti:Sapph light to the UV, which then exits through a dichroic mirror. The efficiency of the process is low, and scales with the electric field intensity squared (because it is a second order effect). The resonant cavity is used to build up intensity to improve the conversion. To build up high intensity, the cavity resonance frequency needs to match the incoming laser frequency. The cavity is designed with a piezo-mounted mirror to allow feedback to the cavity length to meet this condition. The feedback is from a Hänsch-Coulliaud signal [38], derived from the polarization dependence of the cavity (due to the nonlinear phase matching condition). This cavity lock is entirely built into the commercial system and only needs to be switched on, and as long as the incoming light stays single frequency, it will stay locked indefinitely.

With this laser setup, the typical Ti:Sapph output power is ~ 1.8 W at a wavelength of 777.951 nm, and the power produced at $\lambda = 388.98$ nm is typically 300 mW, although it can reach as high as 500 mW when pumped with a little over 2.0 W output from the Ti:Sapph. The UV light is produced in a room adjacent to the room housing the experimental vacuum chamber and thus requires transport. This was originally done with a free space beam through a hole cut in the wall between the rooms to preserve as much power as possible, but its stability was too sensitive to air currents and vibrations of mirrors over the long beam path. So instead a single mode polarization maintaining fiber is used for transport. Up to 40% of the available UV light exits from the fiber output, which is near the maximum expected based on the input coupling loss (-1.5 dB) and attenuation across 20 m of fiber (-0.6 dB).

The frequency of the Ti:Sapph is monitored with a interferometer-based wavelength meter (Burleigh Wavemeter WA-1500) with a resolution of a few hundred MHz. The experiments require that the laser frequency match the transition frequency to within the natural linewidth ($\gamma = 2\pi \times 1.5$ MHz). The Ti:Sapph cavity length, and accordingly its frequency, can be adjusted by a piezo that one of the mirrors is mounted on. Using this feedback, the laser is frequency-locked to a stable FP cavity made of InVar using a Pound-Drever-Hall (PDH) locking scheme [40]. The PDH error signal is produced from the reflected signal from a laser beam after passing an electro-optic modulator (EOM) producing sidebands at ± 65 MHz. This provides fast time scale frequency stability to the Ti:Sapph, but it needs to be referenced to an atomic absorption signal. The FP cavity length is also adjustable with a piezo mounted mirror. This cavity is scanned (causing the Ti:Sapph frequency to scan) and the frequency doubled light (also scanning) is used in a SAS measurement on a rf discharge helium cell. When the signal from the atomic absorption is found, the scan is halted and the SAS is used to feedback to the FP cavity length, keeping the UV light at the atomic

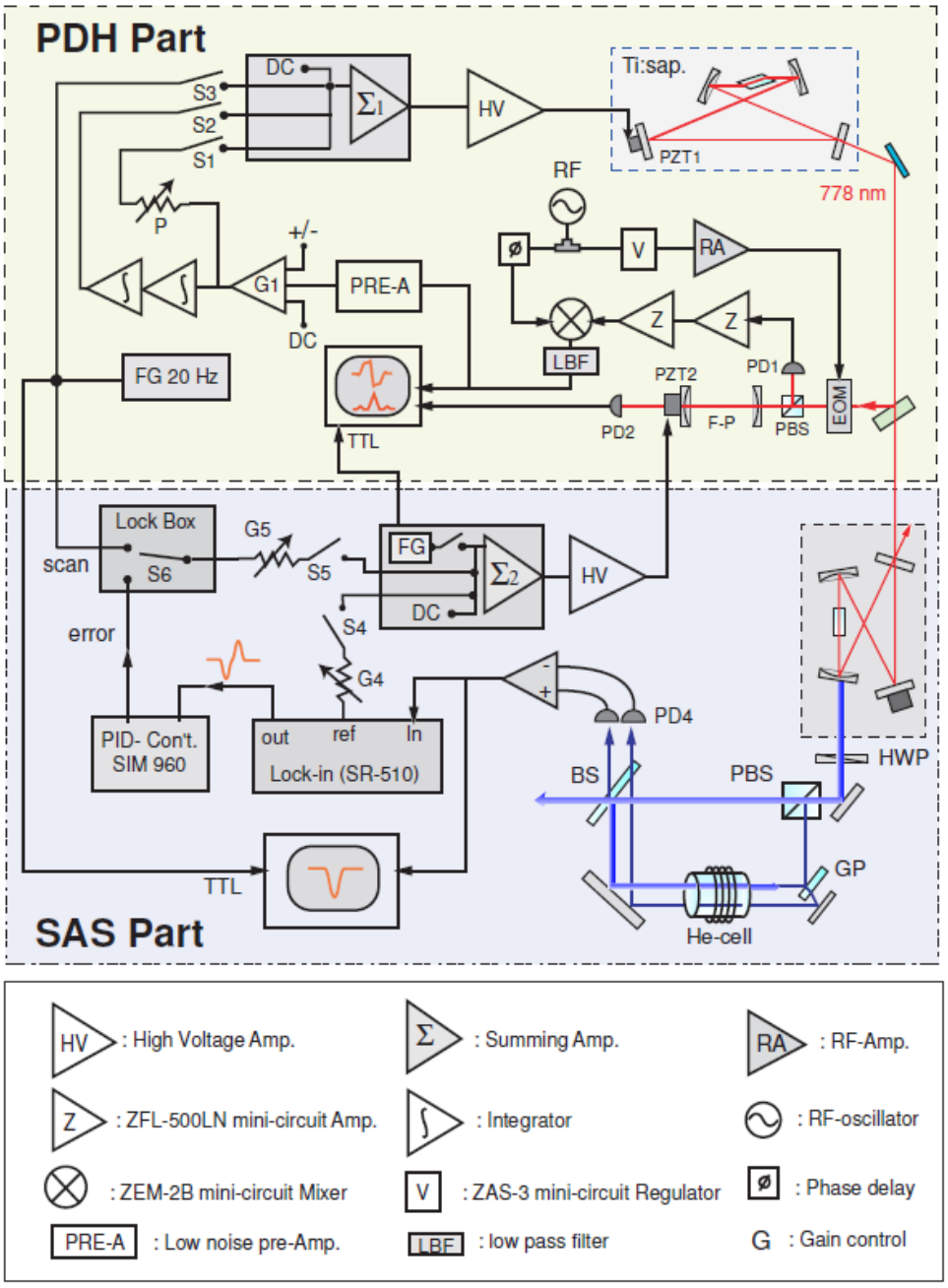

Figure 4.7: The electronic control setup for the UV frequency stabilization and lock. The Pound-Drever-Hall lock is used to stabilize the Ti:Sapph to an external stable cavity to provide fast time scale feedback. The external cavity length is controlled with a SAS feedback to maintain the frequency doubled light on the absorption signal of He^*, this provides long time scale stability. Taken from Fig. 3.10 in [39].

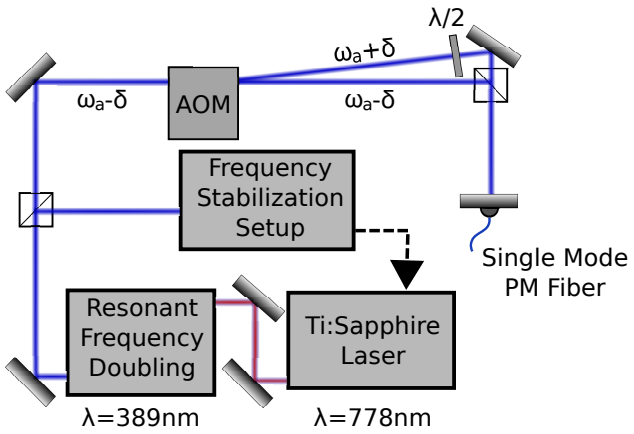

Figure 4.8: The UV bichromatic light is produced with a single pass of an AOM. The two beams are made to have orthogonal polarizations so they can be recombined with a polarizing beam splitter cube and coupled into a single mode polarization maintaining optical fiber.

resonance frequency. A schematic of these control electronics is shown in Fig. 4.7

4.3.1 UV Optical Mask Production

The UV optical mask is frequency locked by taking a small amount of UV light directly after the frequency doubling cavity and using it to lock directly to the atomic resonance. The remainder of the light is fiber coupled and sent to the vacuum system. At the vacuum system it is frequency shifted by $2\pi \times 80$ MHz using an AOM and sent to the lithography setup.

4.3.2 UV Bichromatic Light Production

As shown in Fig. 4.8, the bichromatic UV beam is produced directly following the frequency doubling setup. The UV light is sent through an AOM with 50% efficiency to produce two beams with frequencies ω_ℓ and $\omega_\ell + 2\delta$. One of the beams is sent through a half wave plate to rotate its polarization orthogonal to the first and they are recombined using a polarizing beam splitter (PBS). After the PBS the single bichromatic beam is sent into a single mode polarization maintaining optical fiber and transported to the room with the vacuum chamber.

The bichromatic force requires that the two frequencies be detuned equally from atomic resonance. The small amount of SAS light used for the UV frequency lock is first sent through an AOM so that the pump beam is frequency detuned 2δ above the probe beam.

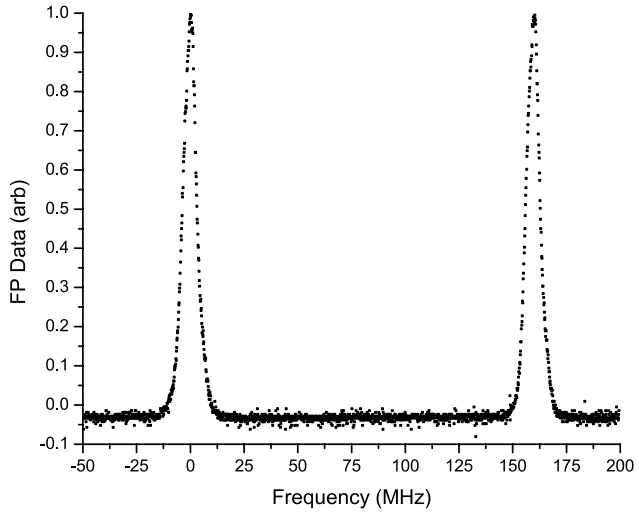

Figure 4.9: The transmission signal from the UV FP cavity built to measure the frequency intensity matching for the bichromatic force. The FP cavity length is scanned as two UV frequencies separated by 160 MHz were sent into the cavity. A Lorentzian fit of the FWHM gives a resolution of 6 MHz.

Then the SAS signal will occur for a value of $\omega_\ell = \omega_0 + \delta$. The SAS AOM is driven with the same rf signal as the bichromatic AOM so that in the end the two bichromatic frequencies are $\omega_\ell = \omega_0 \pm \delta$, where typically $2\delta \sim 2\pi \times 50$ MHz.

The bichromatic UV beams require a method to measure the relative intensity of each frequency component. A confocal FP cavity for UV was constructed to do this. Two mirrors with f=7.5 cm are mounted on 15 cm of InVar cut into a hollow cylinder. One of the mirrors is mounted on a piezo that can be used to sweep the cavity length. The cavity has a free spectral range of 500 MHz and a resolution (FWHM) of 6 MHz, shown in Fig. 4.9.

Chapter 5

Neutral Atom Lithography

The first demonstration of nano-fabrication using optical fields to steer neutral atoms was described by Timp and colleagues with a beam of sodium atoms deposited on a glass substrate [41]. Because of the chemical instability of sodium in air, their fabricated structure could not survive removal from the vacuum chamber. Later the direct deposition of more stable atoms was explored, with extensive demonstrations in chromium [27, 42, 43]. The structures fabricated with such direct deposition techniques are limited to atoms with readily accessible optical transitions for interaction with laser fields.

By contrast, lithography techniques can be used to make nano-scale patterns with a greater diversity of materials. This is because the patterning is done by optically controlling atoms that are different from the eventual fabricated material. The only requirement on these materials is their vulnerability or resistance to an appropriate chemical etch. Thus very many materials can be patterned for fabrication. A review of both direct deposit and lithography techniques appeared in 2003 [44]. The results of this chapter are also largely documented in [31, 32, 45].

5.1 Lithography Technique

Our neutral atom lithography (NAL), positive resist, is achieved by destroying the chemical bonds in a layer of polymeric molecules of self-assembled monolayers (SAM's), dissolving the damaged molecules, and finally etching the exposed area. The metastable 2^3S state of helium (He*) is ideal because its internal energy of 20 eV is higher than any other metastable atom. Thus it is most effective for exposing a resist with minimum dosage and results in the shortest exposure time, requiring minimum restrictions on the atomic beams and laser

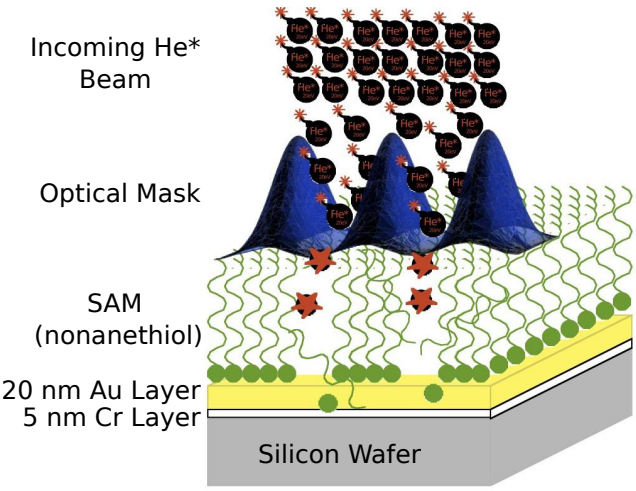

Figure 5.1: Our samples are silicon wafers with a 5 nm chromium adhesion layer for the 20 nm of gold. The SAM is formed with nonanethiol molecules on the gold surface and protects the surface when submerged in a chemical etch solution. The incoming He* beam traveling downward in this view is patterned (here with a standing wave optical mask) and transfers its pattern into damage on the SAM. When submerged in the etch solution, the damaged pattern will be etched into the gold.

control [44].

Our samples (Fig. 5.1) are built on single-crystal silicon wafers that have a 20 nm layer of gold evaporated onto their [100] surface over a 5 nm chromium adhesion layer. These wafers are grown and coated commercially. The SAM is formed on the gold surface by submerging the wafer in a 1 mM solution of nonanethiol in ethanol for 13 to 20 hours. The long chain molecules orient themselves with their hydrophilic heads bound to the gold substrate and their hydrophobic tails sticking out into the solution. The incident He* attacks the structure of the SAM molecules thereby making them soluble in a wet chemical etch. Then the unprotected gold regions are dissolved in a subsequent etch while the undisturbed SAM protects the remaining pattern in the gold layer.

5.2 He* Beam Collimation

Our NAL experiments use a bright beam of He* that originates from the reverse flow DC discharge source described in Sec. 4.1.1. The He* beam exits the source with a large divergence so that the intensity of He* quickly drops with distance from the source. To address this, the atomic beam is collimated with the bichromatic force [22, 37], followed by

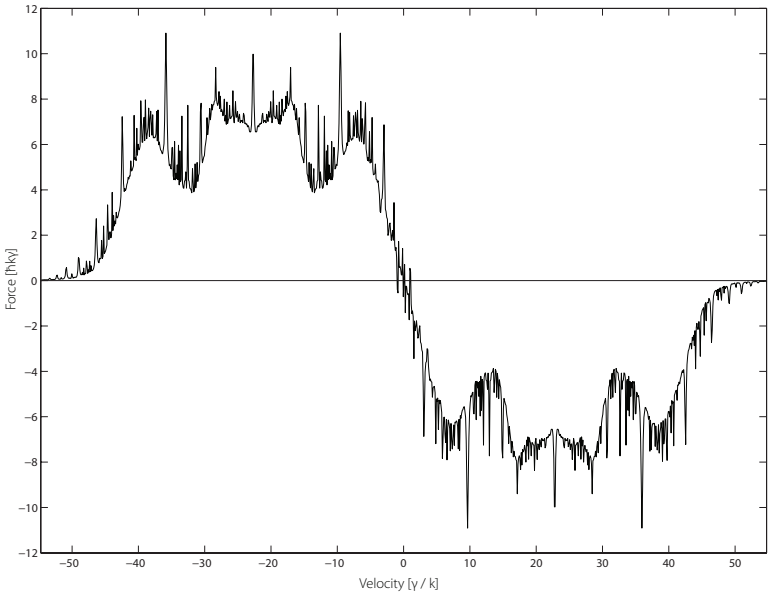

Figure 5.2: The two bichromatic interaction regions for each dimension are given a frequency offset to shift the force profile to vanish for v = 0. Taken from Fig. 2.10 in [28].

three optical molasses velocity compression stages. Because bichromatic collimation makes such an intense He* beam, our sample exposure time is measured in minutes instead of hours.

In our experiment, the bichromatic force is implemented with counterpropagating light beams, each containing two frequencies that are detuned by $\pm\delta = 2\pi\times 60$ MHz, and amplified with Yb fiber amplifiers as described in Sec. 4.2. With the frequencies of these beams centered about the atomic resonance, the dependence of the force on atomic velocity (v) is symmetric about v = 0 over the velocity range $\pm\delta/2k$, and nearly vanishes elsewhere. Since collimation requires a force that is antisymmetric about v = 0, we shift the velocity dependence by $\delta/2k$ without changing its shape by shifting the laser frequencies appropriately, see Sec. 4.2.1. The resulting force is unidirectional so that collimation requires two regions (Fig. 5.2) for each of the two dimensions, making four bichromatic force regions (Fig. 5.3). The four sequential bichromatic force regions are placed as close as possible to the point where the cone of He* atoms emerges from the source so that the collimated beam has a minimum diameter. The apodized Gaussian laser beam profiles in each 10 mm long region carry an average intensity of $\sim 4000\ I_s$.

The transverse velocity spread after the bichromatic force regions (first panel of Fig. 5.4) is about ±10 m/s corresponding to $\sim \pm 9$ mrad, and is not suitable for our purposes based

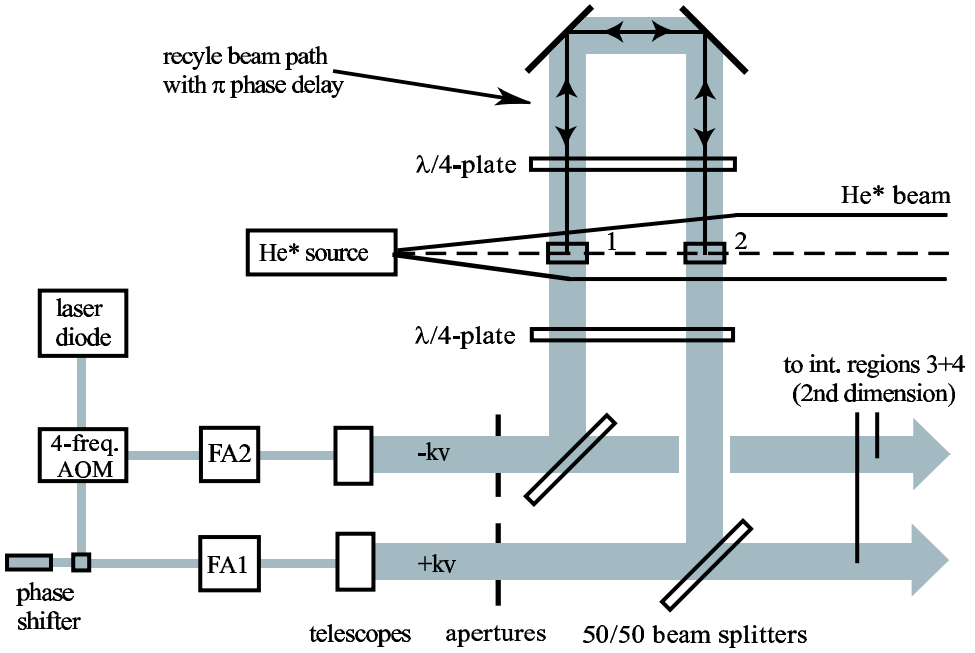

Figure 5.3: Each collimation dimension requires two bichromatic interaction regions because the force is unidirectional. Each interaction pushes atoms to v = 0 in the transverse direction. The two interaction regions are formed with the same bichromatic beams by matching the beam path length with the π pulse length of the bichromatic beat. The second dimension is also collimated with the same design (not shown). Taken from Fig. 3.5 in [32].

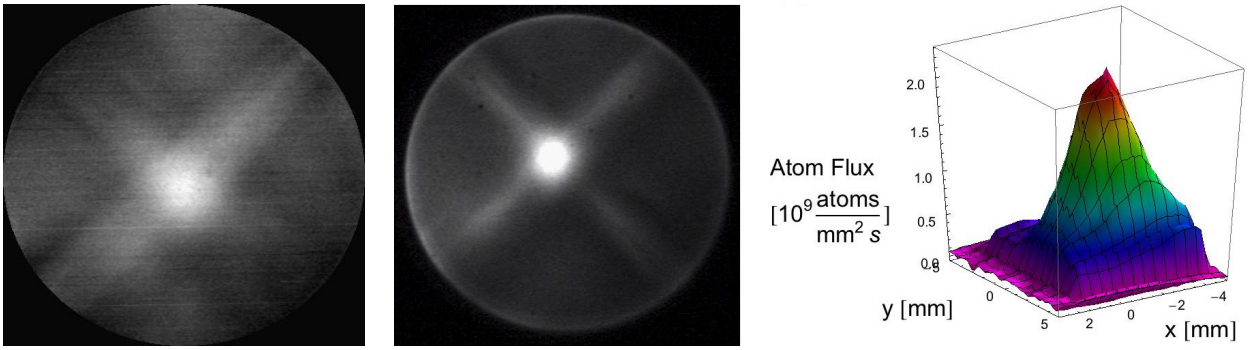

Figure 5.4: Measurements of the transverse profile of the He* beam with; (left) the front MCP/PS with bichromatic collimation only, (middle) the combined bichromatic and molasses collimation, and (right) the He* intensity measured at the sample position with the back SSD.

on the results of Sec. 3.1. Therefore we have a high intensity optical molasses stage with $\delta = -2\pi \times 8$ MHz and $s_0 = 10$ to capture atoms in this large angular spread, followed by an ordinary Doppler molasses to reduce the atomic beam divergence to nearly 3 mrad with very little loss of atoms, shown in the second panel of Fig. 5.4. These molasses regions have a length along the beamline of ≈ 19 mm and ≈ 9 mm respectively. A bit further down the line in the second set of interaction region windows is a one dimensional Doppler molasses used to steer the atoms and determine their angle of incidence at the target. This stage is more carefully monitored to set the finally velocity spread of the He* beam near the Doppler cooling limit for the lithography experiments, and results in a final transverse distribution of ~ 1 m/s. Also, to ensure that the He* beam is traveling perpendicular to the standing wave optical mask, this beam is made to be parallel with the optical mask beam to within 1 mrad.

This collimation section occupies 8.2 cm of our beamline and delivers $\sim 1.5 \times 10^9$ atoms/s-mm^2 at our sample, 68 cm from the He* source shown in the right panel of Fig. 5.4. Thus a 10 minute exposure deposits one He* in each ~ 1 nm^2 area without any focusing, and the focusing can easily increase this dosage to a few He* per SAM molecule site (estimated area ~ 0.3 nm^2). These dosages are known to $\pm$ 10% measured with the back SSD discussed in Sec. 4.1.2, and this precision arises from fluctuations of the laser beams that collimate the atoms.

5.3 Lithography Results

Our NAL is performed with three patterning techniques: mechanical mask, IR optical mask, and UV optical mask. In practice there is always a mechanical mask in the form of a metal grid placed before the sample that typically has a spacing of a few mm, and is used to determine the proper etching time. There is a smaller mesh of 10 μm size that can also be used to pattern the He* beam producing a small "box" pattern. The two optical masks are formed by sending a laser beam into the vacuum system and retroreflecting from a high reflectivity mirror attached perpendicular to the lithography sample. This mounting is needed to couple any movement of the sample to the mirror and therefore the standing wave pattern. The Gaussian beam is set so that the waist occurs at the mirror to give the maximum standing wave area. The sample is positioned so that the gold surface lies halfway through the optical beam.

The required He* exposure time for a lithography sample varies from day to day based on the effectiveness of the optical collimation. It is determined by mapping the collimated He* beam with the back SSD and adjusting the exposure time according to the value of the peak flux for that day. The exposure times range from 10 to 60 minutes. The sample etching is the least predictable part of the experiment. The best process is to visually monitor the sample surface while it is in the etching solution. When the pattern of the mechanical grid mask becomes visible, the sample is pulled from the etch solution and rinsed with distilled water. Then the samples are studied using a sequence of optical microscope, scanning electron microscope (SEM), and atomic force microscope (AFM).

5.3.1 Mechanical Mask Patterning

All our samples are exposed using a metal grid of mm scale as a mechanical mask. This grid pattern is shown in Fig. 5.5 and is always present, even when using a second smaller-scale patterning technique. This visible result is a useful visual test for the success of the He* exposure. A small mesh (15 μm spacing) is also used as a mechanical mask producing the pattern shown in Fig. 5.6 measured using an SEM and AFM. This patterning technique provides the initial estimate of the edge resolution, $\sim$ 80 nm. This resolution seems to be limited by the domain granularity of the gold layer and by the etching process (but not by the etching time). This method of neutral atom lithography is analogous to ordinary resist-based technologies that are used in most conventional lithography processes.

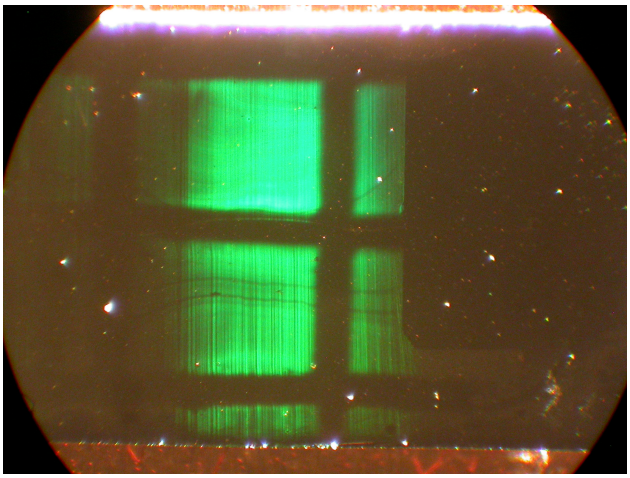

Figure 5.5: Optical microscope image of a gold lithography sample surface. The dark thick lines are the result of the mechanical mesh with spacing of 2 mm. The bright green color is optical diffraction of white light from the lines formed from an IR optical mask.

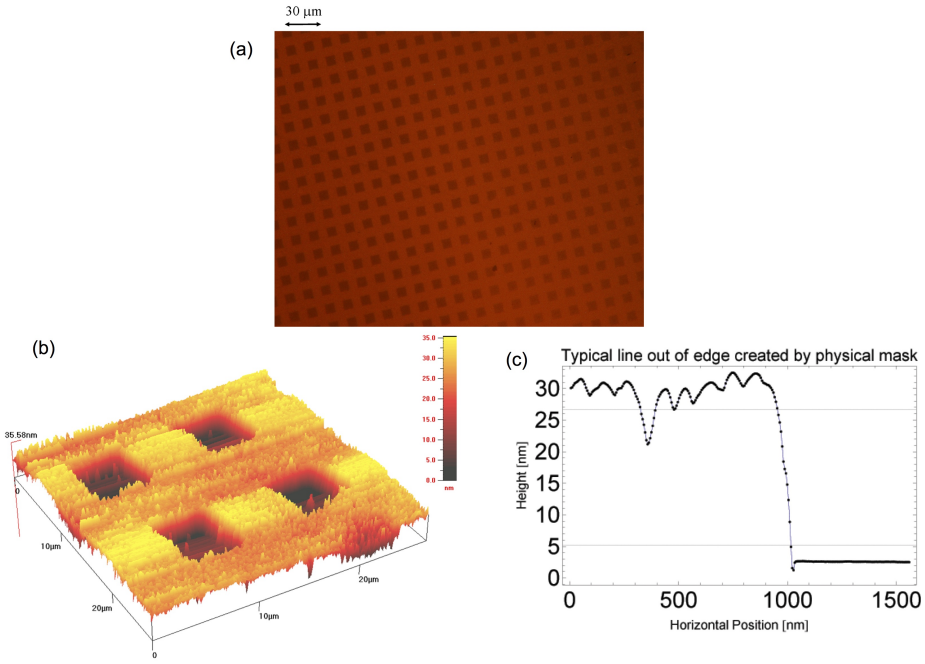

Figure 5.6: The result of patterning with a small mechanical mesh with boxes spaced 15 μm apart shown in an (a) SEM image of the gold surface, (b) AFM measurement of the surface height, and (c) lineout of the edge formed by the box measured with the AFM.

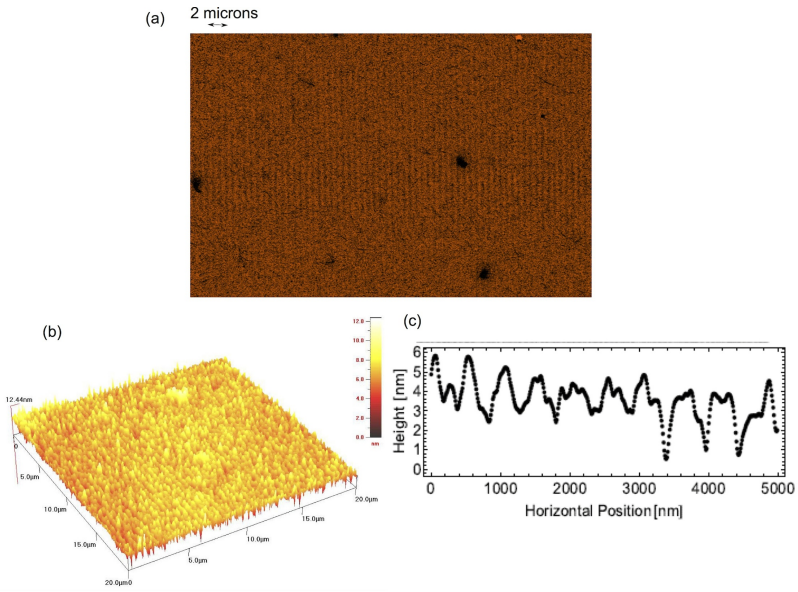

Figure 5.7: The patterning result for the IR optical mask with $P_{inc} = P_f$. The pattern is easily seen in the SEM image of the sample surface (a), but the AFM measurement shows that the pattern height is small and not very clean.

5.3.2 Infrared Optical Mask

Our IR optical mask is formed with a standing wave field of $\lambda = 1083$ nm light tuned ~ 490 MHz above the $2^3S_1 \rightarrow 2^3P_2$ transition (atoms attracted toward its nodes). It has an elliptical cross section with waist of $w_{\parallel} \sim 1.5$ mm parallel to the substrate surface and $w_\ell \sim 330\,\mu$m along the atomic beam path to maximize the patterned area. We describe the incident power of the traveling wave P_{inc} that is retro-reflected to form this "optical mask" in terms of the power that will focus the atoms on its resulting standing wave axis: P_f, see Sec. 3.1. The ellipticity of the optical mask slightly modifies the required power to $P_f' = P_f(w_{\parallel}/w_\ell) \approx 5.0$ mW.

The results of the numerical simulations described in Sec. 3.1 indicate that at P_f' the transverse velocity spread of the He* beam will cause the well-defined pattern of lines to wash out. The experimental result of patterning with this optical mask is shown in Fig. 5.7. The equally-spaced lines separated by 542 nm are poorly formed, as expected from the numerical results. Note that no previous experiment had been capable of showing pattern formation with He* in this regime. The poor quality of the patterning is the result of atoms that are not properly focused and damage the SAM in regions that should be protected. However the increased density of atoms that are focused still appears. The SAM is more

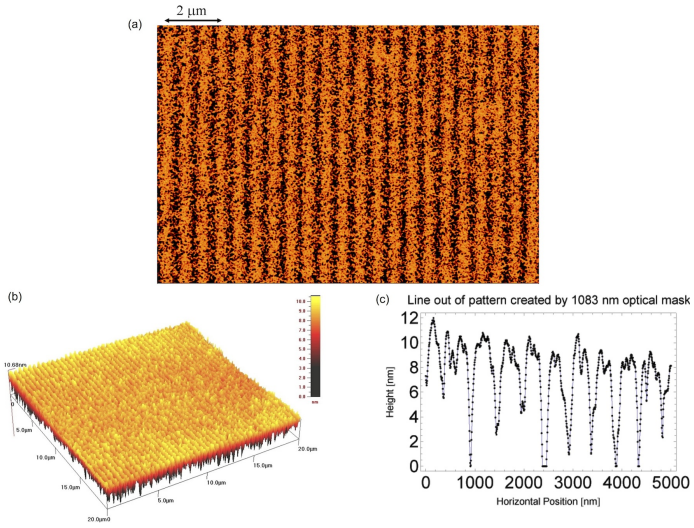

Figure 5.8: The patterning result for the IR optical mask with $P_{inc} = 3P_f$. With the higher optical mask power, the pattern is much more clearly formed as seen from the (a) SEM image of sample surface. The AFM measurement (b) and lineout across the pattern (c) show the etched channels have a width of $\sim$ 100 nm, consistent with the edge resolution from the mechanical mask results.

uniformly damaged in areas of the focus causing the resulting etch to more effectively remove the gold than in the areas between the lines with sporadically damaged SAMs.

The localization of the He* beam into lines is improved by increasing the optical mask power to $3P_f'$, Fig. 5.8. The results of the numerical simulation indicate with this power and velocity spread the lines should be well localized with fewer atoms landing in regions between each line. The pattern formed after etching the gold sample has deeper trenches that are spaced with spectroscopic regularity across the surface. The 20×20 μm region shown in the AFM surface scan Fig. 5.8(b) is less than 1/10000 the total patterned area. The length of each gold nano-line is $\sim$ 3 mm long, nearly 6000 times its width. This allowed the sample to act as a diffraction grating in the patterned area as seen in Fig. 5.5. The lithography resolution is estimated by the width of each channel to $\sim$ 100 nm although is somewhat limited by the granularity of the gold. This resolution is consistent with the $\sim$ 80 nm edge resolution obtained from the mechanical mask sample.

5.3.3 Ultraviolet Optical Mask

The UV optical mask used to pattern the He* beam is created using a CW Ti:Sapph laser that is frequency doubled using a resonant doubling cavity to $\lambda = 389$ nm, and locked to the

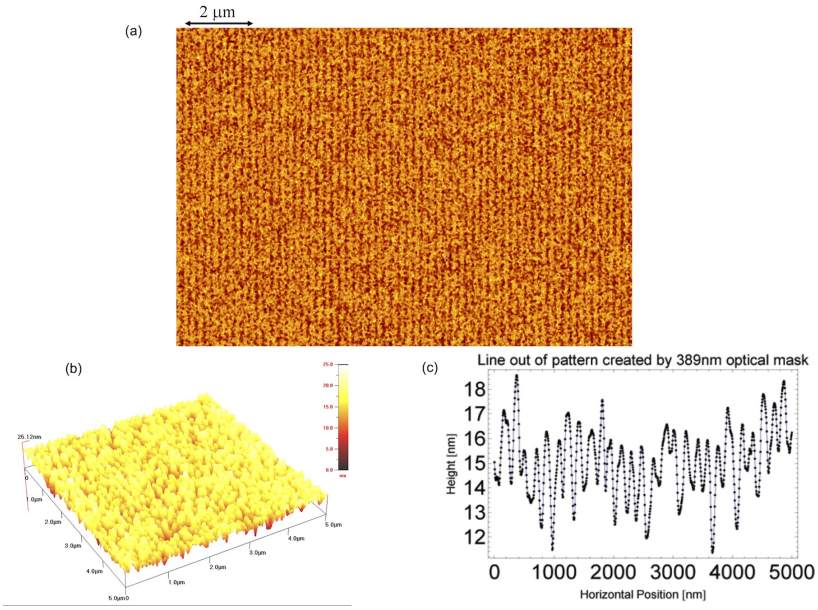

Figure 5.9: The UV optical mask produces lines separated by 194 nm, nearing the size of the gold surface granularity. (a) The optical mask pattern is clearly visible in the SEM image of the surface, but the AFM measurement (b),(c) shows the irregularity caused by the etching process of the gold grains.

atomic resonance frequency using SAS, as described in Sec. 4.3. To utilize the dipole force, the light is detuned by 80 MHz using an AOM. The optical mask beam is made elliptical to allow patterning over a large area ($w_1 = 1.12$ mm) while concentrating the intensity in the smaller dimension ($w_2 = 180$ μm). This reduces the probability of SE as the time spent traversing the optical beam is less than the radiative lifetime of the transition. The typical power used to pattern the atomic beam is P_{inc} =3-5P'_f, where for the UV parameters $P'_f = 3$ mW.

Fig. 5.9 shows an SEM image of an area on one of the gold samples that has been etched showing the pattern produced by the UV optical mask. The lines are now separated by 194 nm. The total area on the sample that has been patterned is $\sim$1 mm^2, so that the figure is 1/10000 the total area. To obtain information on the depth of the trenches, an AFM is used to produce the lineout shown in Fig. 5.9(c), showing trenches about equal in width as the structures. On the scale of our structures, $\sim$ 100 nm, the gold grain size has become a serious limitation in the pattern formation during the etch process.

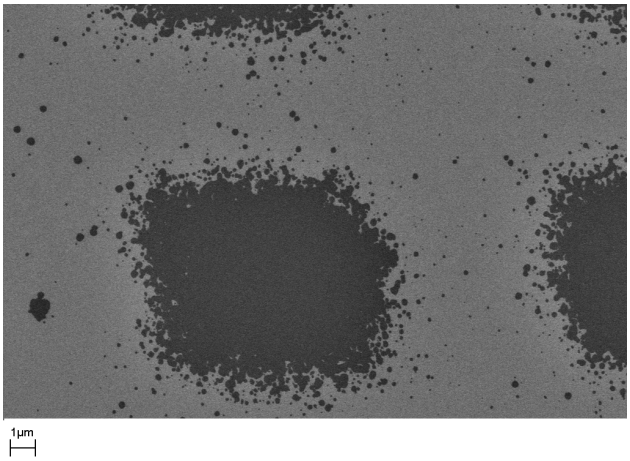

Figure 5.10: An SEM image of the palladium sample surface after NAL using a mechanical mask. The mask blocks all He* atoms outside the square pattern region, however the etch process is unable to reproduce the straight edges on a sub-μm scale.

5.3.4 Palladium Samples

The results using the UV optical mask reach a fundamental limit with the thin layer gold samples due to the grain size formed when the gold layer is deposited. These grains are intrinsically ∼50-100 nm in size as can be seen in Fig. 5.9. For this reason palladium patterning was attempted. Palladium grain sizes are smaller than those of gold allowing the possibility for smaller scale patterning. The thiol molecules used in the gold lithography process will form on palladium, however the selectivity of the etch arises from a different underlying process. The standard gold etching solution does not etch palladium, and based on results published on micro-contact printing lithography, a commercial etching solution was chosen [46]. It is believed that the method of monolayer protection to the surface is different from the gold. The thiol forms a much more tightly packed monolayer on palladium, and the resistance is not based on the hydrophobic nature of the thiol tail chain as with gold [47].

Fig. 5.10 shows the result of NAL on palladium with a mechanical mask. The pattern formed showed several interesting effects. First it is obvious that the palladium surface is much smoother than the gold surface. However the chemical etch does not seem to be isotropic, and etches out horizontally after breaking through the surface, as seen in the pitted structure. This made it impossible to produce straight edges on the length scale produced by the UV optical mask. This limitation and lack of better etch solution prevented further studies of the He* NAL process.

Chapter 6

Ultraviolet Bichromatic Force

The bichromatic force is a stimulated force whose magnitude (F_B) is determined by the properties of two overlapped standing wave fields at frequencies $\omega_{b,r} = \omega_0 \pm \delta$ and not by atomic parameters. The velocity range $\Delta \mathrm{v}_B$ is limited by non-adiabatic transitions between the dressed state energy levels of the combined atom plus two frequency light field [26]. These properties have no dependence on spontaneous emission (SE), which has no role in the force. The magnitude of the force is $F_B \sim 2\hbar k\delta/\pi$, as found by using the bichromatic dressed states, with proper choice of Rabi frequency Ω and of standing wave phase Δkz, see Sec. 2.3.2. The velocity range extends symmetrically about zero in a region of $\pm\Delta \mathrm{v}_B$, where previous studies have found $\delta/4k \leq \Delta \mathrm{v}_B \leq \delta/2k$ so both F_B and $\Delta \mathrm{v}_B$ scale with the value of laser detunings δ.

The process of laser cooling requires that a force have a velocity dependence, and that this velocity dependence allows atoms to accumulate at a particular location in velocity-space. This will occur if the interaction is able to extract energy and entropy from the atomic gas. The bichromatic force can meet all these requirements, and unlike other laser cooling techniques, without the aid of SE. The velocity dependence of the force has already been shown in many experimental and numerical studies for relatively long interaction times that inevitably included many SE events [22, 26, 37, 48–53]. The energy extraction is clearly possible through the exchange of the different frequency photons in the fields. Absorbing a 'red' photon and stimulating emission into the 'blue' photon standing wave will clearly leave the atom with less kinetic energy.

The last requirement is being able to extract the associated entropy from the atomic velocity distribution. In single frequency laser cooling this is not possible without the aid of SE. The large angular distribution of modes in SE allows many new states to become

accessible to the system of atoms plus light. The scattering of photons into these system modes acts as a huge reservoir for the entropy, $S = k_B \ln(N)$, where N is the number of states accessible to the system. It is so large that it is often (mistakenly) assumed to be necessary for the removal of entropy. However, with more than a single light field, it is possible to transfer the entropy into the applied laser fields through stimulated emission. It is the addition of multiple laser fields and the redistribution of photons among these fields that allows the BF to cool [54].

If we consider a dilute gas of atoms with an initial distribution of velocities spread over the range of $\pm\Delta \mathrm{v}_B$, application of the bichromatic force will accelerate all atoms with approximately the same magnitude F_B/M in a particular direction. As atoms approach the velocity limit of $\Delta \mathrm{v}_B$ the magnitude of the force quickly diminishes as a result of Landau-Zener (LZ) transitions between dressed states, so that there would be no appreciable change in velocity [26]. All atoms will reach this velocity region within a characteristic "cooling time" (t_c) estimated as

$$t_c = \frac{\Delta p}{F_B} = \frac{M\, 3\delta/4k}{2\hbar k\delta/\pi} = \frac{3\pi}{16\omega_r} \tag{6.1}$$

where Δp is given by twice the average value of $\Delta \mathrm{v}_B$.

The final velocity distribution will be peaked at $\Delta \mathrm{v}_B$, narrower than the initial distribution spread over the entire velocity range of the force. The fact that all the atoms are accelerated to $\Delta \mathrm{v}_B \neq 0$ has no bearing on their temperature. The location in velocity of the peak of the distribution is unimportant since it is always possible to transform into a frame moving at $\Delta \mathrm{v}_B$. The temperature is instead related to the distribution of velocities in the gas around this point. If the final distribution of velocities is narrower than the initial, then the atomic gas has been cooled. Additionally, as long as there has been no appreciable increase in the spatial distribution, we can say that the phase-space density has been increased.

6.1 Experimental Setup

Of course, in any experiment, the possibility of SE will always be present. To experimentally test the cooling process without SE, we have a chosen a transition with a large ω_r and long excited state lifetime τ to minimize the effects of SE. The $2^3\mathrm{S} \rightarrow 3^3\mathrm{P}$ transition in He at $\lambda = 389$ nm has a recoil frequency of $\omega_r = 2\pi \times 329$ kHz, giving an expected bichromatic cooling time of $t_c = 285$ ns. The excited state lifetime is $\tau = 106$ ns, so that the average SE time is at least 260 ns (the time average excited state population is 41% [53]).

The experiment was performed on a beam of He atoms initially excited to the $2^3\mathrm{S}$ state

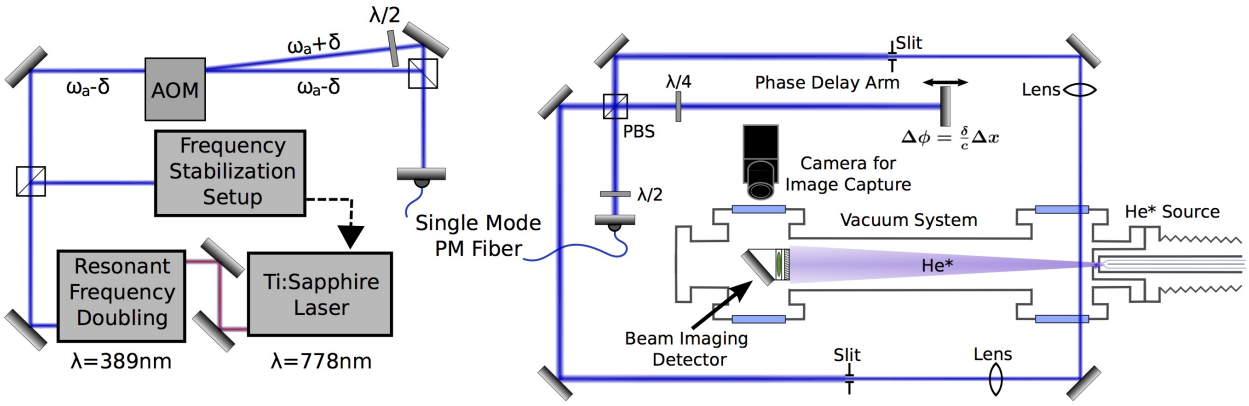

Figure 6.1: The experimental setup for the bichromatic force experiments is split between two laboratories. The laser system (left) uses an AOM and PBS to produce a UV bichromatic beam (see Fig. 4.8). This beam is transported through optical fiber to the He* beam apparatus, where it is split into two beams, each apertured with a slit and imaged from opposite directions to form the required standing wave.

through a continuous flow DC discharge source cooled with liquid nitrogen as described in Sec. 4.1.1. The optical standing waves are formed from a CW narrow linewidth Ti:Sapph laser at a wavelength of 778 nm that is sent to a resonant frequency doubling cavity to produce $\lambda = 389$ nm as described in Sec. 4.3.2. The bichromatic optical setup is shown in Fig. 6.1. The single frequency beam after frequency doubling is sent through an AOM to produce two beams at $\omega_\ell = \omega_0 \pm \delta$ (fundamental and first order). The two beams are recombined with a polarizing beamsplitter (PBS) and sent into a UV polarization-maintaining single mode optical fiber for transport to the He* beam apparatus. After exiting the fiber the two frequencies (orthogonally polarized to each other), are sent through a second PBS oriented at 45 degrees to the linear polarizations in the beam (in a setup similar to [22]). This produces two beams, each with two frequencies sharing the same polarization, shown in Fig. 6.2. The same polarization is required for the induced dipoles of both frequencies to be quantized along the same quantization axis. Each of the now linearly polarized two frequency beams is sent through mechanical slits and imaged from opposite directions onto the He* atoms.

The lasers are linearly polarized along the same direction when imaged onto the He* atoms to excite $\Delta m_J = 0$ transitions in the atoms. The atomic beam is unpolarized and could not be optically pumped prior to the bichromatic interaction because of experimental space constraints, thus leaving atoms in all three degenerate ground state magnetic sublevels. The π polarization was chosen because then the three degenerate magnetic ground state levels

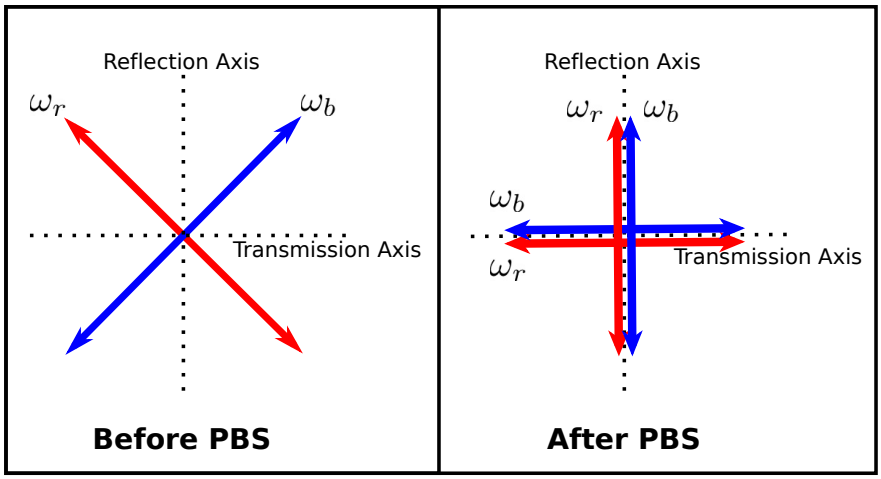

Figure 6.2: Exiting the optical fiber the two optical frequencies are orthogonally polarized, and rotated 45 degrees with respect to the reflection/transmission axes of a PBS. Each frequency is projected onto each axis with equal intensity, resulting in two separated beams (one reflected, one transmitted) that can be used to form the desired standing wave.

have Rabi frequencies in the ratio of $\sqrt{3} : 2 : \sqrt{3}$ for $2^3S_1 \rightarrow 3^3P_2$, see Fig. 1.6.

The experiments are typically run with $\delta = 2\pi \times 25$ MHz, where this is half of the AOM rf drive frequency. This means the optimum Rabi frequency for a spatial phase of $\Delta kz = \pi/2$ is $\Omega = \sqrt{3/2}\,\delta \sim 2\pi \times 31$ MHz. For our UV transition this corresponds to an intensity of $I = 2.6$ W/cm^2. This is a limiting factor in the experiment given the difficulty of producing high power bichromatic UV light. This detuning corresponds to a minimum velocity range of the force of $\pm\Delta v_B \approx \pm\delta/4k = \pm 2.4$ m/s. In principle these results should be the same at larger velocity ranges, just requiring proper scaling of the velocity with an increase in δ, but the required optical power scales as the square of the increase in δ, so that to double the velocity range would require over 5 W/cm^2. Given the imaged beam size, the incident power required from each direction on the atoms is ~ 10 mW. The bichromatic force has an intensity dependence so the slits are designed to capture the flat region on the top of the laser's Gaussian profile with only $\pm 10\%$ variation in the Rabi frequency across the interaction region. This results in transmitting only a fraction of the power delivered to each slit. The small size of the bichromatic beams after imaging the slits, and the variability of the output power from the UV setup make it difficult to accurately set the Rabi frequency for the bichromatic force on a daily basis.

Following the bichromatic interaction region, the He* beam (< 1 mm in size) freely expands, allowing a transverse TOF measurement of the velocity profile 630 mm downstream.

The large transverse expansion and the small initial size following the bichromatic interaction causes the transverse velocity (v_t) distribution to map directly to the transverse position distribution on the detector, where

$$v_t = \frac{L_t}{L_l} v_l \tag{6.2}$$

where L_t is the transverse displacement on the detector, $L_l = 630$ mm is the longitudinal distance, and $v_l = 1050$ m/s is the average longitudinal velocity. The He* are detected using an MCP/PS to directly image this transverse distribution (see Sec. 4.1.2). The transverse spatial spread of the He* beam after the 630 mm flight is very much larger than the detector's 24 mm size, so that absent any optical interaction the He* has a uniform distribution. Following the application of the bichromatic standing waves the velocity distribution measured by the detector changes, and this can be directly compared with the initial distribution. The sensitivity of the MCP/PS is not spatially uniform, and this effect is cancelled by dividing the two images with and without the bichromatic force to measure changes in the He* velocity-space density.

6.2 Bichromatic Force, Phase Dependence

The first experimental tests using the bichromatic standing wave setup shown in Fig. 6.1, were to observe the phase dependence of the force with about $1.2\,t_c$ of interaction time. Sec. 2.3 showed that the relative spatial phase between the red and blue standing waves controls the direction of the force. Experimentally the phase between the red and blue standing waves varies with the length of the delay arm shown in Fig. 6.1. A difference in path length (ΔL) between the two beam paths used to form the standing wave is related to the phase by $\Delta L/L_\pi = \Delta kz/\pi$, where $\Delta k = 2\,\delta/c$ as defined as in Eq. 2.25. At a path length difference of one bichromatic beat length, the standing waves return to the original phase. The length of the beat is $L_\pi = c\frac{\pi}{\delta} = 5$ m, for the $\delta = 2\pi \times 30$ MHz used for this data.

To look for the directionality dependence, the delay arm is varied over the length of L_π. Then looking at the direction of the atomic beam deflection we are able to identify the relative phase of the standing wave fields, Δkz. Fig. 6.3 shows results for several delay arm distances as a % of L_π, where $L_\pi/2$ corresponds to $\Delta kz = \pi/2$. The distributions in Fig. 6.3 show atoms missing (dip) and moved to a new position in velocity-space (peak). The data is shown as a percentage change in detector signal between the initial uniform He* distribution to that after the bichromatic force. The magnitude of this change is limited by a large background signal on the detector arising from VUV light emitted from the He* source

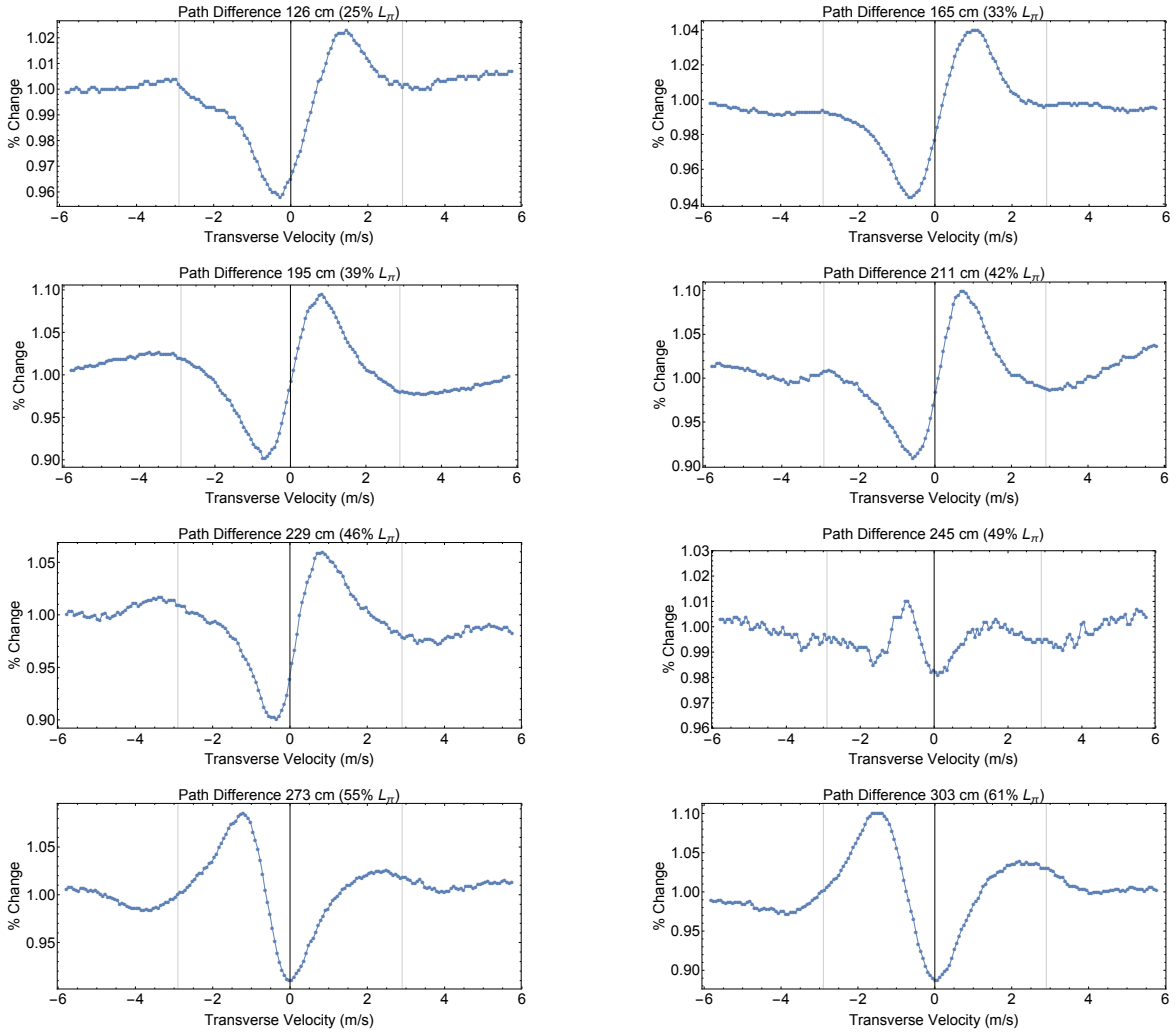

Figure 6.3: The optical path length difference between the two beams determines the relative phase between the two standing waves. The direction of the force is set by this phase; pushing to the right for $\Delta L < L_\pi/2$, pushing left for $\Delta L > L_\pi/2$, and with no preferred direction at $\Delta L = L_\pi/2$.

discharge. Independent measurements have shown this background to be $\sim 90\%$ of the MCP/PS response with gradual changes as the detector ages or the He* source parameters change. As the standing wave phase is varied, the directionality of the force changes from right to left and has vanishing directionality as it nears the center with $\Delta kz = \pi/2$. This type of response is a purely bichromatic force effect and verified that the UV bichromatic force was working.

The total span of the velocity range in these deflections is much smaller than expected, only ~ 1 m/s when $\delta/4k = 2.9$ m/s. It was determined that the small velocity range was the result of the available power in each laser beam (10 mW) being slightly below the optimal Rabi frequency for $\delta = 2\pi \times 30$ MHz. This results in a force around a narrow velocity range as is predicted in the force profile vs Rabi frequency in Fig. 3.5.

At this point the detuning was reduced to $\delta = 2\pi \times 25$ MHz and the phase delay arm was fixed at $\Delta kz = \pi/4$ for the remainder of the experiments, since changing the delay arm length was a non-trivial task, given the critical nature of matching the transverse profile of the two beam paths and the small beam sizes used in the two imaging systems.

6.3 Bichromatic Force, Ω Dependence

Since the power of the bichromatic UV light was at its maximum, the AOM frequency was lowered ($\delta = 2\pi \times 25$ MHz) to address the insufficient Rabi frequency in the beams. At the new value of δ, the required optical power should be 30% lower, and the magnitude of the minimum velocity range is also reduced to $\Delta \mathrm{v}_B \approx \delta/4k = 2.4$ m/s. Data is accumulated as the laser power delivered to the He* beam is varied, and used to produce a 3D density map of He* intensity as a function of detector position (transverse velocity) and Rabi frequency.

The spatial distribution of the atoms is measured over a range of Rabi frequencies in a single run by capturing a video ($60 - 100$ s) of the MCP/PS detector while continuously rotating a variable neutral density (ND) filter immediately following the fiber and simultaneously recording the intensity of one of the bichromatic beam's reflection off the front of an optic. The circular ND filter returns to maximum intensity after one full revolution, and this sudden jump from very low intensity to very high intensity is used to synchronize the MCP/PS video clock to the oscilloscope data obtained with a photodiode on the reflected beam.

After saving the video file, the data analysis is done with a combination of ImageJ and Mathematica. An ImageJ script (see Appendix C.1) is used for image processing (background removal, image rotation, cropping) and takes a vertical average over a rectangular section of

the detector screen for each frame. This reduces the data from the uncompressed video size of several GBs to a set of several thousand lineouts which was ~ 15 MB in total size. The Mathematica script (see Appendix C.2) then imports each frame's lineout of He^* intensity vs position along with the oscilloscope optical power data. The independently-measured maximum optical power for that day along with the relevant beam parameters are used to calibrate the photodiode data and convert it to Rabi frequency as a function of time. This time axis is correlated with the frame numbers of the video lineouts by identifying the frame during which the atomic spatial distribution has the largest change. This is guaranteed to be the time at which the laser intensity went from the minimum to maximum. Then because the number of frames at each value of Rabi frequency is not consistent across the video, the Rabi frequency is binned and lineouts within each binned value of Rabi frequency are averaged to reduce noise. The position axis of the lineout is calibrated to velocity using Eq. 6.2 and $\mathrm{v}_l = 1050$ m/s. The entire analysis process for each force map (using typical PC computing power) takes ~ 20 minutes. This results in a three dimensional data set called a force map of Rabi frequency vs velocity vs He^* intensity.

A typical bichromatic force map is shown in Fig. 6.4 where dark purple shading indicates a reduction in He^* intensity and lighter white shading is an increase in intensity. At low Rabi frequency the atomic velocity distribution remains relatively unaffected and uniform. When the bichromatic standing waves reach the optimal Rabi frequency a large dip appears in the atomic velocity distribution near $\mathrm{v} = -4$ m/s, and a large peak appears at positive velocities around +6 m/s. This large velocity limit is surprising given the short interaction time (220 ns $\approx 2\tau$) indicating the force is able to act very efficiently on these short time scales. The total velocity span is 10 m/s $\approx 40\mathrm{v}_r$ implying a net 20 cycles of absorption followed by stimulated emission. This final velocity distribution has an increased density of atoms in velocity-space around $\Delta\mathrm{v}_B \approx \delta/2k$. This is only possible because atoms from within the range of the force have been accelerated and accumulate at the limit while atoms already at and outside this velocity range are not affected by the force. The appearance of a large peak in the velocity-space density clearly demonstrates cooling. The He^* beam has a transverse spatial extent of $\sim 1000\lambda$, and over the course of the interaction region expands by

$$\Delta\mathrm{v}_B\, t_c = \left(\frac{3\delta}{8k}\right)\left(\frac{3\pi}{16\omega_r}\right) = \left(\frac{9\delta}{256\,\omega_r}\right)\lambda \tag{6.3}$$

where $\Delta\mathrm{v}_B\, t_c \approx 2.7\lambda$ for our choice of δ so there is negligible reduction in position-space density. This result has no measurable dependence on the interaction region's distance from the He^* source over about a cm, other than a drop in intensity on the MCP/PS detector

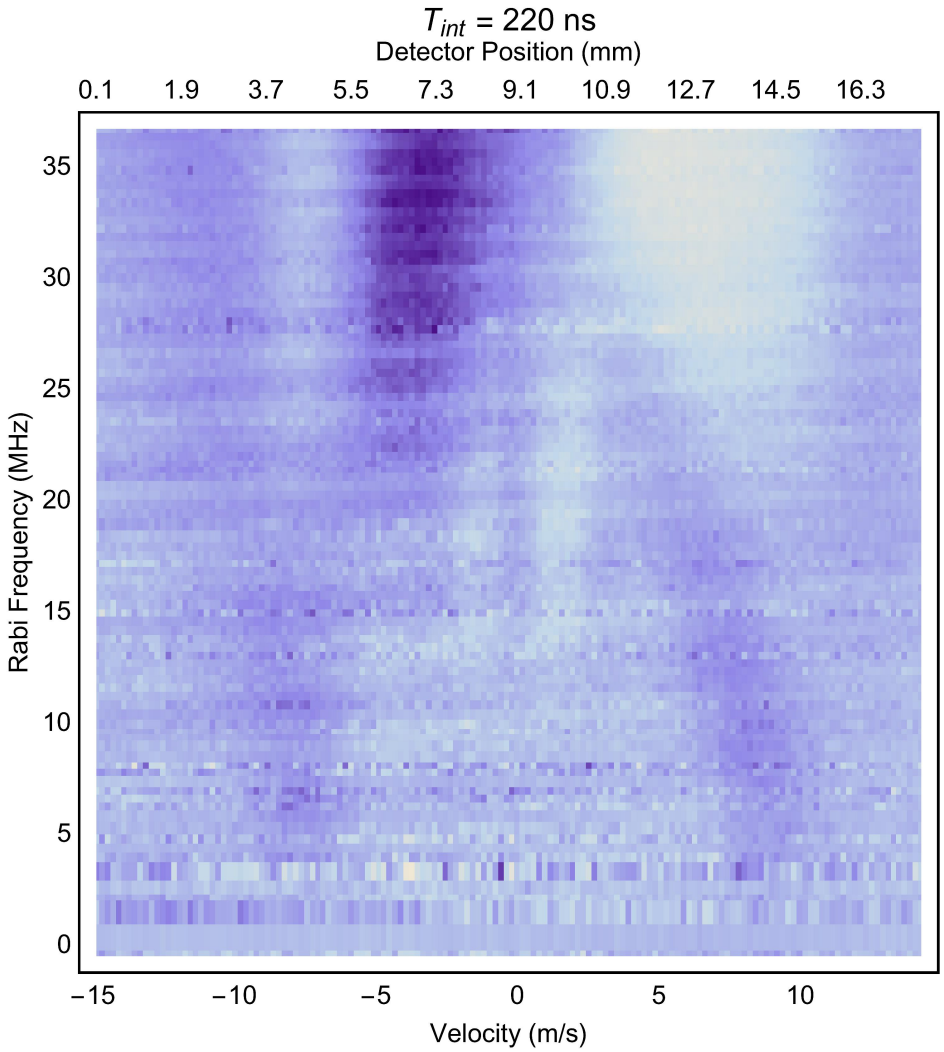

Figure 6.4: A force map of He* velocity-space density as a function of the bichromatic Rabi frequency. Darker purple shading indicates a reduction in He* intensity noticeable at higher Rabi frequency to the left of v = 0, and lighter white shading is an increase in intensity occurring to the right near $\Delta v_B \approx \delta/2k$. Each horizontal line of pixels is the MCP/PS detector signal averaged over 10s of image captures, where each image is averaged to a single dimension along the force axis.

caused by the He* beam expanding to a size larger than the vertical extent of the bichromatic standing wave beams.

The role of SE will depend on the interaction time of the atoms in the bichromatic standing wave. The mechanical slits are used to give well defined edges to the interaction region so that the total interaction time is given by $t_{int} = \frac{s}{\mathrm{v}_l}$ where s is the imaged slit opening. The bichromatic force is tested as a function of t_{int} by recording force maps for different slit openings, shown in Fig. 6.5. All interaction times (never long enough for many SE events) show a very similar spatial distribution. A large region of atoms at negative velocities have been removed and accumulate near positive velocities on the right. There is no noticeable dependence on interaction time until the slit opening becomes as small as 150 μm corresponding to $t_{int} \approx 140$ ns, at which the width of the velocity dip is reduced indicating insufficient time for the atoms within the entire velocity range to reach the limit.

The difference in coupling strengths for the three initial ground state m_J sublevels causes different atoms to experience different Rabi frequencies and hence different force profiles. It is not possible to simultaneously optimize the Rabi frequency for all three sublevels. A force map was taken for the $2^3\mathrm{S}_1 \rightarrow 3^3\mathrm{P}_1$ transition to see if this was a significant effect. For the π polarization used, the $m_\mathrm{J} = 0 \rightarrow m_\mathrm{J} = 0$ transition is forbidden, and this prevents roughly one third of the atoms from interacting with the light, thereby reducing the detector signal. However the remaining two states have identical coupling strengths. The resulting force map is shown in Fig. 6.6 along with the previous data from Fig. 6.4 shown as a reference. The results are qualitatively similar. This result is strong evidence that SE is not frequent enough to optically pump all the atoms into the $m_\mathrm{J} = 0$ dark state and no longer interact with the light. Since interaction time is determined by the slit geometry and doesn't depend on the transition used, this is proof that all of the force maps that demonstrate a strong peak in velocity-space density have done so without the aid of SE.

Estimating the final temperature of the atoms following the bichromatic laser cooling requires defining a measure of the spread in the final velocity distribution. This is complicated by several experimental 'smearing' effects in the measured force maps. The transverse velocity assignment (Eq. 6.2) is possible using the longitudinal velocity v_l, but the He* source produces a distribution of v_l values. Even if the cooling is perfect and results in a single transverse velocity, the beam would have an angular divergence traveling to the detector given by the range of $\mathrm{v}_t/\mathrm{v}_l$ values, where the v_l distribution varies over about 40%. Further, the actual spread of the final velocity distribution that will result from finite temperature will be convolved with this distribution of longitudinal velocities causing additional spreading of the detected signal. All these effects will lead to an overestimation of the actual width of

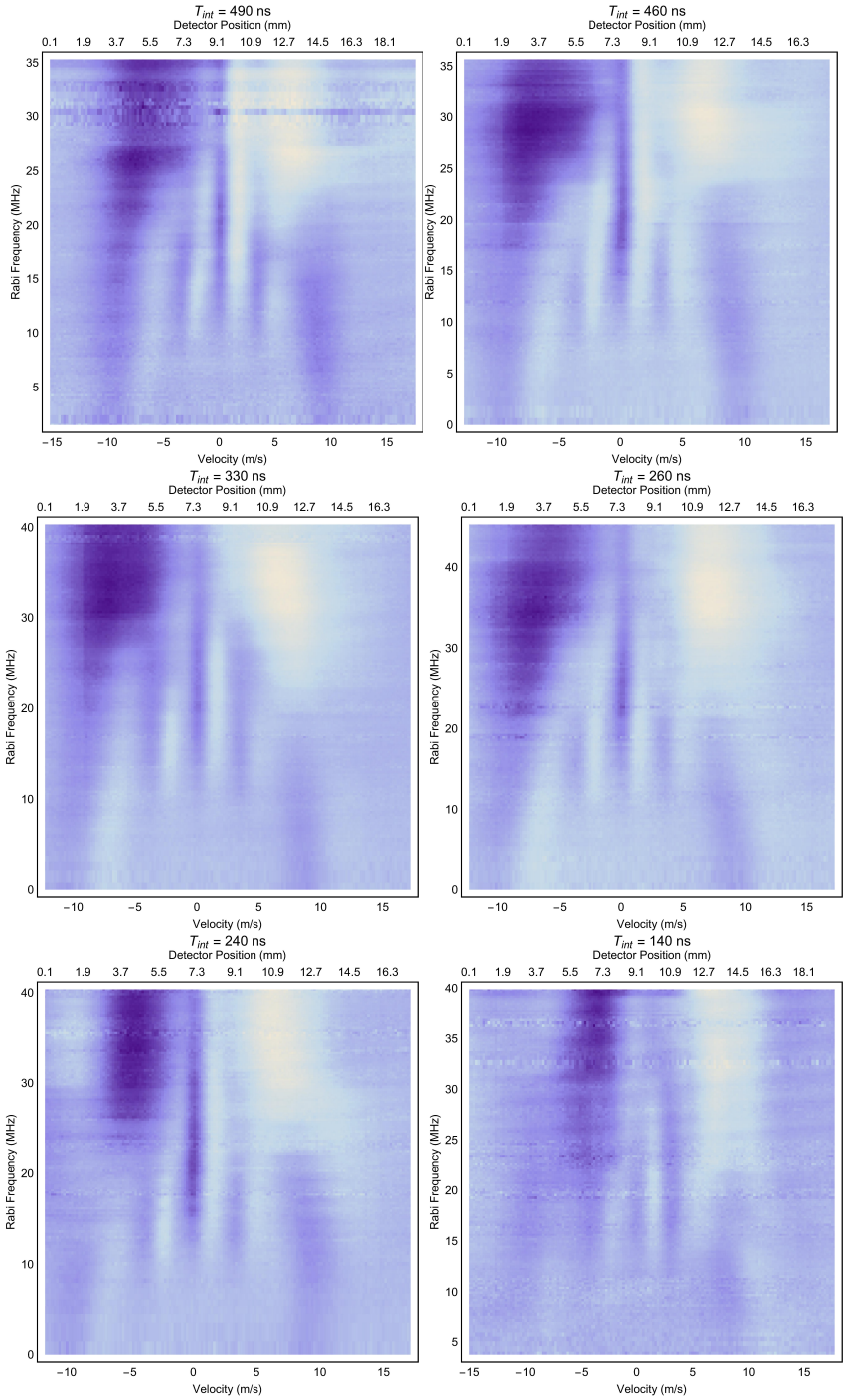

Figure 6.5: The He* velocity-space density as a function of Rabi frequency (vertical axis) for different imaged slit sizes, resulting in different bichromatic interaction times. The result is not strongly dependent on the interaction time over these time scales, with the only notable difference occurring as $t_{int} \to 140$ ns, where the width of the reduced/increased intensity is reduced.

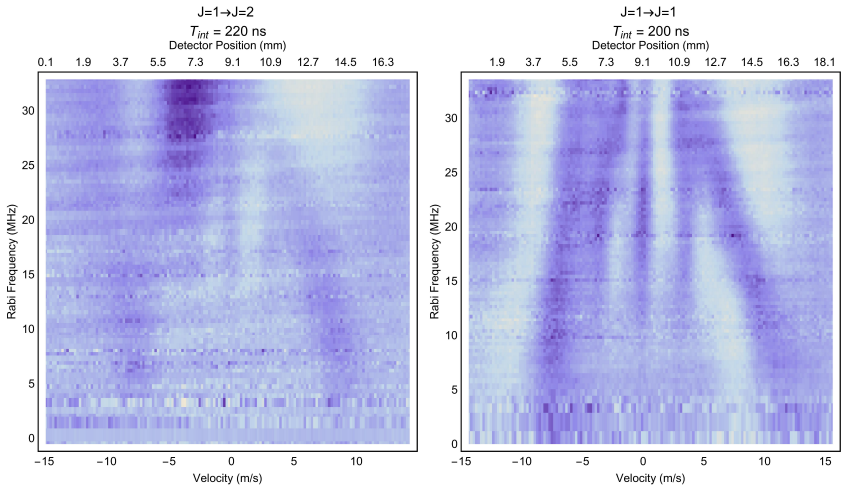

Figure 6.6: The He* velocity-space density as a function of Rabi frequency for the $J = 1 \rightarrow J = 1$ and $J = 1 \rightarrow J = 2$ transitions. The coupling strength for the $J = 1 \rightarrow J = 1$ transition is equal for two of the initial ground state sublevels, and zero for the third. This causes roughly one third of the atoms to not experience any optical interaction. The observation of the bichromatic force confirms that SE is not occurring, as this would quickly optically pump all atoms into the dark state.

the final transverse velocity distribution. Several experimental schemes were attempted to address these effects (described in the next section), but were largely unsuccessful.

A lineout of the force map from Fig. 6.4 taken at a Rabi frequency of 36 MHz is shown in Fig. 6.7. This Rabi frequency is different from the optimum $\sqrt{3/2}\,\delta$, but is likely an indication of the experimental difficulty in measuring the standing wave amplitude at the He* beam. The interaction time for this experimental data was 220 ns. The range of the bichromatic force extends between ± 6 m/s, and the He* atoms accumulate around $+6$ m/s. The final distribution has a full width half max of ≈ 4.8 m/s, corresponding to a final temperature of ≈ 10 mK. The temperature that corresponds to the full range of initial velocities affected by the bichromatic force (≈ 18 m/s) would be ≈ 40 mK, indicating the bichromatic cooling has reduced the one dimensional He* beam temperature by about a factor of four.

The cooling limit of the bichromatic force is not well understood theoretically. The velocity limit arises due to LZ transitions, and the probabilistic nature of these events indicates a statistical distribution of final velocities related to the number of jumps. The statistical nature would predict the force should require a few LZ jumps before sufficient cooling can occur. However the diffusion among dressed levels discussed in Sec. 2.3.3 could also lead to additional heating. The rate of this heating and how the bichromatic force responds is not

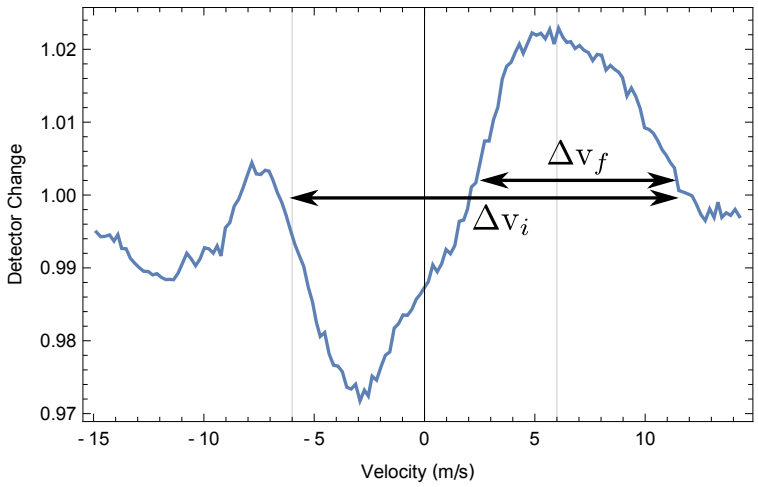

Figure 6.7: The final velocity distribution after a bichromatic force interaction time of 220 ns. The bichromatic force has accelerated atoms from the region labeled Δv_i to the peak centered at +6 m/s with a width Δv_f, corresponding to a final temperature of ≈ 10 mK.

something that has been investigated to date. The small magnitude of detuning and velocity range available for our experiments provides limited opportunities for the LZ transitions to occur. The typical transverse travel distance of an atom across the standing wave is given by Eq. 6.3. This means that the typical distance traveled for an atom in the experiments is about 2.7λ; offering ~ 10 avoided crossings for potential LZ transitions based on the dressed state model. It is not clear what effect this will have on the cooling limit. It is also possible that this could be the source of the increased velocity limit near $\Delta v_B \approx \delta/2k$. In the absence of the LZ jumps, the force will continue to accelerate the atoms, and as the velocity increases the LZ jumps may no longer be limited to the usual regions of avoided crossings.

6.4 Attempted Detection Schemes

Initial data was taken with the front MCP/PS until it was determined that the limited laser power would necessitate fairly low values of δ resulting in smaller transverse velocities. This caused the front MCP/PS ($L_l = 25$ cm) to have limited resolution since the transverse velocities of interest in the He^* beam had not significantly expanded to fill the detector. This required using the back MCP/PS ($L_l = 63$ cm), which gave adequate resolution but lower signal since the expansion along the second transverse dimension (perpendicular to the bichromatic force) could not be completely captured on the detector. This required integrating the detection signal for longer to obtain similar signal to noise (S/N) levels.

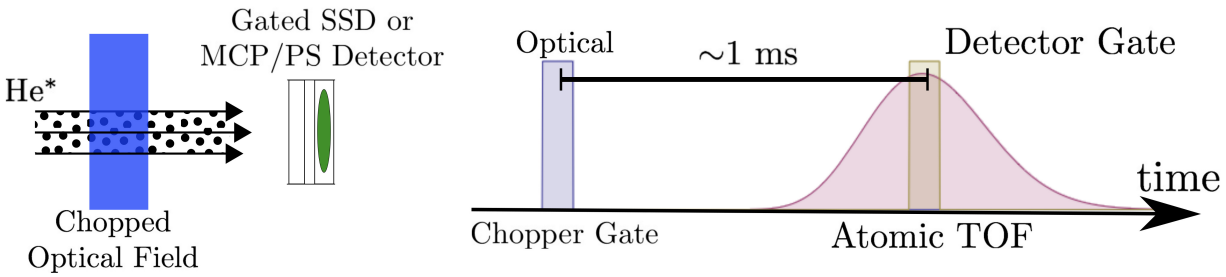

Figure 6.8: Longitudinal time of flight was used to reduce the smearing associated with the longitudinal velocity distribution. A chopper wheel would gate the bichromatic standing waves, and the transverse He* distribution would arrive at the detector at a time delay given by its longitudinal velocity. The detector was then gated to only measure a subset of these velocities.

However data taken with both detectors gave the same apparent velocity-space distributions.

The smearing caused by the longitudinal distribution of velocities in the beam makes an absolute measurement of the ultimate cooling limit difficult. Several modifications to the experiment were attempted to reduce this effect, but were largely unsuccessful for different reasons. The next paragraphs will document the different schemes and the limitations that prevented them from working.

It was recognized that atoms traveling perpendicular to the bichromatic standing wave would not have any smearing. This is because the angular exit from the interaction region is given by v_t/v_l so that at $v_t = 0$ the distribution in v_l has no effect. It was thought that the bichromatic standing waves could cross the He* beam at an angle such that the final velocity along the detector's transverse axis would be zero. This scheme doesn't work because the angle required for the cooling to leave the atom with zero transverse velocity relative to the detector itself depends on longitudinal velocity of the atom.

The next attempt was to switch to the back SSD detector and try to minimize the smearing by measuring the transverse velocity distribution along with a longitudinal time of flight (TOF) scheme shown in Fig. 6.8. The bichromatic optical beam was gated using a chopper. Then the longitudinal TOF signal of the laser cooled atoms was recorded with the SSD. The SSD has spatial resolution from a small opening slit and can be scanned across the He* beam. At each position of the SSD, the He* signal was measured as a function of delay time from the chopper on-signal using either a boxcar integrator or LabVIEW data acquisition card. In principle this gives the unsmeared transverse velocity distribution by looking at the position distribution for a fixed time delay corresponding to a subset of

longitudinal velocities.

It actually would contain a wealth of information, by measuring the signal for different time delays a single measurement would give the bichromatic force as a function of interaction time. This scheme gave qualitatively similar results to the initial bichromatic force measurements, however could only be done for a single value of the laser power at a time. Additionally each detector position had to be taken in sequence instead of all at once as with the MCP/PS detector. The He^* signal is also greatly reduced, first by the duty cycle of the on time for the chopper (when cooling is occurring), and second by only looking at the fraction of atoms at a particular longitudinal velocity. This necessitated amplifying the signal by adding a MCP to the SSD device. These effects combined to cause single velocity distribution scans to easily take more than an hour to obtain modest S/N levels, a time for which it was very difficult to maintain stable laser power and bichromatic frequency balance. Even with the chance that the entire system stayed stable enough for a scan, it was determined that the longitudinal velocity distribution could not be sufficiently narrowed given the poor resolution of the TOF set by the minimum chopper opening time and He^* TOF distance.

To speed up the data acquisition process, TOF was attempted with the MCP/PS detector. This was done with a similar optical chopper setup on the laser beams, which triggered a pulse generator. After a fixed delay, the electronic pulse was amplified with a DEI PVX-4150 pulse amplifier to 1000 V and sent to the initially grounded MCP to gate it on. This caused the He^* beam signal to be amplified by the MCP and sent to the PS for only a fixed range of longitudinal velocities. This detection scheme was also severely limited by low signal because of the small duty cycle. The results at the best TOF resolution in longitudinal velocity, integrated for over five minutes for good S/N levels, resulted in distributions that were not significantly different from what was seen with the complete longitudinal velocity distribution, and was only able to cut out the edges of the velocity distribution because of the same TOF limitations listed above.

Chapter 7

Conclusions

The bichromatic force is likely the beginning of a rich field of optical forces involving multifrequency light. The additional frequencies have opened the possibility of using stimulated processes to transfer momentum, energy, and entropy to cool atoms in a method previously believed to be impossible. Once the radiative lifetime is no longer the relevant timescale many of the limits on optical forces are no longer bounded by the atomic properties, and this has been exploited for the experiments in this thesis.

7.1 Lithography Conclusions

The exquisite control over the motion of atoms from optical forces is a major motivation for the field of neutral atom lithography (NAL). Nanoscale lithography is driven by ever shrinking spatial resolution. While electron beam lithography gives the cleanest spatial patterning, the rastering required is slow and only feasible for small scale production, at considerable expense. This leaves optical lithography for most mass produced devices. Optical lithography is cumbersome in the current patterning resolution regime of 10-30 nm, and will always be limited by the size of the image that can be formed, typically on the order of the light's wavelength. For large scale production this requires very bright sources of VUV nearing XUV wavelengths, and in this regime most optical elements have very poor efficiency and quality requiring large investments from the semiconductor industry.

In principle, neutral atom lithography can pattern with unlimited resolution, given that the resolution is now determined by the size of an atom. He^* is a particularly good choice since its large internal energy can be used for a resist-based lithography method, so that the patterned material can differ from that of the atomic beam. However, as with the optical

lithography, this requires a bright beam and the ability to form an image. The bichromatic force along with conventional laser cooling techniques allow complete collimation of our He^* beam, so that lithographic patterning can be done in tens of minutes. Optical masks were demonstrated that show the He^* beam can be patterned and this pattern transferred to the sample.

The atomic physics of neutral atom lithography is clearly effective, and was demonstrated for different optical and mechanical masks. Since the optical mask is determined from the intensity distribution of a laser, it would be possible to produce arbitrary patterns in the He^* using spatial light modulators and holographic techniques. The He^* beam could even be patterned with an optical mask and then focused to a much smaller size onto the sample surface so that the wavelength of the optical mask is not a limiting factor. The only limiting factor at the moment is the surface science required for the resist-based nanoscale patterning. While in principle most lithographic resists are designed for light of a similar energy to the He^* internal energy, the damage mechanisms are quite different, arising from the very small penetration depth of the He^* compared to light. Given the eclectic nature of neutral atom lithography, there is little scientific research in the field of lithography resists optimized for He^* instead of light, leaving the future of NAL uncertain.

7.2 Bichromatic Force Conclusions

The results with the UV bichromatic force on He^* clearly show that the force is mediated by stimulated processes causing many atomic recoils in a time too short to be caused by radiative processes. The results presented here are not an optimum demonstration of the actual cooling potential given the very limited magnitude of δ. The rate of momentum transfer relative to the radiative process δ/γ could be much larger with additional laser power. This would lead to a larger final velocity allowing more potential avoided crossings to be traversed for better cooling. While a very large number of Landau-Zener transitions is likely to cause some heating due to the diffusion among dressed energy states, too few is insufficient to adequately stop all atoms at the velocity limit.

The experiments clearly show that the velocity-space distribution is peaked after interaction with the bichromatic force. This increase in the velocity-space density is the result of cooling, and may be more significant than is measured, given the potential for spatial smearing at the detector caused by the spread of longitudinal velocities. There are two sources of this smearing, one on the location of the peak of the transverse velocity distribution, which only for a cooled peak at $v_t = 0$ has no spatial smearing at the detector. The second

effect causing spatial smearing at the detector is due to the convolution of the longitudinal velocity distribution with the entire transverse velocity distribution around the cooled peak. These two effects could be minimized by reducing the longitudinal velocity spread, either through a beam slowing process or by extending the He^* beam path and gaining better TOF resolution. The slowing would be more technically difficult, but would not suffer the large loss of signal that occurs from the TOF velocity selection.

Verification that the bichromatic force can cool without SE also allows experiments to be done with atoms or molecules without cycling transitions. The choice of transition could be tailored for a better test of the cooling process. A transition with a very narrow linewidth (long lifetime) would more easily allow large ratios of δ/γ. This along with a longer wavelength, to reduce I_s, could be chosen where high power lasers are possible. A careful study of the bichromatic cooling process for a range of detunings could provide a better understanding of the role of the non-adiabatic LZ transitions.

Bibliography

[1] Harold J Metcalf and Peter van der Straten. *Laser Cooling and Trapping*. Springer, New York, 1999.

[2] J M McGuirk, G T Foster, J B Fixler, M J Snadden, and M A Kasevich. Sensitive absolute-gravity gradiometry using atom interferometry. *Physical Review A*, 65:033608, 2002.

[3] Herbert Walther, Benjamin T H Varcoe, Berthold-Georg Englert, and Thomas Becker. Cavity quantum electrodynamics. *Reports on Progress in Physics*, 69(5):1325–1382, April 2006.

[4] M H Anderson, J R Ensher, M R Matthews, C E Wieman, and E A Cornell. Observation of Bose-Einstein Condensation in a Dilute Atomic Vapor. *Science*, 269(5221):198–201, July 1995.

[5] Kendall B Davis, M O Mewes, MR van Andrews, N J Van Druten, D S Durfee, D M Kurn, and Wolfgang Ketterle. Bose-Einstein condensation in a gas of sodium atoms. *Physical Review Letters*, 75(22):3969, 1995.

[6] C C Bradley, C A Sackett, and R G Hulet. Bose-Einstein condensation of lithium: Observation of limited condensate number. *Physical Review Letters*, 78(6):985, 1997.

[7] Markus Greiner and Simon Fölling. Condensed-matter physics: Optical lattices. *Nature*, 453(7196):736–738, June 2008.

[8] Maciej Lewenstein, Anna Sanpera, Veronica Ahufinger, Bogdan Damski, Aditi Sen De, and Ujjwal Sen. Ultracold atomic gases in optical lattices: mimicking condensed matter physics and beyond. *Advances in Physics*, 56(2):243–379, March 2007.

[9] Jasper Chan, TP Mayer Alegre, Amir H Safavi-Naeini, Jeff T Hill, Alex Krause, Simon Gröblacher, Markus Aspelmeyer, and Oskar Painter. Laser cooling of a nanomechanical oscillator into its quantum ground state. *Nature*, 478(7367):89–92, 2011.

[10] E S Shuman, J F Barry, and D DeMille. Laser cooling of a diatomic molecule. *Nature*, 467(7317):820–823, September 2010.

[11] Amar C Vutha, Wesley C Campbell, Yulia V Gurevich, Nicholas R Hutzler, Maxwell Parsons, David Patterson, Elizabeth Petrik, Benjamin Spaun, John M Doyle, and Gerald Gabrielse. Search for the electric dipole moment of the electron with thorium monoxide. *Journal of Physics B: Atomic, Molecular and Optical Physics*, 43(7):074007, 2010.

[12] F Diedrich, J C Bergquist, Wayne M Itano, and D J Wineland. Laser cooling to the zero-point energy of motion. *Physical Review Letters*, 62(4):403, 1989.

[13] Paul D Lett, Richard N Watts, Christoph I Westbrook, William D Phillips, Phillip L Gould, and Harold J Metcalf. Observation of atoms laser cooled below the Doppler limit. *Physical Review Letters*, 61(2):169, 1988.

[14] Jean Dalibard and Claude Cohen-Tannoudji. Laser cooling below the Doppler limit by polarization gradients: simple theoretical models. *Journal of the Optical Society of America B*, 6(11):2023–2045, 1989.

[15] A Aspect, Ennio Arimondo, R Kaiser, N Vansteenkiste, and C Cohen-Tannoudji. Laser cooling below the one-photon recoil energy by velocity-selective coherent population trapping: theoretical analysis. *Journal of the Optical Society of America B*, 6(11):2112–2124, 1989.

[16] L Allen and J H Eberly. *Optical Resonance and Two-Level Atoms*. Dover Publications, New York, 1987.

[17] B R Mollow. Power spectrum of light scattered by two-level systems. *Physical Review*, 188(5), 1969.

[18] Claude Cohen-Tannoudji, Jacques Dupont-Roc, and Gilbert Grynberg. *Atom-Photon Interactions*. Basic Processes and Applications. Wiley-VCH, 1998.

[19] Hans Albrecht Bethe and Edwin E Salpeter. *Quantum Mechanics Of One- And Two-Electron Atoms*. Dover Publications, 2008.

[20] S S Hodgman, R G Dall, L J Byron, KGH Baldwin, S J Buckman, and A G Truscott. Metastable helium: A new determination of the longest atomic excited-state lifetime. *Physical Review Letters*, 103(5):053002, 2009.

[21] A Kramida, Yu. Ralchenko, J Reader, and and NIST ASD Team. Technical report, 2014.

[22] J Söding, R Grimm, Yu B Ovchinnikov, Ph Bouyer, and Ch Salomon. Short-distance atomic beam deceleration with a stimulated light force. *Physical Review Letters*, 78(8):1420, 1997.

[23] Felix Bloch. Nuclear induction. *Physical Review*, 70(7-8):460, 1946.

[24] Richard P Feynman, Frank L Vernon, and Robert W Hellwarth. Geometrical Representation of the Schrödinger Equation for Solving Maser Problems. *Journal of Applied Physics*, 28(1):49–52, 1957.

[25] R Grimm, J Söding, and Yu B Ovchinnikov. Coherent beam splitter for atoms based on a bichromatic standing light wave. *Optics letters*, 19(9):658–660, 1994.

[26] Leonid Yatsenko and Harold Metcalf. Dressed-atom description of the bichromatic force. *Physical Review A*, 70(6):063402, 2004.

[27] J J McClelland. Atom-optical properties of a standing-wave light field. *Journal of the Optical Society of America B*, 12(10):1761–1768, 1995.

[28] Michael Keller. Optical Manipulation of Helium Atoms with Application to Neutral Atom Lithography. Master's thesis, Stony Brook University, August 2006.

[29] M R Williams. *Measurement of the Bichromatic Optical Force on Rubidium Atoms*. PhD thesis, Stony Brook University, May 1999.

[30] M Cashen. *Optical Forces on Atoms in Polychromatic Light Fields*. PhD thesis, Stony Brook University, May 2002.

[31] Claire S Allred. *Neutral Atom Lithography with Metastable Helium*. PhD thesis, Stony Brook University, May 2009.

[32] Jason Reeves. *Neutral Atom Lithography Using the 389 nm Transition in Metastable Helium*. PhD thesis, Stony Brook University, August 2010.

[33] Daniel Stack. *Optical Forces from Periodic Adiabatic Rapid Passage Sequences on Metastable Helium Atoms*. PhD thesis, Stony Brook University, August 2012.

[34] J Kawanaka, M Hagiuda, K Shimizu, F Shimizu, and H Takuma. Generation of an intense low-velocity metastable-neon atomic beam. *Applied Physics B*, 56(1):21–24, January 1993.

[35] H C Mastwijk, M van Rijnbach, J W Thomsen, P van der Straten, and A Niehaus. Photo induced collisions with laser cooled He* atoms. *The European Physical Journal D-Atomic, Molecular, Optical and Plasma Physics*, 4(2):131–137, 1998.

[36] F B Dunning, R D Rundel, and R F Stebbings. Determination of secondary electron ejection coefficients for rare gas metastable atoms. *Review of Scientific Instruments*, 46(6):697–701, 1975.

[37] M Partlow, X Miao, J Bochmann, M Cashen, and H Metcalf. Bichromatic Slowing and Collimation to Make an Intense Helium Beam. *Physical Review Letters*, 93(21):213004, November 2004.

[38] T W Hänsch and B Couillaud. Laser frequency stabilization by polarization spectroscopy of a reflecting reference cavity. *Optics Communications*, 35(3):441–444, December 1980.

[39] Seung Hyun Lee. *Coherent Manipulation of Rydberg Helium Atoms in Inhomogeneous Electric Fields*. PhD thesis, Stony Brook University, August 2006.

[40] R W P Drever, J L Hall, F V Kowalski, J Hough, G M Ford, A J Munley, and H Ward. Laser phase and frequency stabilization using an optical resonator. *Applied Physics B*, 31(2):97–105, June 1983.

[41] G Timp, R E Behringer, D M Tennant, J E Cunningham, M Prentiss, and K K Berggren. Using light as a lens for submicron, neutral-atom lithography. *Physical Review Letters*, 69(11):1636, 1992.

[42] J J McClelland, R E Scholten, E C Palm, and R J Celotta. Laser-Focused Atomic Deposition. *Science*, 262(5135):877–880, 1993.

[43] R Gupta, J J McClelland, Z J Jabbour, and R J Celotta. Nanofabrication of a twodimensional array using laserfocused atomic deposition. *Applied Physics Letters*, 67(10):1378–1380, 1995.

[44] D Meschede and H Metcalf. Atomic nanofabrication: atomic deposition and lithography by laser and magnetic forces. *Journal of Physics D: Applied Physics*, 36(3):R17–R38, 2003.

[45] Claire S Allred, Jason Reeves, Christopher Corder, and Harold Metcalf. Atom lithography with metastable helium. *Journal of Applied Physics*, 107(3):033116, 2010.

[46] Daniel B Wolfe, J Christopher Love, Kateri E Paul, Michael L Chabinyc, and George M Whitesides. Fabrication of palladium-based microelectronic devices by microcontact printing. *Applied Physics Letters*, 80(12):2222–2224, 2002.

[47] J Christopher Love, Daniel B Wolfe, Michael L Chabinyc, Kateri E Paul, and George M Whitesides. Self-assembled monolayers of alkanethiolates on palladium are good etch resists. *Journal of the American Chemical Society*, 124(8):1576–1577, 2002.

[48] M R Williams, F Chi, M T Cashen, and H Metcalf. Measurement of the bichromatic optical force on Rb atoms. *Physical Review A*, 60(3):R1763, 1999.

[49] M R Williams, F Chi, M T Cashen, and H Metcalf. Bichromatic force measurements using atomic beam deflections. *Physical Review A*, 61(2):023408, 2000.

[50] M T Cashen and Harold Metcalf. Bichromatic force on helium. *Physical Review A*, 63(2):025406, 2001.

[51] M A Chieda and E E Eyler. Prospects for rapid deceleration of small molecules by optical bichromatic forces. *Physical Review A*, 84(6):063401, 2011.

[52] Michael Andrew Chieda and E E Eyler. Bichromatic slowing of metastable helium. *Physical Review A*, 86(5):053415, 2012.

[53] S E Galica, L Aldridge, and E E Eyler. Four-color stimulated optical forces for atomic and molecular slowing. *Physical Review A*, 88(4):043418, 2013.

[54] Harold Metcalf. Entropy exchange in laser cooling. *Physical Review A*, 77(6):061401, 2008.

Appendix A

Lithography Fortran Code

A.1 LightMaskProgram.f

```
      program LightMaskProgram
      integer*4 MaxnStep
      parameter( MaxnStep = 100000 )
      real*8 atom(6), Vtrans, param(1), time, tau
      real Vlave, sin
      real*8 xpos(MaxnStep), ypos(MaxnStep), zpos(MaxnStep), tpos(MaxnStep)
      real*8 squaresize, wo, m
      integer*4 idum, nState, nStep, iStep
      external GaussDist
      external velc
      external dipolerk

!Set Parameter Values
      Vtrans = 4.0   !Transverse Velocity
      Vlave = 1125.0      !Longitudinal Ave Velocity
      time = 0.0
      nStep = 50          !Number of steps
      wo = 4.e-4          !Gaussian waist
      squaresize = 3.*3.e-6/2.         !Initial Atomic Dist
      m = 6.646e-27                  !Mass of He
      param(1) = m
      nState = 6

      open(16, file='Fudge8/InitialConditionsvt4.txt',status='unknown')
      open(18, file='Fudge8/FinalConditionsvt4.txt',status='unknown')

      do i=1, 50000
        atom(1) = squaresize*(ran1(idum) - 0.5)        !X-pos
        atom(2) = 3.*wo                                !Y-pos
        atom(3) = squaresize*ran1(idum)                !Z-pos
        atom(4) = Vtrans * GaussDist(idum)             !X-vel
        atom(5) = -1. * velc(Vlave,idum)               !Y-vel
        atom(6) = Vtrans * GaussDist(idum)             !Z-vel
        write(16,*) atom(1), atom(2), atom(3), atom(4), atom(5), atom(6)

        tau = atom(2) / (-1.*atom(5)) / nStep  !Time Steps
        do iStep=1,nStep
          call rk4( atom, nState, time, tau, dipolerk, param )
          time = time + tau
          tpos(iStep) = time
          xpos(iStep) = atom(1)
          ypos(iStep) = atom(2)
          zpos(iStep) = atom(3)
        enddo
```

```
        write(18,*) xpos(nStep), ypos(nStep), zpos(nStep)
      enddo

      close(16)
      close(18)

      stop
      end
```

A.2 DipoleForce.f

```
      subroutine DipoleForce( x, y, z, Force )

!  Calculates Dipole Force; Used by dipolerk.f
!  Inputs
!    x       Positions in Light Field
!    y
!    z
!  Output
!    Force  The Dipole Force

      real Intensity1, Intensity2, Prefactor
      real m, vl, k, wo
      Integer NTAB
      REAL dfridr, err, h, func, CON, CON2, BIG, SAFE
      PARAMETER (CON=1.4, CON2=CON*CON, BIG=1.E30,NTAB=10,SAFE=2.)
      INTEGER i, j
      REAL errt, fac, hh, a(NTAB,NTAB)
      REAL xp, yp, zp

      !The Following is to find Derivative of Intensity
      !Taken from Numerical Recipes for Fortran
      h = .25e-7
      if(h.eq.0.) pause 'h must be nonzero in dfridr'
      hh = h
      xp = x
      yp = y
      zp = z
      call FieldIntensity( xp, yp, zp+hh, Intensity1)
      call FieldIntensity(xp, yp, zp-hh, Intensity2)
      a(1,1) = (Intensity1 - Intensity2) / (2.0*hh)
      err = BIG
      do i=2, NTAB       !Successive columns in the Neville tableau will go to
        hh = hh/CON        !smaller stepsizes and higher orders of extrapolation
        call FieldIntensity(xp, yp, zp+hh, Intensity1)
        call FieldIntensity(xp, yp, zp-hh, Intensity2)
        a(1,i) = (Intensity1 - Intensity2) / (2.0*hh) !Try new smaller stepsize
        fac = CON2
        do j=2,i     !Compute extrapolations of various orders, requiring no new
          a(j,i) = (a(j-1,i)*fac - a(j-1,i-1)) / (fac-1.) !function evaluations
          fac = CON2*fac
          errt = max(abs(a(j,i)-a(j-1,i-1)),abs(a(j,i)-a(j-1,i-1)))
              !The error strategy is to compare each new extrapolation to one
              !order lower, both at the present stepsize and the previous one.
          if(errt.le.err) then        !If the error is decreased, save the
            err=errt                     !improved answer
            dfridr=a(j,i)
          endif
        enddo
        if(abs(a(i,i)-a(i-1,i-1)).ge.SAFE*err) then
          m = 6.646e-27  !mass of He
          vl = 1125.      !Longitudinal velocity for McClelland power
          k = 2 * 3.141 / 1083.e-9 !Wavevector
          wo = 4.e-4               !Laser gaussian waist
          Prefactor = 8. * 5.37  *  0.5 * m * vl**2.  /  (k**2. * wo**2.) !Force prefactor
          Force = Prefactor * dfridr !Const * Derivative of Intensity
          return
        endif
        !If higher order is worse by a significant factor SAFE, then quit early
```

```
      enddo
      m = 6.646e-27  !mass of He
      vl = 1125.     !Longitudinal velocity for McClelland power
      k = 2 * 3.141 / 1083.e-9 !Wavevector
      wo = 4.e-4               !Laser gaussian waist
      Prefactor = 8. * 5.37  *  0.5 * m * vl**2.  /  (k**2. * wo**2.) !Force prefactor
      Force = Prefactor * dfridr !Const * Derivative of Intensity
      return
      end
```

A.3 dipolerk.f

```
      subroutine dipolerk( x, t, param, deriv )
      real*8 x(*), t, param(*), deriv(*)
      external DipoleForce

!  Returns right-hand side of Doppler Force ODE; used by Runge-Kutta routines
!  Inputs
!    x       State vector [r(1) r(2) r(3) v(1) v(2) v(3)]
!    t       Time (not used) force is time independent
!    param      Parameter mass of He
!  Output
!    deriv  Derivatives [dr(1)/dt dr(2)/dt dr(3)/dt dv(1)/dt dv(2)/dt dv(3)dt]

      real*8 m, v1, v2, v3, accel1, accel2, accel3
      real r1, r2, r3, Force

      !* Compute acceleration
      m = param(1)
      r1 = x(1)
      r2 = x(2)      ! Unravel the vector x into
      r3 = x(3)
      v1 = x(4)      ! position and velocity
      v2 = x(5)
      v3 = x(6)
      accel1 = 0.0   ! no accel in
      accel2 = 0.0   ! x and y
      call DipoleForce( r1, r2, r3, Force)
      accel3 = Force/m  !Dipole Force Accel

      !* Return derivatives [dr(1)/dt dr(2)/dt dr(3)/dt dv(1)/dt dv(2)/dt dv(3)/dt]
      deriv(1) = v1
      deriv(2) = v2
      deriv(3) = v3
      deriv(4) = accel1
      deriv(5) = accel2
      deriv(6) = accel3
      return
      end
```

A.4 FieldIntensity.f

```
      subroutine FieldIntensity( x, y, z, Intensity )

!  Calculates Electric Field Intensity; Used by DipoleForce.f
!  Inputs
!    x       Positions in Light Field
!    y
!    z
!  Output
!    Intensity    The Intensity of the light

      complex*8 Efield1, Efield2
      real*8 zo, wz, Rz, k, woz !, Intensity
      real Intensity
      wz=4.e-4                  !Gaussian waist
```

```
      zo=3.141*wz**2./1083.e-9 !Gaussian Zo
      Rz=z+zo**2.0/z            !Gaussian Rz
      k=2.*3.141/1083.e-9       !WaveVector
      woz=wz*Sqrt(1.0+(z/zo)**2.0)
      Efield1 = wz/woz*EXP(-(x**2.0+y**2.0)/(woz**2.0))*EXP(CMPLX(0.,1.)*(k*(x**2.0+y**2.0)/(2.0*Rz)-ATAN(
     z/zo)+k*z))
      Efield2 = wz/woz*EXP(-(x**2.0+y**2.0)/(woz**2.0))*EXP(CMPLX(0.,1.)*(-k*(x**2.0+y**2.0)/(2.0*Rz)-ATAN
     (z/zo)-k*z))
      Intensity = 1./4. * (Efield1 + Efield2) * (Conjg(Efield1) + Conjg(Efield2))
      return
      end
```

A.5 GaussDist.f

```
      FUNCTION GaussDist(idum)
      INTEGER idum
      REAL GaussDist
      EXTERNAL ran1
        !Returns a normally distributed deviate with zero mean and unit variance, using ran1
        !as the source of uniform deviates. All taken from Numerical Recipes for Fortran
      INTEGER iset
      REAL fac,gset,rsq,v1,v2,ran1
      SAVE iset,gset
      DATA iset/0/
      if(idum.lt.0) iset=0          !Reinitialize
      if(iset.eq.0) then            !We don't have an extra deviate handy, so pick two
1       v1=2.*ran1(idum)-1.         !uniform numbers in the square extending from -1 to
        v2=2.*ran1(idum)-1.         !+1 in each direction.
        rsq=v1**2+v2**2             !See if they are in the unit circle, and if they are
        if(rsq.ge.1..or.rsq.eq.0.) goto 1   !not try again.
        fac=sqrt(-2.*log(rsq)/rsq)          !Now make the Box-Muller transformation to
        gset=v1*fac                 !get two normal deviates. Return one and save the
        GaussDist=v2*fac            !other for next time.
        iset=1                      !Set Flag
      else                          !We have an extra deviate handy
        GaussDist=gset              !So return it.
        iset=0                      !And unset the flag
      endif
      return
      END
```

A.6 ran1.f

```
      FUNCTION ran1(idum)
      INTEGER idum, IA, IM, IQ, IR, NTAB, NDIV
      REAL ran1, AM, EPS, RNMX
      PARAMETER (IA=16807, IM=2147483647, AM=1./IM, IQ=127773, IR=2836, NTAB=32, NDIV=1+(IM-1)/NTAB,EPS
     =1.2e-7,RNMX=1.-EPS)
        !"Minimal" random number generator of Park and Miller with Bays-Durham shuffle and
        !added safeguards. Returns a uniform random deviate between 0.0 and 1.0 (exclusive
        !of the endpoint values). Call with idum a negative integer to initialize; there-
        !after, do not alter idum between successive deviates in a sequence. RNMX should
        !approximate the largest floating value that is less than 1.
      INTEGER j, k, iv(NTAB), iy
      SAVE iv, iy
      DATA iv /NTAB*0/, iy /0/
      if(idum.le.0.or.iy.eq.0) then !Initialize
        idum = max(-idum,1)         !Be sure to prevent idum=0
        do j=NTAB+8,1,-1            !Load the suffle table (after 8 warm-ups)
          k = idum/IQ
          idum = IA*(idum-k*IQ)-IR*k
          if(idum.lt.0) idum=idum+IM
          if(j.le.NTAB) iv(j)=idum
        enddo
        iy=iv(1)
      endif
```

```
      k=idum/IQ                        !Start here when not initializing
      idum=IA*(idum-k*IQ)-IR*k         !Compute idum=mod(IA*idum,IM) without overflows by
      if(idum.lt.0) idum=idum*IM         !Schrage's method.
      j=1+iy/NDIV                      !Will be in the range 1:NTAB.
      iy=iv(j)                         !Output previously stored value and refill the shuffle
      iv(j)=idum                         !table
      ran1=min(AM*iy,RNMX)             !Because users don't expect endpoint values
      return
      end
```

A.7 rk4.f

```
      subroutine rk4( x, nX, t, tau, derivsRK, param )
      integer*4 MAXnX, MAXnparam
      parameter( MAXnX = 50, MAXnparam = 1000 )
      integer*4 nX
      real*8 x(nX), t, tau, param(MAXnparam)
! Runge-Kutta integrator (4th order)
! Inputs
!   x           Current value of dependent variable
!   nX          Number of elements in dependent variable x
!   t           Independent variable (usually time)
!   tau         Step size (usually time step)
!   derivsRK    Right hand side of the ODE; derivsRK is the
!               name of the function which returns dx/dt
!               Calling format derivsRK(x,t,param,dxdt).
!   param       Extra parameters passed to derivsRK
! Output
!   x           New value of x after a step of size tau

      integer*4 i
      real*8 half_tau, t_half, t_full
      real*8 F1(MAXnX), F2(MAXnX), F3(MAXnX), F4(MAXnX), xtemp(MAXnX)

      !* Evaluate F1 = f(x,t).
      call derivsRK( x, t, param, F1 )

      !* Evaluate F2 = f( x+tau*F1/2, t+tau/2 ).
      half_tau = 0.5*tau
      t_half = t + half_tau
      do i=1,nX
        xtemp(i) = x(i) + half_tau*F1(i)
      enddo
      call derivsRK( xtemp, t_half, param, F2 )

      !* Evaluate F3 = f( x+tau*F2/2, t+tau/2 ).
      do i=1,nX
        xtemp(i) = x(i) + half_tau*F2(i)
      enddo
      call derivsRK( xtemp, t_half, param, F3 )

      !* Evaluate F4 = f( x+tau*F3, t+tau ).
      t_full = t + tau
      do i=1,nX
        xtemp(i) = x(i) + tau*F3(i)
      enddo
      call derivsRK( xtemp, t_full, param, F4 )

      !* Return x(t+tau) computed from fourth-order R-K.
      do i=1,nX
        x(i) = x(i) + tau/6.*(F1(i) + F4(i) + 2.*(F2(i)+F3(i)))
      enddo

      return
      end
```

A.8 velc.f

```
      FUNCTION velc(Vave,idum)
      INTEGER idum
      REAL velc
      EXTERNAL ran1
        !Returns a normally distributed deviate with zero mean and unit variance, using ran1
        !as the source of uniform deviates. All taken from Numerical Recipes for Fortran
      REAL Vave, Vel, Prob, Maxwell
      REAL ran1
      if(Vave.le.0) pause 'Need a positive average velocity'
1     Vel=3000.*ran1(idum)        !uniform numbers in the square extending from 0 to 3000
      Prob=0.0009*ran1(idum)        !and 0 to 0.0009
      Maxwell = 32./(3.141**2.*Vave**3.)*Vel**2.*EXP(-4./3.141*(Vel/Vave)**2.)
      if(Prob.gt.Maxwell) goto 1
      velc=Vel
      return
      END
```

Appendix B

Bichromatic Force Fortran Code

B.1 uvforce.f90

```
program force
        implicit none

        !Constants
        double precision pi,lambda,k,hbar,gamma,forfact,velfact,mass
        parameter(pi=3.141592654,lambda=388.98E-9,hbar=1.054571E-34,gamma=9.36E6,mass=6.64E-27)
        parameter(k=2.0*pi/lambda,forfact=hbar*k*gamma,velfact=gamma/k)

        !Input Parameters
        integer datapoints
        parameter(datapoints=41)
        double precision :: dsym = (15.*gamma)     !Detuning
        double precision :: wR = (1.22*15.*gamma) !Rabi Freq
        double precision :: phi = -2.0*pi !*(-3.0)/2.0            !Phase
        double precision :: rtol = 1.0E-12          !Relative Tolerance
        double precision :: atol = 1.0E-12          !Absolute Tolerance

        !ODE Parameters
        integer neqn         !Number of Differential Equations
        double precision h0      !Initial Step Size for ODE Solver
        integer lwork, liwork
        parameter(neqn=5)
        parameter(lwork=24+neqn*(48+2*neqn), liwork=37+neqn)
        double precision work(lwork)
        integer iwork(liwork)
        double precision rpar(8) !Real Parameters for the ODE Solving Process
        integer ipar(1)                  !Int Parameters for the ODE Solving Process
        integer idid                     !Return Code of the ODE Solver
        external feval, jeval, solout
        integer ijac, mljac, mujac, iout
        double precision u(5)     !Bloch Vector (u1,u2,u3,z,v)

        !Loop Parameters
        integer i, j, ntime
        double precision tstart, tstop, tend, dt
        double precision fors, vo, dv
        character*2 filename

        dv = velfact/1.0             !Velocity Step Size
        vo = -20.*velfact - dv !Velocity Start - Step Size

        !Loop Over Velocities
        do j = 1, datapoints
                vo = vo + dv
```

```
                !Reset ODE Solver Inputs
                do i = 1, lwork          !Use Default Parameters for work
                        work(i) = 0.0
                end do
                do i = 1, liwork         !Use Default Parameters for iwork
                        iwork(i) = 0
                end do
                idid = 0
                ijac = 0
                mljac = neqn
                mujac = neqn
                iout = 0

                !ODE Parameters
                rpar(1) = gamma
                rpar(2) = -gamma/2.0
                rpar(3) = dsym
                rpar(4) = k
                rpar(5) = 4.0*wR*dsin(phi/4.0)
                rpar(6) = 4.0*wR*dcos(phi/4.0)
                rpar(7) = -2.0*hbar*k/mass*wR*dsin(phi/4.0)
                rpar(8) = -2.0*hbar*k/mass*wR*dcos(phi/4.0)

                !Initial Values
                u(1) = 0.0   !Initial
                u(2) = 0.0   !Bloch
                u(3) = -1.0  !Vector
                u(4) = 0.0   !Z - meters
                u(5) = vo    !V - meters/second

                !Set Integration Times
                tstart = 0.0E0
                dt = 10.0*.005/gamma!1.0*.005/gamma                              !tau/10
                tend = 40.0*1.0/gamma!4.0*1.0/gamma                        !4tau
                ntime = idint((tend-tstart)/dt) !# of Steps
                h0 = dt/1000.0                                  !Initial Step Size

                !Setup Output File
                write (filename,'(I2.2)') j
                open(unit=88,file='output'//filename//'.dat')

                !Loop on Time
                do i = 1, ntime
                        tstop = tstart + dt
                        !Force
                        fors = mass*rpar(8)*dsin(rpar(4)*u(4))*dcos(rpar(3)*tstart)*u(1) + mass*rpar(7)*
                             dcos(rpar(4)*u(4))*dsin(rpar(3)*tstart)*u(2)
                        !Write to File: t, z, v, F, u1, u2, u3
                        write(88,9999) tstart,u(4),u(5)/velfact,fors/forfact,u(1),u(2),u(3)
                        !Integrate Over Time Step dt
                        call bim(neqn,feval,tstart,tstop,u,h0,rtol,atol,jeval,ijac,mljac,mujac,work,lwork,
                             iwork,liwork,rpar,ipar,iout,idid)
                        if (idid.ne.0) then
                                write(*,*) 'ERROR: returned idid =', idid
                        end if
                end do
                9999 format(7F25.9)
                close(88)
        end do
        stop
end


! Subroutine implements Optical Bloch Equations (OBEs)
subroutine feval(neqn,t,u,du,ierr,rpar,ipar)
        integer neqn,ierr,ipar
        double precision t,u(neqn),du(neqn),rpar(8),a,b,da,db

        ! rpar(1) = gamma
        ! rpar(2) = -gamma/2.0
```

```
        ! rpar(3) = dsym
        ! rpar(4) = k
        ! rpar(5) = 4.0*wR*dsin(phi/4.0)
        ! rpar(6) = 4.0*wR*dcos(phi/4.0)
        ! rpar(7) = -2.0*hbar*k/mass*wR*dsin(phi/4.0)
        ! rpar(8) = -2.0*hbar*k/mass*wR*dcos(phi/4.0)

        !Optical Fields
        a = rpar(5)*dsin(rpar(4)*u(4))*dsin(rpar(3)*t)   !Im(Omega)
        b = rpar(6)*dcos(rpar(4)*u(4))*dcos(rpar(3)*t)   !Re(Omega)
        da = rpar(7)*dcos(rpar(4)*u(4))*dsin(rpar(3)*t)  !dIm(Omega)/dz
        db = rpar(8)*dsin(rpar(4)*u(4))*dcos(rpar(3)*t)  !-dRe(Omega)/dz

        !Derivatives
        du(1) = rpar(2)*u(1) - a*u(3)
        du(2) = rpar(2)*u(2) - b*u(3)
        du(3) = a*u(1) + b*u(2) - rpar(1)*u(3) - rpar(1)
        du(4) = u(5)
        du(5) = db*u(1) + da*u(2)
        return
end

! Subroutine for evaluating the Jacobian of the function
! Just Dummy, since Jacobian is calculated numerically
subroutine jeval (neqn,t,y,jac,ldim,ierr,rpar,ipar)
        integer neqn,ldim,ierr,ipar
        double precision t,y(neqn),jac(ldim,neqn),rpar

        return
end

! Subroutine for output after each step
! Just Dummy, since no output after each step
subroutine solout(m,t,y,f,k,ord,irtrn)
        integer m,k,ord,irtrn
        double precision t(k),y(m,k),f(m,k)

        return
end
```

Appendix C

Force Map Video Analysis

C.1 ImageJ Script

```
setBatchMode(true);

//filenumber = "001";            // Keep Commented when Running Using Bash Script
RotAngle = -45.;                 // Rotation Angle for Images
rect=newArray(195,261,473,172);  // Rectangle to Create Lineouts
seqleng = 250;                   // Number of Files to Process in Each Sequence (Determined from Computer's
     Memory Limitations)
LineoutFolder = filenumber+"/Lineouts/";         // Folder to Save Lineouts to
saveDivided = 0;                 // Set to 1 to Save Divided Images
DividedFolder = filenumber+"/Divided/";     // Folder to Save Divided Images to

// Find the Number of Frames in the AVI file
AVIfile = "AVIs/"+filenumber+".avi";
run("AVI...", "select=[AVIfile] use convert");
numFrames = nSlices;
listleng=numFrames / seqleng;    // Number of Sequences to Loop Over
close();

// Create Background Image
Bckgrndfile = "AVIs/"+filenumber+"b.avi";
run("AVI...", "select=[Bckgrndfile] use convert");      // Import Background AVI
bckgndavi=getTitle();
run("Z Project...", "projection=[Average Intensity]"); // Create Average Image
bckgnd=getTitle();
selectImage(bckgndavi);
close();

// Loop over Sequences of Data Images to Divide/Rotate/Lineout
for (i=0; i<listleng; i++) {       // Loop Over Each Sequence to Process
  filenum=i*seqleng+1;             // First File of the Sequence
  endfilenum = filenum+seqleng-1; // Last File of the Sequence
  run("AVI...", "select=[AVIfile] first=filenum last=endfilenum use convert"); // Import Images
  datastack=getTitle();
  imageCalculator("Divide create 32-bit stack", datastack,bckgnd);  // Divide Background
  dividedstack=getTitle();
  selectImage(datastack);
  close();
  selectImage(dividedstack);
  if(saveDivided)
    run("Image Sequence... ", "format=TIFF name=[] start=0 digits=4 use save=[DividedFolder]");
  run("Rotate... ", "angle=RotAngle grid=1 interpolation=Bicubic enlarge stack");     // Rotate All Images
  makeRectangle(rect[0],rect[1],rect[2],rect[3]);     // Create Rectangle for Lineouts
  for(n=1; n<=nSlices; n++)  {  // Loop Over All Images in the Sequence
    setSlice(n);
```

```
    run("Clear Results");
    prof = getProfile();          // Get Average Lineout of Current Image
    for (j=0; j<prof.length; j++)
      setResult("", j, prof[j]);
    updateResults;
    savefile=LineoutFolder+getInfo("slice.label")+".xls";  // Save Lineout to LineoutFolder with Filename
        Given by Image name
    saveAs("Measurements",savefile);
    }
  close();
}
close();
```

C.2 Mathematica Scripts

```
(* filenumber = 001 (* Keep Commented when Running in Bash *) *)
folder = StringTake["000"<>ToString[filenumber],-3];  (* Folder with Data *)
oscfile = StringTake["000"<>ToString[filenumber-0],-3];  (* Oscilloscope Data File *)
PowervTime = Import["oscdata/WA000"<>oscfile<>".CSV"][[3;;,{4,5}]];  (* Import Oscilloscope Data *)

(* This Section Finds the Time of the Laser Power Jump Using the Derivative of the Oscilloscope Data *)
RabiDerivMax = Max[Table[PowervTime[[i+10,2]]-PowervTime[[i,2]],{i,1,Length[PowervTime]-10}]];  (* Max
    Value of Derivative *)
RabiMaxPos = Flatten[Position[Table[PowervTime[[i+10,2]]-PowervTime[[i,2]],{i,1,Length[PowervTime]-10}],
    RabiDerivMax]][[1]];  (* Position of Max *)
RabiMaxTime = (PowervTime[[RabiMaxPos+10,1]]+PowervTime[[RabiMaxPos,1]])/2;  (* Convert Array Position to
    Time *)

(* This Section Converts Oscilloscope Data to Rabi Frequency *)
Zero = 0.18;  (* Zero Offset of Photodiode Voltage *)
Calib = 40.*40./3.58;  (* Photodiode Calibration (Rabi Freq/Volts) *)
RabivTime = {#[[1]],Re[((#[[2]]-Zero)*Calib)^.5]}&/@PowervTime;  (* Convert Intensity to Rabi Freq *)
Rabifunc = Interpolation[RabivTime];  (* Find Fit to Data *)

(* Import All Lineout Data and Prepend the Associated Video Time *)
Files = FileNames[folder<>"/Lineouts/*.xls"];
data = SortBy[Table[(Prepend[#1, ToExpression[StringDrop[StringDrop[Files[[i]], 13],-6]]] & ) /@ Drop[
    Import[Files[[i]]], 1], {i, 1, Length[Files]}],First];  (* The Value of 13 is Dependent on Folder File
    Structure *)

(* This Section Finds the Time of the Laser Power Jump Using the Derivative of Chi^2 Type Values Between
    Lineouts *)
VidDerivMax = Max[Table[Norm[(data[[i,;;,3]]-data[[i+5,;;,3]])],{i,1,Length[data]-5}]];  (* Max Value of
    Derivative *)
VidDerivPos = Flatten[Position[Table[Norm[(data[[i,;;,3]]-data[[i+5,;;,3]])],{i,1,Length[data]-5}],
    VidDerivMax]][[1]];  (* Position of Max *)
VidMaxTime = (data[[VidDerivPos+5,1,1]]+data[[VidDerivPos,1,1]])/2;  (* Convert Array Position to Time *)

(* This Section Replaces the Video Time with Rabi Frequency in the Data *)
pixelcal = .030;
offsettime = VidMaxTime - RabiMaxTime;  (* Offset Time Between Video and Oscilloscope *)
(* Drop Video Frames Before Oscilloscope Data Starts *)
data = Select[data,(PowervTime[[-1,1]]+offsettime)>#[[1,1]]>(PowervTime[[1,1]]+offsettime)&];
CalData = Map[{Rabifunc[#[[1]]-offsettime],#[[2]]*pixelcal,#[[3]]}&,data,{2}];  (* Add Rabi Frequency in
    Place of Video Time *)

(* This Section Saves the Data in a Mathematica Format *)
SetDirectory[folder];  (* Folder of Current File Number *)
CalData>>data.m;  (* Save Data *)


startpx = 1;
endpx = All;
numRabipoints = numPoints;
numPospoints = numPoints;
folder = StringTake["000"<>ToString[filenumber],-3];  (* Folder with Data *)

SetDirectory[folder];  (* Folder of Current File Number *)
data = << data.m;
data = SortBy[data[[startpx;;endpx,;;,;;]],First];
NumPixel = Length[data[[1,;;,2]]];
```

```
MinRabi = Min[data[[;;,1,1]]];
MaxRabi = Max[data[[;;,1,1]]];
RabiStep = (MaxRabi-MinRabi)/(numRabipoints-1);
If[numPospoints > NumPixel, numPospoints = NumPixel];
PosStep = NumPixel / numPospoints;

RabiAveraged = Table[Table[datavalues = Mean[Select[data[[;;,Pixel,;;]],Rabi<=#[[1]]<(Rabi+RabiStep)&]];
    If[Length[datavalues]!=3,{},{datavalues[[2]],datavalues[[1]],datavalues[[3]]}],{Rabi,MinRabi-RabiStep
    /2,MaxRabi,RabiStep}],{Pixel,1,NumPixel,1}];

PosAveraged = Table[Table[Mean[RabiAveraged[[Round[j*PosStep]+1;;Round[j*PosStep+PosStep],i,;;]]],{j,0,
    numPospoints-1}],{i,1,Length[RabiAveraged[[1]]]}];

Put[PosAveraged,"Averaged"<>ToString[numRabipoints]<>".m"];
```